Measurement of the Top-Quark Mass in the Semileptonic Decay Channel at the ATLAS Experiment

Diplomarbeit an der Fakultät für Physik
der
Ludwig-Maximilians-Universität München

vorgelegt von
Janna Katharina Behr
geboren in Erlangen

München, den 30. März 2012

1. Gutachter: Prof. Dr. Otmar Biebel

2. Gutachter: Prof. Dr. Jochen Schieck

Kurzfassung

Eine präzise Bestimmung der Masse des Top-Quarks ist sowohl in theoretischer als auch in experimenteller Hinsicht von erheblichem Interesse. Eine genaue Kenntnis dieser Größe erlaubt nicht nur Rückschlüsse auf andere Parameter des Standardmodells der Teilchenphysik - und stellt damit eine wichtige Möglichkeit dar, dieses auf Konsistenz zu testen -, sondern ermöglicht auch indirekte Vorhersagen über die Eigenschaften möglicher neuer Teilchen, die im Rahmen von Erweiterungen des Standardmodells postuliert werden.

Am Large Hadron Collider (LHC) am Kernforschungszentrum CERN bei Genf werden seit März 2010 Protonen bei einer Schwerpunktsenergie von 7 TeV zur Kollision gebracht. Top-Quarks werden in diesen Kollisionen bevorzugt in Paaren von Teilchen und Antiteilchen mit einem Wirkungsquerschnitt von etwa 170 pb erzeugt. Allein im vergangenen Jahr wurde am ATLAS-Experiment, einem der vier großen Detektoren des LHC, eine Datenmenge entsprechend einer integrierten Luminosität von 5 fb^{-1} aufgezeichnet. Dies entspricht etwa 850.000 Top-Antitop-Ereignissen, die potentiell für eine Massenmessung zur Verfügung stehen.

Mit wachsender Datenmenge wird sich die statistische Unsicherheit auf die Top-Quark-Masse weiter reduzieren. Bereits die derzeit durchgeführten Messungen sind von systematischen Unsicherheiten dominiert. Die Herausforderung an zukünftige Analysen besteht dementsprechend darin, die Ursachen dieser systematischen Unsicherheiten zu identifizieren und ihren Einfluss soweit wie möglich zu verringern. In diesem Zusammenhang spielt die Unsicherheit auf die Jet-Energieskala als eine der dominanten Quellen systematischer Unsicherheit eine entscheidende Rolle.

In der vorliegenden Arbeit wird eine neue Methode zur Bestimmung der Masse des Top-Quarks vorgestellt, die speziell zu dem Zweck entwickelt wurde, die Abhängigkeit der Top-Quark-Masse von der Jet-Energieskala und die damit verbundene systematische Unsicherheit zu verringern. Die Masse des Top-Quarks wird dabei allein anhand der Winkel zwischen den drei Jets aus seinem hadronischen Zerfall, gemessen im Ruhesystem des Top-Quarks, berechnet. Da Winkel zwischen Jets deutlich präziser vermessen werden können als deren Energien und Impulse, sollte die mit dieser Methode bestimmte Masse eine verringerte Abhängigkeit von der Jet-Energieskala aufweisen. Dies wird im Rahmen dieser Arbeit bestätigt.

Dazu wird der neue Ansatz mit den beiden bereits etablierten Methoden zur Massenbestimmung verglichen: Im Falle der ersten und gängigsten Messmethode wird die Masse des Top-Quarks der invarianten Masse der drei Jets aus seinem hadronischen Zerfall gleichgesetzt. Im zweiten Fall wird diese Masse durch die invariante Masse der beiden Jets aus dem hadronischen Zerfall des W-Bosons geteilt und das Verhältnis mit dem Literaturwert der W-Boson-Masse reskaliert.

Unter der vereinfachenden Annahme einer globalen Unsicherheit auf die Jet-Energieskala von 5% erhält man eine entsprechende Unsicherheit sowohl auf die mit der Winkelmethode als auch auf die mit der Verhältnismethode bestimmte Top-Quark-Masse von etwa 0.8 GeV. Die entsprechende Unsicherheit im Falle der 3-Jet-Methode beträgt dagegen 7.7 GeV. Die Winkelmethode stellt somit im Hinblick auf die Präzision der Messung eine erhebliche Verbesserung im Vergleich zur gängigen 3-Jet-Methode dar und ist mit der Verhältnismethode vergleichbar.

Die verbleibende Abhängigkeit der mit der Winkelmethode bestimmten Top-Quark-Masse von der Jet-Energieskala ist durch die Notwendigkeit bedingt, den Lorentz-Boost des Top-Quarks bezüglich des Laborsystems aus den gemessenen Energien und Impulsen seiner Zerfallsprodukte zu berechnen, um so die Winkel zwischen den Jets im Ruhesystem des Top-Quarks zu bestimmen. Erste Untersuchungen, die im Rahmen dieser Arbeit durchgeführt wurden, deuten darauf hin, dass durch Interpolation hin zu Massenwerten entsprechend Top-Quarks mit kleinem Boost, für die die Winkel zwischen den Jets direkt im Laborsystem gemessen werden können, die durch die Jet-Energieskalen-Unsicherheit bedingte Unsicherheit auf die Top-Quark-Masse auf vernachlässigbare Werte reduziert werden kann.

Abstract

A precise determination of the top-quark mass is of great importance for both theory and experiment. Not only does it allow for consistency tests of the Standard Model of Particle Physics, but it can also be used to derive constraints on the properties of new particles predicted by many extensions of the Standard Model.

The Large Hadron Collider (LHC) at CERN, where protons have been brought to collision since March 2010, allows the production of top quarks at an as yet unprecedented centre-of-mass energy of 7 TeV. In the year 2011 alone an amount of data corresponding to an integrated luminosity of roughly 5 fb^{-1} has been recorded by the ATLAS experiment, one of the four big experiments at the LHC. Top quarks are predominantly produced in pairs of top and anti-top quarks ($t\bar{t}$) with a production cross section of 170 pb at 7 TeV. This corresponds to approximately 850,000 $t\bar{t}$ events in the 2011 dataset which are available for analysis.

In current analyses, the overall uncertainty on the top-quark mass is already dominated by systematic uncertainties and, with more data being collected, the statistical uncertainty is expected to be reduced even further. For future precision measurements it is therefore imperative to assess and reduce the different sources of systematic uncertainty. In this context, the jet-energy scale (JES) and its uncertainty play a key role as one of the dominant sources of systematic uncertainty on the top-quark mass.

In this thesis, a new estimator for the top-quark mass is introduced which has specifically been developed with the aim of reducing the JES-related systematic uncertainty of the measurement. It relies on the idea that angles between jets can be measured more accurately than their energies and momenta. It is shown that the top-quark mass can be obtained using only the angles between the three jets from the hadronic decay of the top quark determined in the restframe of the latter.

The new mass estimator is compared to the two established estimators, the invariant three-jet mass and the 3-to-2-jet invariant mass ratio re-scaled by the literature value of the W-boson mass. Assuming a global uncertainty on the JES of 5%, the systematic uncertainty on the top-quark mass evaluated with the simple three-jet method is 7.7 GeV. With the jet-angles approach, this value is reduced to a mere 0.8 GeV which is equal to the value obtained with the ratio method. Hence, the new mass estimator yields a significant improvement in precision compared to the standard estimator, the invariant three-jet mass, and is comparable to the ratio method which is already used in some analyses.

First studies presented in this thesis indicate that the remaining JES dependence of the angles method can potentially be eliminated by interpolation towards the masses of top quarks with small Lorentz boosts for which the angles between the jets can be measured directly in the laboratory frame.

Contents

1. Introduction

The first proton-proton collisions at the CERN based Large Hadron Collider (LHC) in March 2010 marked the beginning of a new era of particle physics. With its current centre-of-mass energy of 7 TeV and an instantaneous luminosity of the order of $10^{33}\text{cm}^{-2}\text{s}^{-1}$ the LHC does not only provide an excellent facility for testing the Standard Model of Particle Physics to a yet unprecedented precision, it also bears the potential of discovering new physics beyond the Standard Model.

The top quark, the heaviest elementary particle known to date, plays a key role at this threshold between known physics and new phenomena at the TeV-scale predicted by many theories: The precise measurement of its properties (such as its production cross section, its charge or its mass) does not only allow for consistency tests of the Standard Model, it also yields indirect predictions of the masses of new particles. Most prominently, the value of the top-quark mass together with that of the W-boson mass allows to derive constraints on the mass of the (Standard Model) Higgs boson. In the case of a discovery of the latter and a subsequent direct measurement of its mass these indirect constraints may serve as an important cross check.

The world average of the top-quark mass is based on measurements performed at the TeVatron collider at the Fermilab near Chicago. Its current value, obtained from a combination of Run I (1992-1996) and Run II (2001-2011) measurements, performed at the two experiments CDF and DØ, and based on 5.8 fb^{-1} of data, is:

$$m_{\text{top}} = 173.2 \pm 0.6\ (\text{stat.}) \pm 0.8\ (\text{syst.})\ \text{GeV} \quad [1]$$

With the shutdown of the TeVatron in September 2011, it is now up to the LHC based experiments ATLAS and CMS to reproduce and eventually improve the precision to which the top-quark mass is known. The measurements at these experiments benefit from the high luminosity and centre-of-mass energy of the LHC which justifies its label "top-quark factory": In the year 2011 alone, a dataset corresponding to an integrated luminosity of roughly 5 fb^{-1} has been collected by both experiments. Top quarks are predominantly produced in pairs of top and anti-top quarks ($t\bar{t}$) via the strong interaction with a production cross section of 170 pb at 7 TeV. This corresponds to approximately 850,000 $t\bar{t}$ events in the 2011 dataset which are available for analysis. In current measurements, the uncertainty on the top-quark mass is already dominated by systematic uncertainties (see Figure 1.1). With more data being collected, the statistical uncertainty is expected to be reduced even further.

Hence the challenge for future analyses will be to assess and reduce the different sources of systematic uncertainty on the top-quark mass. To this end, a wide range of analysis approaches has been developed that focus on different kinematical and topological properties of $t\bar{t}$ events in different decay channels. The latter are classified according to the decay of the two W-bosons stemming from the decays of the top and anti-top quark, respectively. These may either decay leptonically into a charged lepton and its corresponding neutrino or hadronically into a quark and an anti-quark. The $t\bar{t}$ decay channels are accordingly labelled as dileptonic, semileptonic/lepton+jets and allhadronic/all-jets.

The analysis presented in this thesis is performed in the semileptonic decay channel which is also known as the "Golden Channel" for top-quark analyses: The leptonic signature can be used to efficiently reject the huge QCD background characteristic for hadron colliders and the hadronic decay allows a full kinematic reconstruction of the corresponding top quark. Various approaches to reconstructing the top quark from its hadronic decay products - two light quarks from the W-boson

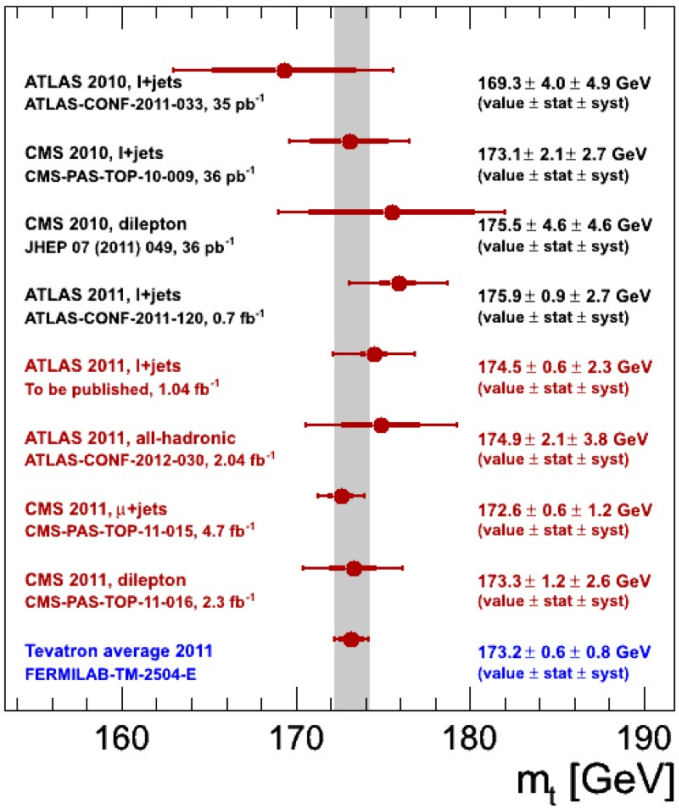

Figure 1.1.: Current status of the top-quark mass measurements performed at the TeVatron collider and the two experiments ATLAS and CMS at the LHC. These values have been summarised for the Moriond conference, March 2012. [2]

decay and a b-quark which lead to hadronic jets in the detector - and determining its mass have been developed.

It turns out that for most of these measurements the jet-energy scale (JES), which relates the measured energy of the jets to that of the original partons, is among the dominant sources of systematic uncertainty. To increase the precision of the measurement of the top-quark mass, it is therefore essential to find a way to reduce the JES dependence of the measurement. One way to achieve this aim is to replace the most commonly used mass estimator, which takes the invariant mass of the three jets from the hadronic top-quark decay as the top-quark mass, by an improved estimator which relies on the ratio of the invariant three-jet mass and the invariant mass of the two jets from the W-boson decay re-scaled by the W-boson mass from literature to calculate the top-quark mass. With this estimator a higher precision of the measurement can be achieved.

In this thesis, a new estimator for the top-quark mass is introduced which relies on the idea that angles between jets can be measured more accurately than their energies and momenta. It is shown that the mass of the hadronically-decaying top quark can be calculated using only the angles between the three jets in the restframe of the top quark. The JES dependence of this new estimator is compared to that of the two established estimators. The resulting JES-related systematic uncertainty of the new method is comparable to that of the ratio method and constitutes a considerable improvement in precision compared to the simple invariant three-jet mass estimator.

The remaining JES dependence can be attributed to the necessity of determining the Lorentz boost of the top quark with respect to the laboratory frame from the four-momenta of its decay products. This is required in order to calculate the angles between the jets in the top-quark restframe. By plotting the reconstructed mass values against the Lorentz boost of the corresponding top quarks

and interpolating to the case of vanishing boost the mass point corresponding to top quarks that are at rest in the laboratory frame is derived. The results presented in this thesis indicate that this mass point is independent of the JES and that hence the JES-related systematic uncertainty is negligible.

Conventions

Throughout this thesis, **natural units** are used in accordance with the conventions of particle physics, i.e.

$$\hbar \equiv c \equiv k_B \equiv 1.$$

All charges are given in units of the elementary charge

$$e = 1.602176487(40) \cdot 10^{-19}\text{C} \text{ [3]}$$

and for energies and masses the unit electron-volt (eV) is used.

2. The Top Quark in the Context of the Standard Model of Particle Physics

The discovery of the top quark by the CDF [4] and DØ [5] collaborations at the Fermilab-based TeVatron collider in 1995 marked a significant milestone for both experimental and theoretical high-energy physics but, unlike other discoveries in the history of particle physics, it did not come entirely unexpected.
When the muon was found fifty years earlier [6, 7], in 1947, together with the long sought-after π-meson, the physics community was baffled by the existence of this heavier version of the electron which, at that time, did not fit into any model of subatomic particles.[1] A succession of further discoveries of particles today known as "baryons"[2] and "mesons"[3] as well as ground-breaking experimental results on the parity and charge asymmetry at the subatomic level fuelled the development of models and theories describing the elementary constituents of matter as well as the fundamental forces governing their interactions.
By the end of the 1970s, a consistent set of theories had emerged - a result of a most fruitful interplay between experimental discoveries on the one hand and theoretical predictions on the other - which, since that time, has been commonly summarized under the term "Standard Model of Particle Physics". Its great predictive power concerning not only the existence of previously unknown particles but even the setting of indirect constraints for their masses has since been proven on various occasions. The most remarkable among these were the discoveries of the bottom quark in 1977 [8], the intermediate vector bosons $W^{\pm}$ [9] and Z^0 [10] in 1983 and finally, in 1995, the top quark.

2.1. The Standard Model of Particle Physics

The Standard Model of Particle Physics fundamentally relies on the concept of gauge symmetry in the framework of which it can be summed up most concisely in the following formula:

$$SU(3)_C \times SU(2)_L \times U(1)_Y \tag{2.1}$$

The individual terms stand for the gauge (Lie) groups of the three fundamental forces which can presently be described within the framework of gauge theory: The strong interaction with symmetry group $SU(3)_C$, where the subscript "C" stands for the colour charge to which the quanta of the strong field couple, and the electroweak interactions with symmetry group $SU(2)_L \times U(1)_Y$ with the subscript "L" representing the left-handedness of the coupling to the electroweak charge isospin and "Y" representing the hypercharge.

The fourth known fundamental force, gravity, is missing in this picture: Although there have been attempts to formulate a gauge theory of gravity, all these theories have turned out to be non-renormalisable, i.e. they contain an infinite number of free parameters, the values of which would have to be determined by experiment in order to make sense of the theory. For this reason gravity is not part of the Standard Model of Particle Physics and hence will not be considered here any further.

[1] "Who ordered *that*?" Isidor I. Rabi is said to have exclaimed at the news of this discovery.
[2] This term is derived from the Greek word $\beta\alpha\rho\acute{\upsilon}\varsigma$ meaning "heavy".
[3] This term is derived from the Greek word $\mu\acute{\varepsilon}\sigma o\varsigma$ meaning "intermediate".

2.1.1. Gauge symmetry and the Example of Quantum Electrodynamics (QED)

The concept of a gauge symmetry which is at the heart of the Standard Model undoubtedly ranks among the most profound and important ideas of modern physics: For a quantum field theory to be called a gauge theory, its Langrangian $\mathcal{L}$ is required to be invariant under local transformations $U \in G$ of its fields where G is some symmetry (Lie) group such as $U(1)$ or $SU(3)$.
One of the best-known examples for a local gauge theory is Quantum Electrodynamics (QED) with gauge group $U(1)_{em}$, not to be confused with $U(1)_Y$ in Equation (2.1) (see also Section 2.1.4). The Lagrangian for a free electron spinor field $\Psi(x)$ is given by:

$$\mathcal{L}_{QED} = \bar{\Psi}(x)(i\gamma^\mu \partial_\mu - m)\Psi(x) \tag{2.2}$$

where the γ^μ are the Dirac matrices and repeated indices are summed over.

This expression is clearly invariant under *global* gauge transformations of the spinor fields

$$\begin{aligned} \Psi(x) &\to e^{i\alpha}\Psi(x) \\ \bar{\Psi}(x) &\to e^{-i\alpha}\bar{\Psi}(x) \end{aligned} \tag{2.3}$$

with the constant phase factor $\alpha \in \mathbb{R}$ and $e^{i\alpha} \in U(1)$. Invariance of $\mathcal{L}$ under *local* transformations

$$\begin{aligned} \Psi(x) &\to e^{i\alpha(x)}\Psi(x) \\ \bar{\Psi}(x) &\to e^{-i\alpha(x)}\bar{\Psi}(x) \end{aligned} \tag{2.4}$$

with space-time dependent phase factor $\alpha(x)$, however, requires the ordinary derivative in Equation (2.2) to be redefined as follows:

$$\partial_\mu \to \mathcal{D}_\mu = \partial_\mu + iq\mathcal{A}_\mu(x) \tag{2.5}$$

where the newly introduced *gauge field* $\mathcal{A}_\mu(x)$ transforms as

$$\mathcal{A}_\mu(x) \to \mathcal{A}_\mu(x) - q^{-1}\partial_\mu\alpha(x) \tag{2.6}$$

and q is a free parameter which can be identified with the electric charge.
The complete QED Lagrangian, which includes the gauge/photon field as a dynamic variable, is then given by

$$\mathcal{L}_{QED} = \bar{\Psi}(x)(i\gamma^\mu \mathcal{D}_\mu - m)\Psi(x) - \frac{1}{4}F_{\mu\nu}F^{\mu\nu} \tag{2.7}$$

where the field tensor

$$F_{\mu\nu} = \partial_\mu \mathcal{A}_\nu - \partial_\nu \mathcal{A}_\mu \tag{2.8}$$

is gauge-invariant by itself.

The quanta of the gauge field $\mathcal{A}_\mu(x)$ are the photons that couple to the electric charge, thereby mediating the force between electrically charged particles. Hence the mere requirement for the Lagrangian to be invariant under the action of some local symmetry group G automatically dictates the existence of gauge fields and the nature of their couplings.

It is worth noting that this property, commonly referred to as **universality**, is of crucial importance in modern physics when it comes to model building, e.g. in order to formulate a Grand Unified Theory (GUT) that describes the three fundamental forces of the Standard Model in a unified framework: The standard approach is to start by postulating a certain symmetry while merely requiring that the corresponding symmetry group G contains the Standard Model: $G \supset SU(3)_C \times SU(2)_L \times U(1)_Y$, and then build a Lagrangian that is invariant under the elements of this group.[4]

[4] Compare this to classical electromagnetism: While James. C. Maxwell had formulated his equations between 1861 and 1864 based on empirical insights, it was not until the 1920s that Herman Weyl, who also coined the term "gauge invariance", discovered their underlying U(1) gauge symmetry.

The theory of Quantum Electrodynamics described above undoubtedly ranks among the most successful theories of physics[5]: Not only has it served as a model for plenty of other theories such as Quantum Chromodynamics (Section 2.1.2) or the theory of electroweak interactions (Section 2.1.4), it has also been tested in numerous experiments to an astonishingly high accuracy, exhibiting a yet unprecedented agreement between theoretical calculations and precision measurements.[12]

2.1.2. Quantum Chromodynamics (QCD)

The theory of the interaction of "coloured" particles, Quantum Chromodynamics (QCD), represented by the first term $SU(3)_C$ in Equation (2.1), builds on many concepts developed in the context of QED. However, there is a fundamental difference between these theories which is founded in the structure of the underlying gauge group: $SU(3)$, unlike $U(1)$, is a **non-Abelian Lie group**, meaning that its generators $\mathcal{T}^i$ do not commute; This non-commutativity has profound consequences for the couplings of the gauge field (see below).
The constituting commutation relation of the $SU(3)$ Lie algebra is given by

$$[\mathcal{T}^A, \mathcal{T}^B] = i \sum_{C=1}^{8} f^{ABC} \mathcal{T}^C \tag{2.9}$$

where f^{ABC} are the structure constants of the Lie group and the $\mathcal{T}^A$ are the generators in the eight-dimensional adjoint representation of $SU(3)$.

The generators can be re-written in a more common form in the (three-dimensional) fundamental representation of $SU(3)$ as $t^A = \frac{\lambda^A}{2}$ where the λ^A are the well-known Gell-Mann matrices. (An explicit form of the Gell-Mann matrices can be found in [13].)

The gauge-invariant QCD Lagrangian has a structure similar to the one of QED in Equation (2.7):

$$\mathcal{L}_{QCD} = \sum_q \bar{\Psi}_{q,a}(x)(i\gamma^\mu \partial_\mu \delta_{ab} - g_s \gamma^\mu t^C_{ab} \mathcal{A}^C_\mu - m_q \delta_{ab})\Psi_{q,b}(x) - \frac{1}{4} F^A_{\mu\nu} F^{A\ \mu\nu} \tag{2.10}$$

where repeated indices are summed over and

$$F^A_{\mu\nu} = \partial_\mu \mathcal{A}^A_\nu - \partial_\nu \mathcal{A}^A_\mu - g_s f^{ABC} \mathcal{A}^B_\mu \mathcal{A}^C_\nu. \tag{2.11}$$

Here again, g_s is a parameter that describes the coupling of the gauge fields to colour.

The spinors $\Psi_{q,a}(x)$, which are in the triplet or fundamental representation of $SU(3)$, represent a field of spin-$\frac{1}{2}$ particles that carry a quantum number similar to the electric charge in the case of QED. This quantum number has accordingly been named **colour charge**. Hence the quanta of this spinor field, the **quarks**, come in three *colours* (represented by the index $a \in \{1, 2, 3\}$): red, green or blue. The index "q" stands for the six known quark flavours: up, down, strange, charm, bottom, top (see the overview table in Section 2.1.5).

The gauge fields $\mathcal{A}^C_\mu$ are - in complete analogy to QED - a direct consequence of the requirement that the Lagrangian be invariant under the chosen symmetry group. They are in the (eight-dimensional) adjoint representation of $SU(3)$, hence $A, B, C \in \{1, ..., 8\}$. The quanta of this gauge field are called **gluons** and, just like the photons couple to electric charge q with coupling constant $\alpha = \frac{q^2}{4\pi}$, gluons couple to colour charge g_s with coupling constant $\alpha_s = \frac{g_s^2}{4\pi}$ (see Equation (2.10)), thereby mediating the interaction between coloured particles.

[5] Richard P. Feynman once called it the "jewel of physics"[11].

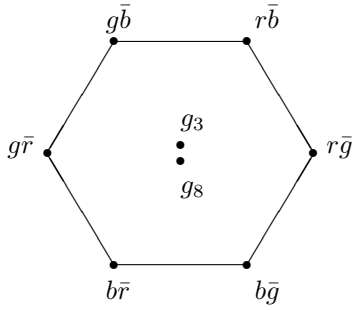

$$g_3 = \frac{1}{\sqrt{2}}(r\bar{r} - g\bar{g})$$
$$g_8 = \frac{1}{\sqrt{6}}(r\bar{r} + g\bar{g} - 2b\bar{b})$$

Figure 2.1.: Gluon octet in the adjoint representation of $SU(3)_C$

However, the non-Abelian structure of $SU(3)_C$ results in a colour charge for the quanta of the gauge field $\mathcal{A}_\mu^C$: While photons do not carry a(n electric) charge and therefore do not interact with one another, gluons carry both colour and anti-colour (Figure 2.1) which allows them to couple to quarks according to vertex (a) in Figure 2.2 but also to other gluons according to vertices (b) and (c). For QED, only the analogue to vertex (a) exist while (b) and (c) are not allowed for photons.

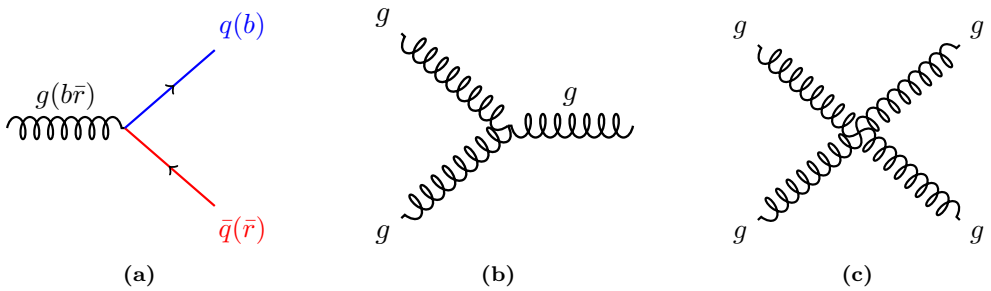

Figure 2.2.: Possible vertices of QCD: (a) gluon-quark coupling, (b) triple-gluon vertex, (c) quadruple-gluon vertex

This **gluon self-interaction** results in a phenomenon known as *anti-screening* which has far-reaching and profound consequences, in particular for the understanding of the physics processes at hadron colliders such as the LHC (see below) and for the interpretation of the quark masses (Section 2.1.3): The coupling constants of QED and QCD, α and α_s respectively, are - contrary to what their name suggests - not constant but vary as a function of the energy scale Q of the process. This is a consequence of **vacuum fluctuations**, a phenomenon that occurs naturally in quantum field theories: The quantum mechanical time-energy uncertainty relation[6] $\Delta t \Delta E \geq 1$ allows the creation of a particle-anti-particle pair with energy ΔE from the vacuum which exists for a brief timespan Δt before its constituents annihilate. These fluctuations modify the propagators of free particles by adding virtual loops as shown in Figure 2.3. The effect of these vacuum contributions, however, is fundamentally different in QED and QCD due to the different nature of their gauge couplings: While in QED loop contributions can arise only from virtual electron-positron pairs (top left in Figure 2.3), the gluon self-coupling of QCD also allows closed gluon loops in addition to those from pairs of quark and anti-quark (top left in Figure 2.3). The virtual electron-positron pairs of QED become polarised in the presence of electrically charged particles, thus *screening* the *bare* charge which leads to a dampening of the electric field at large distances, very similar to the dampening of an electric field that occurs in a dielectric material. As a consequence, the coupling constant α of QED decreases over the distance whereas at higher energies, which allow smaller

[6] This is given in natural units.

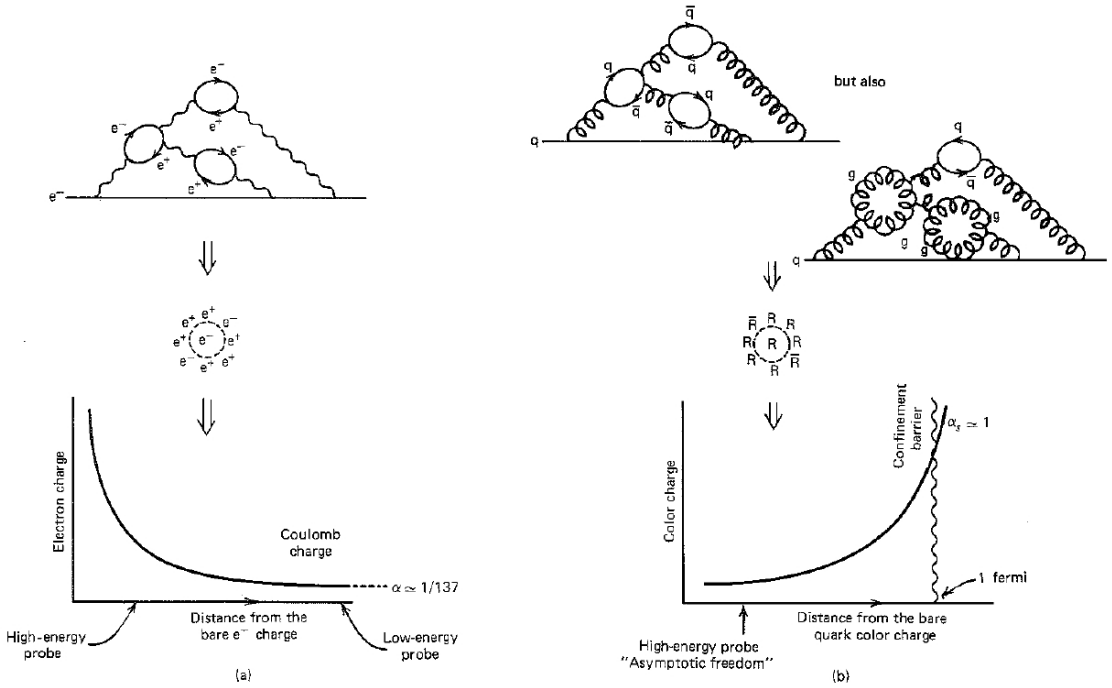

Figure 2.3.: The effect of vacuum fluctuations on the couplings of QED (a) and QCD (b) [14]

distances to be probed, the coupling increases (bottom left in Figure 2.3).
In QCD, however, the additional contributions from the gluon loops reverse the effect of the vacuum fluctuations, leading to a phenomenon called **anti-screening**: At larger distances, i.e. smaller energies, the vacuum *augments* the colour charge, an effect similar to the increase of the magnetic field in a paramagnetic substance. Accordingly, the strong coupling constant α_s *decreases* with increasing Q (top right in Figure 2.3 and Figure 2.4). This effect is known as **asymptotic freedom**. It implies that quarks inside mesons and baryons can approximately be treated as free particles and that perturbation theory can successfully be applied in this energy regime.

On the other hand, α_s is large for small energies and large distances. This has profound consequences for both theory and experiments:

- Perturbation theory fails in the low-energy regime. This calls for non-perturbative approaches to model QCD processes and calculate quantities such as proton and quark masses, the search for and optimisation of which is still a field of ongoing research. An already well-established non-perturbative method is *lattice QCD*: Calculations are performed on a discrete spacetime lattice which not only regularises the theory but also allows for numerical simulations of QCD processes. This model correctly predicts the confinement of colour for the strong interaction [12] and is currently used to derive quantities such as the masses of hadrons and quarks [3].

- It is impossible to observe free quarks. Any attempt to separate two coloured particles, for example the quark and anti-quark in a meson, leads to an increase of the energy density of the gluon field between the quarks. At some point, the additional energy stored in the field is large enough for the creation of another pair of quark and anti-quark from the vacuum which then forms two colourless mesons with the two initial quarks. This phenomenon is known as **confinement**: The coloured quarks are confined within hadrons which do not possess a net colour. This does not only make it difficult to measure properties of quarks such as the top quark mass but it also poses an epistemological problem: How can we make sense of a quantity such as the mass of a particle that we can never, due to the very nature of its

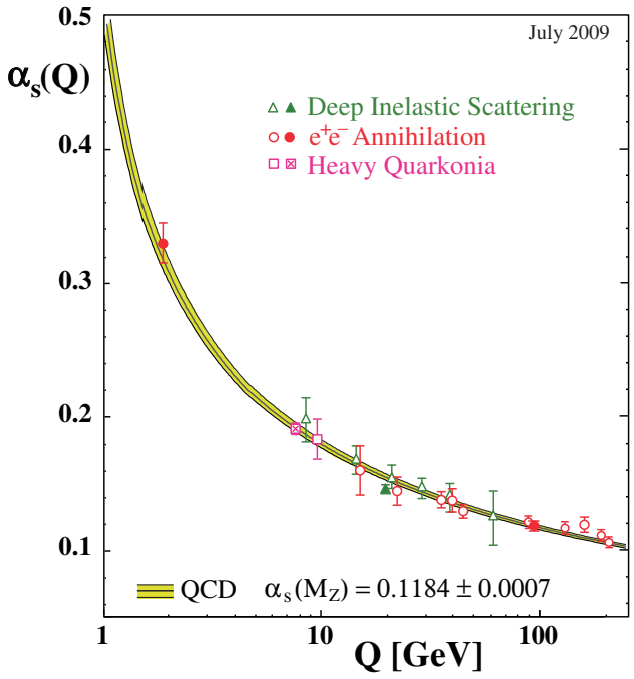

Figure 2.4.: The running coupling constant of QCD as a function of the energy scale Q [3]

interactions, observe isolated from other particles? Is there a way to unambiguously define the concept of quark masses and if so how are these theoretical definitions related to the quantities measured in experiment? These issues are addressed in Section 2.1.3.

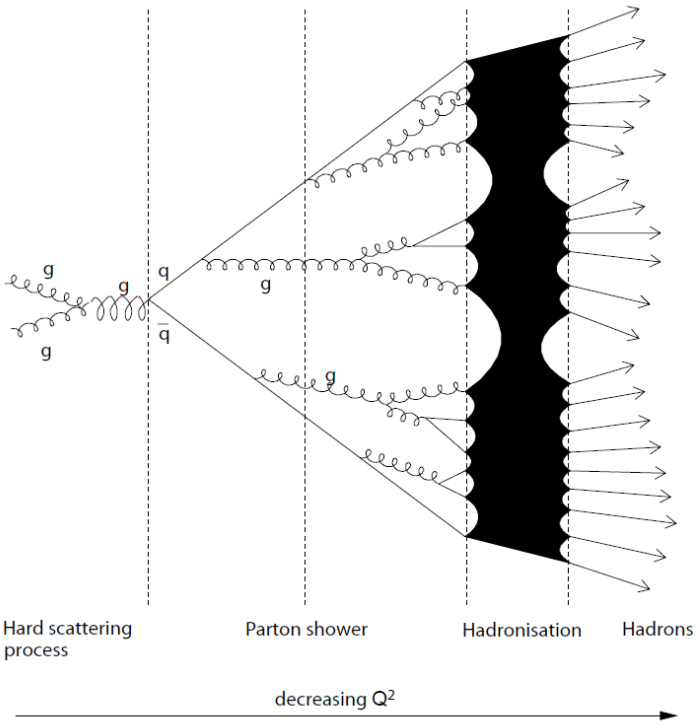

Figure 2.5.: Schematic representation of parton and hadron shower triggered by final-state partons [15]

- The final-state quarks from a hard-scattering process cannot directly be observed in the detector, as explained above. Instead, they trigger complex cascades of particles as shown in Figure 2.5: The individual quarks emerging from the hard scattering process generate **parton showers** by radiating gluons which in turn split into gluons or pair of quark and anti-quark according to the vertices in Figure 2.2. During **hadronisation** new particles are created from the vacuum to form colourless bound-states (**hadrons**) which can be either pair of quark and anti-quark (**mesons**) or triple-quark bound-states (**baryons**). This process continues until all coloured particles are absorbed into hadrons. The unstable hadrons finally decay into stable[7] particles such as protons or neutrons. Thus, one single final-state parton from a hard-scattering process results in a whole bunch of stable hadrons which can be observed in the detector. The correct kinematic reconstruction of these **hadronic jets**, in particular the determination of their energy, and the identification of the final-state parton that triggered a jet is a non-trivial task. It is, however, of fundamental importance for the identification and full kinematic reconstruction of the original hard-scattering process and therefore poses a major challenge to all physics analyses at hadron colliders. For further details on jet reconstruction see Section 5.4.

- The aforementioned evolution of hadronic jets from single partons can not (yet) be calculated completely from the theory: For the parton shower, approximative methods such as Next-to-Leading Order (NLO) calculations and Next-to-Leading-Log Approximations (NLLA) are available [16] while for hadronisation only phenomenological models exist. These generally fall into two categories:

  - **String Models**: The strong interaction between two coloured partons in the shower is described by a colour flux tube or string with tension $\kappa \approx 1 \frac{\text{GeV}}{\text{fm}}$ [16, 17]. The energy stored in the string therefore increases linearly with the distance until it breaks up producing a pair of quark and anti-quark that forms colourless mesons with the original partons. This model, known as *linear confinement model*, makes explicit use of the energy dependence of the strong coupling constant and is supported by lattice QCD studies.[17]

  - **Cluster Models**: The coloured particles in the parton shower are grouped with their nearest neighbours into clusters without a net colour. These clusters are treated as quasi-particles that then decay into hadrons.

  Monte-Carlo generators generally use either one of these two models to simulate hadronisation processes. For example, the Monte-Carlo generator Pythia [17] relies on the string model while Herwig [18] uses the cluster approach.

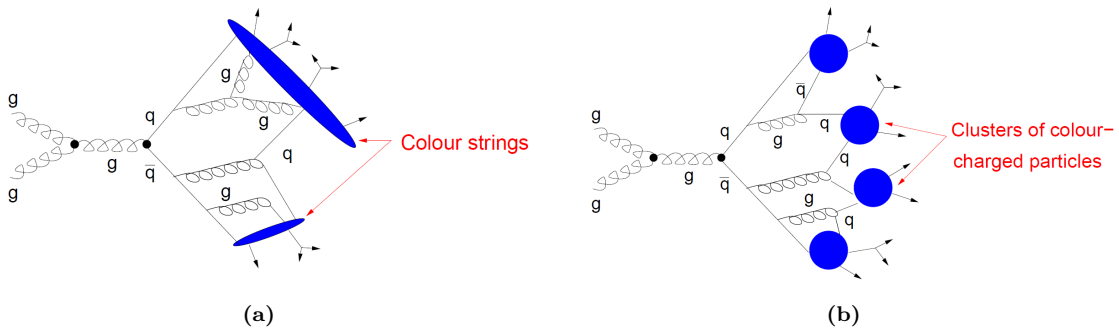

Figure 2.6.: Phenomenological models of hadronisation: (a) string model and (b) cluster model [19]

[7] In this context, the term "stable" refers to all particles that do not decay within the detector.

2.1.3. The Concept of Quark Masses

As explained in Section 2.1.2, quarks cannot be observed as free particles due to confinement, a direct consequence of their very nature as particles carrying a colour quantum number. This poses a major problem for both theory and experiment when it comes to defining and measuring quark masses.
There are various approaches to tackle this issue, each with its own set of approximations and systematic errors, and quark masses can differ significantly depending on which conventions and definitions are used. Therefore, it is important to always keep the (gauge) theoretical framework in mind, and special care must be taken when theoretical concepts are to be related to experimentally measured quantities.

A reasonable starting point for addressing the problem of the quark masses is, naturally, at the fundamental level of the QCD Lagrangian which contains the quark masses as parameters that take finite values after renormalisation. This implies that, beyond leading-order QCD, the quark masses depend on the chosen renormalisation scheme and the energy parameter μ of the renormalisation. Conventionally, the so-called **Modified Minimal Subtraction scheme $\overline{\text{MS}}$** is chosen[8] and the energy scale μ is fixed at either $\mu = 1$ GeV or $\mu = 2$ GeV for light quarks (d, u, s) while for the charm and bottom quark it is customary to choose $\mu = \overline{m}_c$ and $\mu = \overline{m}_b$.[3]

There is, however, an alternative mass concept that is sometimes used to define quark masses: the **pole mass**[9]. This definition has been adapted from QED where it applies to free particles such as the electron. For these, the position of the pole in the propagator (or, to be more precise, its real part) defines the mass of the particle.
In Quantum Chromodynamics, this mass concept can be used as a perturbative definition of the quark mass but with only a limited accuracy due to the non-perturbative effects that are characteristic for QCD. In fact, the full quark propagator of QCD does not have a pole. Therefore, the pole mass is not a physical quantity and has only very limited applicability.
The relation between m_Q^{pole} and $\overline{m}_Q$ is known up to three loops in perturbation theory.[3]
One might expect that the above complications resulting from confinement do not, or at least only in a limited way, apply to the top quark: Due to its huge mass, the top quark has an extremely short lifetime of $0.5 \cdot 10^{-24}$ s and a corresponding width of 1.29 GeV [3] which is larger than the QCD energy scale $\Lambda_{QCD} \approx 200$ MeV, meaning that its lifetime is shorter than the timescale for hadronisation. Therefore, top quarks decay before they can form hadrons, in other words, they are not found to be confined into colourless bound-states because their lifetime is not sufficient for them to form any. It might therefore be hoped that the top quark pole mass does not suffer from the above-mentioned ambiguity.
However, it can be shown [20] that this is not the case and that in fact the intrinsic $\mathcal{O}(\Lambda_{QCD})$ ambiguity of the pole mass applies to any coloured particle, no matter whether stable or unstable and independent of its lifetime. It has therefore been suggested (see again [20]) to use $\overline{MS}$ mass as the standard top mass concept with regard to the increasing precision of top quark mass measurements that will at some point reach an accuracy comparable to Λ_{QCD}.

Apart from the theoretical difficulties of defining appropriate concepts for the masses of quarks, there is still the question how these can be related to the quantities measured in experiments.
In the case of the top quark, there are basically two ways to perform a direct mass measurement based on the analysis of the final states in $t\bar{t}$ events.

- **Template Methods**: Monte Carlo generators are used to produce a set of templates with different input values of $m_{\text{top}}^{\text{MC}}$. These are compared to data on the basis of the distributions

[8] It should be noted that analyses of inclusive B meson decays indicate that different schemes such as the 1S or PS scheme might be better suited, at least for heavy quarks. [3]
[9] This quantity is conventionally denoted by m_Q^{pole} as opposed to the $\overline{MS}$ mass $\overline{m}_Q$.

of a number of chosen kinematic variables and the top quark mass is extracted from this template fit.

- **Calibration Curve Methods**: The value of a chosen mass estimator is calculated from measured final-state observables in data. The same procedure is applied to a number of Monte Carlo datasets generated with different input values of $m_{\text{top}}^{\text{MC}}$ which allows to determine the functional relation between the "true" (i.e. generated) and the reconstructed top quark mass $m_{\text{top, reco}}(m_{\text{top, truth}})$. The mass obtained from data is then re-calibrated on the basis of the thereby obtained calibration curve.

The obvious complication with both of these methods is that they fundamentally rely on the quark mass concept $m_{\text{top}}^{\text{MC}}$ used by the Monte Carlo generator which does not relate directly to a particular renormalisation scheme.
To deal with this source of uncertainty, $t\bar{t}$ cross-section measurements[10] are compared to fully inclusive higher-order QCD calculations while either assuming that $m_{\text{top}}^{\text{MC}} = \overline{m}_t$ or $m_{\text{top}}^{\text{MC}} = m_{\text{top}}^{\text{pole}}$ ([21, 22, 23]). Results from the DØ experiment [23] indicate that the top mass measured at TeVatron - which dominates the current world-average of the top-quark mass as quoted in [1] - is closer to $m_{\text{top}}^{\text{pole}}$ than to $\overline{m}_t$.

2.1.4. Electroweak Interactions and Spontaneous Symmetry Breaking

The relevance of top quark physics in general and precision measurements of the top quark mass in particular can only be fully understood in the context of the theory of electroweak interactions, represented by the $SU(2)_L \times U(1)_Y$ term in Equation (2.1).
As outlined before in the cases of QED and QCD (Sections 2.1.1 and 2.1.2), the requirement that the Lagrangian be invariant under the actions of the elements of the respective symmetry group yields the existence of two gauge fields:
A triplet W_μ^i with $i \in \{1, 2, 3\}$ for $SU(2)_L$ and a singlet B_μ in the case of $U(1)_Y$. The corresponding quantum numbers are the **weak isospin** I and the **weak hypercharge Y**, respectively.
The concept of weak isospin is intimately related to that of chirality[11]: A fermion is called *left-handed* if its Dirac spinor Ψ is an eigenstate of the chirality operator $P_L = \frac{1}{2}(1 - \gamma^5)$ and *right-handed* if it is an eigenstate of the chirality operator[12] $P_R = \frac{1}{2}(1 + \gamma^5)$. For an anti-particle these definitions are simply reversed. A general Dirac spinor can be written as the sum of left- and right-handed components:

$$\Psi = P_L\Psi + P_R\Psi = \Psi_L + \Psi_R \tag{2.12}$$

In the context of electroweak gauge theory, the left-handed fermions form isospin doublets with isospin $I = \frac{1}{2}$ and third component $I_3 = \pm\frac{1}{2}$ while the right-handed fermions are isospin singlets (I = 0). In the case of anti-particles the situation is simply reversed for left- and right-handed states. The gauge fields W_μ^i, which form an isospin triplet[13] ($I = 0$), exclusively couple to left-handed fermions (hence the index "L" in $SU(2)_L$) and right-handed antifermions which means that parity is maximally violated. The fact that the W_μ^i themselves also carry isospin is a direct consequence of the non-Abelian nature of $SU(2)$ and, like in the case of $SU(3)$, implies gauge-field self-coupling. The weak hypercharge to which the B_μ couples can be calculated for each particle using the **Gell-Mann-Nishijima formula**:

$$Q_{em} = I_3 + \frac{1}{2}\, Y. \tag{2.13}$$

Table 2.1 summarizes the quantum numbers for the fermions of the first generation. The same numbers apply to the fermions of the other two families.

[10] Unlike inclusive observables such as the top-quark mass, the cross section is a fully inclusive quantity, i.e. one that is sensitive to kinematic or topological properties of the final state, and as such has a smaller sensitivity to α_s.
[11] This term is derived from the Greek word $\chi\varepsilon\acute{\iota}\rho$ meaning "hand".
[12] The quantity $\gamma^5 = i\gamma^0\gamma^1\gamma^2\gamma^3$ is the product of the four Dirac matrices γ^i.
[13] This is in full analogy to the gluon octet of QCD.

	Q_{em}	I_3	Y
$(\nu_e)_L$	0	$\frac{1}{2}$	-1
e_L	-1	$-\frac{1}{2}$	-1
$(\nu_e)_R$	0	0	0
e_R	-1	0	-2

(a) Leptons

	Q_{em}	I_3	Y
u_L	$\frac{2}{3}$	$\frac{1}{2}$	$-\frac{1}{3}$
d_L	$-\frac{1}{3}$	$-\frac{1}{2}$	$-\frac{1}{3}$
u_R	$\frac{2}{3}$	0	$\frac{4}{3}$
d_R	$-\frac{1}{3}$	0	$-\frac{2}{3}$

(b) Quarks

Table 2.1.: Quantum numbers of the electroweak theory for the fermions of the first generation

The gauge fields of the known gauge bosons, the $W_\mu^\pm$, Z_μ^0 and $\mathcal{A}_\mu$ for the photon, can be obtained by forming linear combinations of the aforementioned gauge fields as follows:

$$W^\pm = \frac{1}{2}(W_\mu^1 \mp iW_\mu^2)$$

$$Z_\mu^0 = -B_\mu \ \sin\theta_W + W_\mu^3 \ \cos\theta_W$$

$$\mathcal{A}_\mu = B_\mu \ \cos\theta_W + W_\mu^3 \ \sin\theta_W \tag{2.14}$$

where θ_W is known as the weak mixing angle.
The linear combinations $W^\pm$ act as ladder operators on the weak isospin doublets in Figure 2.1: A left-handed down-type quark turns into its up-type isospin partner by absorbing a W^+, e.g.

$$s_L + W^+ \to c_L,$$

and a left-handed up-type quark vice-versa turns into its down-type isospin partner by emitting a W^+, e.g.

$$t_L \to W^+ + b_L.$$

Thus, the weak interaction allows changes of quark flavour.
The caveat of the electroweak theory in the formulation outlined so far is that the requirement of gauge invariance can only be met if the gauge fields are massless. While this is indeed the case for the photon field $\mathcal{A}_\mu$, the $W^\pm$ and Z^0 bosons found in nature have considerable masses of 80.4 GeV and 91.2 GeV, respectively.[14]
This problem can be solved by introducing a scalar field Φ with a non-vanishing vacuum expectation value $\langle\Phi\rangle_0$ and a potential $V(\Phi^\dagger\Phi)$ that is invariant under $SU(2)_L \times U(1)_Y$ but has a ground state which does not possess this symmetry.
In the so-called *Minimal Standard Model* Φ takes the form of a complex $SU(2)_L$ doublet with hypercharge $Y(\Phi) = 1$

$$\Phi = \begin{pmatrix} \phi^+ \\ \phi^0 \end{pmatrix} = \frac{1}{\sqrt{2}} \begin{pmatrix} \phi_1 + i\phi_2 \\ \phi_3 + i\phi_4 \end{pmatrix} \qquad \begin{matrix} I_3 = +\frac{1}{2} \\ I_3 = -\frac{1}{2} \end{matrix} \tag{2.15}$$

[14] Theorists were fully aware of this problem when the model for electroweak unification was introduced in 1961. Even though the $W^\pm$ and Z^0 had not been discovered yet, theoretical considerations indicated that they should be heavy. S. Glashow, one of the "fathers" of the electroweak unification, admitted: "It's a stumbling block we must overlook." The problem was only solved six years later when S. Weinberg and A. Salam suggested the Higgs mechanism of spontaneous symmetry breaking. [13]

which possesses four real, scalar degrees of freedom, the ϕ_i, and groundstates Φ_0. These are commonly expressed in the form

$$\Phi_0 = \frac{1}{\sqrt{2}} \begin{pmatrix} 0 \\ v \end{pmatrix} \tag{2.16}$$

where $v = \frac{\mu}{\lambda}$ is a real parameter related to the potential $V(\Phi^\dagger\Phi)$ which in the context of this minimal model is given by:

$$V(\Phi^\dagger\Phi) = -\mu^2\Phi^\dagger\Phi + \lambda^2(\Phi^\dagger\Phi)^2, \qquad \mu, \lambda \in \mathbb{R}. \tag{2.17}$$

The value of v can be estimated from precision measurements of electroweak observables. A single vacuum groundstate Φ_0 does not possess the $SU(2)_L \times U(1)_Y$ symmetry of the complete electroweak Lagrangian (including the additional terms for the Higgs field). This means that when the system is in one of its possible ground states (the collection of which *does* possess $SU(2)_L \times U(1)_Y$ symmetry), the full underlying symmetry of the Lagrangian is hidden. This phenomenon is known as **spontaneous symmetry breaking**.
During spontaneous symmetry breaking, the gauge fields corresponding to the $W^\pm$, Z^0 aquire mass by "absorbing" three of the four degrees of freedom of Φ. The photon gauge field A_μ remains massless and the remaining fourth degree of freedom leads to a scalar field with mass

$$m_H = \sqrt{2}\mu = \sqrt{2}\lambda v, \tag{2.18}$$

the **Higgs field**. In group-theoretical terms, this process can be described as

$$SU(2)_L \times U(1)_Y \to U(1)_{em}, \tag{2.19}$$

where $U(1)_{em}$ is the familiar gauge group of QED.

The Higgs mechanism does not only reconcile the local gauge invariance of the unified electroweak theory with the observed masses of the weak gauge bosons, it also able to describe the fermion masses via Yukawa coupling of the scalar field Φ to the chiral Dirac spinor fields of the fermions:

$$\mathcal{L}_{HF} = \tilde{g}_f(\bar{\Psi}^f_R\Phi^\dagger\Psi^f_L + \bar{\Psi}^f_L\Phi\Psi^f_R) \tag{2.20}$$

where

$$\tilde{g}_f = \frac{\sqrt{2}\ m_f}{v} \tag{2.21}$$

is the Yukawa coupling constant for the fermion f.

Like the value of the Higgs mass m_H, the Yukawa coupling constants $\tilde{g}_f$ - and therefore the fermion masses m_f - are not predicted by the theory but have to be obtained from experiments.
The value of the parameter v, known as the **scale of electroweak symmetry breaking**, can be estimated from precision measurements of electroweak observables to be about 246 GeV. [13]

2.1.5. Overview of the Standard Model Particles and their Properties

The particles and forces of the Standard Model and their properties, as outlined in Sections 2.1.1, 2.1.2 and 2.1.4, can be summarized as follows:

The three fundamental forces described within the gauge theoretical framework of the Standard Model are the **strong, weak and electromagnetic interactions**. The quanta of the corresponding gauge fields are bosonic particles, i.e. they have integer spin. Their properties are summarised in Table 2.2.

The second class of particles contained within the Standard Model are the quanta of the fermion fields: All the Standard Model fermions are spin-$\frac{1}{2}$ particles and fall into either one of two categories, depending on their colour charge:

	strong	**weak**		**electromagnetic**
intermediate gauge bosons	g	$W^{\pm}$	Z^0	γ
spin	1	1		1
mass [GeV]	0	80.4	91.2	0
interaction length [m]	10^{-15}	10^{-18}		∞
electric charge [e]	0	± 1	0	0
colour charged	yes	no		no
chiral sensitive	no	yes		no
couples to	colour	weak isospin		electric charge

Table 2.2.: The three fundamental interactions of the Standard Model and their properties with masses taken from [3]

Leptons (Table 2.7) do not carry a colour charge and therefore do not couple to gluons. As a consequence, they can be observed as free particles and their masses can be defined without the ambiguities related to quark masses (Section 2.1.3).

Generation	**Flavour**	**Symbol**	$\mathbf{Q_{em}}[e]$	**Mass [GeV]**
1	**Electron**	e^-	-1	$511.0 \cdot 10^{-6}$
	Electron Neutrino	ν_e	0	$< 2 \cdot 10^{-9}$
2	**Muon**	μ^-	-1	$105.7 \cdot 10^{-3}$
	Muon Neutrino	ν_μ	0	$< 0.19 \cdot 10^{-3}$
3	**Tau**	τ^-	-1	1.777
	Tau Neutrino	ν_τ	0	$< 18.2 \cdot 10^{-3}$

Figure 2.7.: Leptons and their properties with masses taken from [3]. The limits on the neutrino masses stem from direct measurements.

Quarks (Table 2.8) are "coloured" particles that couple to gluons. Hence they are subject to confinement and cannot be observed as free particles.

Generation	**Flavour**	**Symbol**	$\mathbf{Q_{em}}[e]$	**Mass [GeV]**
1	**Down**	d	$-\frac{1}{3}$	$(5.0^{+0.7}_{-0.9}) \cdot 10^{-3}$
	Up	u	$+\frac{2}{3}$	$(2.5^{+0.6}_{-0.8}) \cdot 10^{-3}$
2	**Strange**	s	$-\frac{1}{3}$	$(100^{+30}_{-20}) \cdot 10^{-3}$
	Charm	c	$+\frac{2}{3}$	$1.29^{+0.05}_{-0.11}$
3	**Bottom**	b	$-\frac{1}{3}$	$4.19^{+0.18}_{-0.06}$
	Top	t	$+\frac{2}{3}$	172.9 ± 0.6 (stat.) ± 0.8 (sys.)

Figure 2.8.: Quarks and their properties with masses taken from [3] and [1]

All quark masses except that of the top quark are $\overline{MS}$ masses, evaluated at renormalization scale $\mu = 2$ GeV for the down, up and strange quark, at $\mu = \overline{m}_c$ for the charm and at $\mu = \overline{m}_b$ for the bottom quark. The top quark mass is based on a combination of data from TeVatron Run I and Run II as provided by the TeVatron Electroweak Working Group (TEVEWWG) [1].

Both quarks and leptons can be grouped into three *families*. All quantum numbers such as spin and charge are identical for corresponding particles from different families such as the up-type quarks u, c and t; only their masses are different.
The fermion mass eigenstates, denoted by d, s, b, ..., used in the classification above are, however, not identical to the weak isospin eigenstates in Section 2.1.4, denoted by d', s', b', ..., on which the $W^{\pm}$ act as ladder operators.
In the quark sector, the relation between these two sets of states is given by a unitary 3×3 matrix, the **Cabibbo-Kobayashi-Maskawa (CKM) matrix $\mathbf{V_{CKM}}$**[15]:

$$\begin{pmatrix} d' \\ s' \\ b' \end{pmatrix} = \begin{pmatrix} V_{ud} & V_{us} & V_{ub} \\ V_{cd} & V_{cs} & V_{cb} \\ V_{td} & V_{ts} & V_{tb} \end{pmatrix} \begin{pmatrix} d \\ s \\ b \end{pmatrix}. \tag{2.22}$$

This implies that the exchange of a $W^{\pm}$ boson does not only allow changes of flavour within the same isospin doublet and therefore within the same generation - which would be the case if V_{CKM} was unitary - but also inter-generational transitions such as[16] $s \to W^+ + u$ or $t \to W^+ + s$.
The matrix elements $|V_{ij}|^2$ correspond to the transition rates between an up-type quark q_i and a down-type quark q_j. Their numerical values are not predicted by the Standard Model but have to be determined experimentally. The measured values as given in [3] are:

$$V_{CKM} = \begin{pmatrix} 0.97428 \pm 0.00015 & 0.2253 \pm 0.0007 & 0.00347^{+0.00016}_{-0.00012} \\ 0.2252 \pm 0.0007 & 0.97345^{+0.00015}_{-0.00016} & 0.0410^{+0.0011}_{-0.0007} \\ 0.00862^{+0.00026}_{-0.00020} & 0.0403^{+0.0011}_{-0.0007} & 0.999152^{+0.000030}_{-0.000045} \end{pmatrix} \tag{2.23}$$

[15] The equivalent to the CKM matrix in the lepton sector is the Pontecorvo-Maki-Nakagawa-Sakata (PMNS) matrix which was introduced in order to explain neutrino oscillations.

[16] This process was first postulated by N. Cabibbo in 1963 who introduced the two-dimensional equivalent to the CKM matrix, the Cabibbo matrix, in order to explain the decay of the K^-, the lightest strange particle. This led to the development of the GIM mechanism and the postulation of the charm quark by S. Glashow, J. Iliopolus and N. Maiani in 1970. [13]

2.2. Relevance of the Top Quark for the Standard Model and Beyond

In the context of the electroweak theory outlined in Section 2.1.4, the importance of the top quark with its unusually high mass becomes fully evident:
In the $SU(2)_L \times U(1)_Y$ gauge theory, as in any quantum field theory, higher-order radiative corrections to scattering processes have to be taken into account perturbatively because they have measurable effects on quantities such as cross sections and masses.[17] While the radiative contributions from **heavy** particles are negligible in QED and QCD, the Yukawa structure of the electroweak theory implies that these contributions have measurable effects.
In particular, this allows experiments to trace particles with masses considerably higher than the centre-of-mass energy at which a particular experiment operates, thus allowing to probe their properties without observing them directly.
This remarkable feature of the $SU(2)_L \times U(1)_Y$ theory made it possible to constrain the mass of the top quark to a range of 173^{+18}_{-20} GeV even before its discovery at TeVatron in 1995 by using precision measurements performed at the Large Electron-Positron collider (LEP). [24]

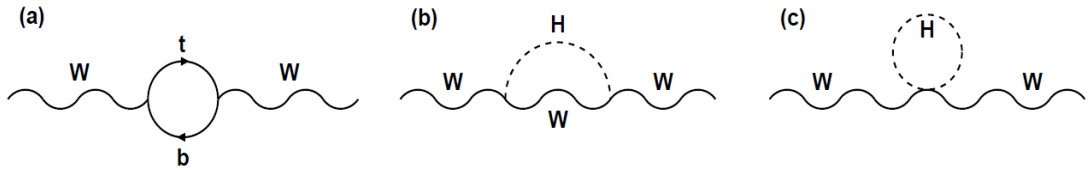

Figure 2.9.: Loop contribution of the top quark and the Higgs boson to the W-boson propagator [25]

In the same way, a combination of precision measurements of the top quark and W-boson masses yields constraints on the mass of the (yet) unobserved Higgs boson by taking into account the radiative corrections of the top quark and Higgs boson to the W-boson propagator (Figure 2.9) and vice versa.

As shown in Figure 2.10, the correlation between the top-quark mass m_{top} and the W-boson mass m_W is approximately linear for different values of the Higgs mass m_H. The grey bands correspond to the sets of linear functions $m_W(m_{\text{top}})$ for values of m_H in the range between 115 GeV and 1000 GeV that have not yet been excluded by theoretical considerations or experimental results: The lower limit of 115 GeV corresponds to the upper bound of the Higgs-mass range that has been excluded via direct searches at LEP and the upper limit is the upper theoretical limit on m_H. The white band between 127 GeV and 600 GeV corresponds to the mass range excluded by direct searches at TeVatron and the LHC. The red area is derived from indirect electroweak fits using precision data taken at LEP1 and SLD.[18]

The orange and green ellipses mark the points in the m_{top}-m_W-plane that are in agreement with the combined data taken at LEP and TeVatron, based on analyses published in 2009 and 2012, respectively. They clearly illustrate how the increasing precision on the W-boson mass leads to stricter (indirect) constraints on the mass of the Higgs boson. The remarkable agreement between the ellipses and the grey band between 115 and 127 GeV points towards a light Higgs boson. In the case of its discovery and a subsequent direct measurement of its mass, the indirect constraints

[17] A prominent example for such a radiative effect is the Lamb shift which can be probed by precision measurements of the hydrogen atom and is correctly predicted within the framework of QED by taking into account higher-order loop diagrams.
[18] This is the acronym of the SLAC Large Detector experiment at the Stanford Linear Accelerator Center (SLAC).

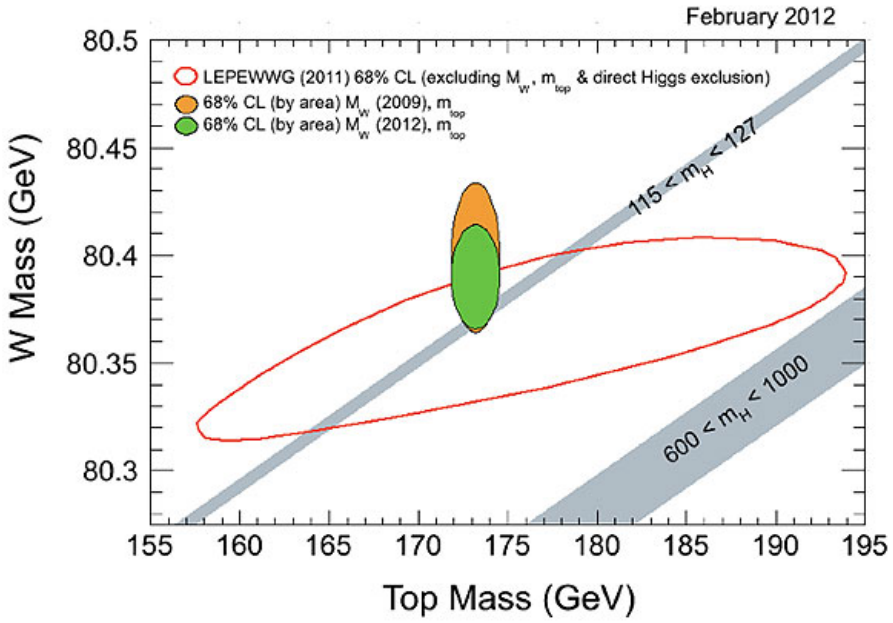

Figure 2.10.: Constraints on the Higgs mass from precision measurements of the W-boson and top-quark mass as of February 2012 [26]

from precision measurements of the W-boson and top-quark masses will serve as an important cross-check.

Moreover, the top quark itself might play a more fundamental role in the context of electroweak symmetry breaking, being the only known particle with a mass close to the electroweak scale v (Section 2.1.4) and a Yukawa coupling to the Higgs field $\tilde{g}_t = \frac{\sqrt{2}\ m_{\text{top}}}{v}$ close to unity.

The top-quark mass might also be sensitive to signatures of physics beyond the standard model (BSM) via radiative contributions from heavy exotic particles and some BSM theories also predict decays of heavy unstable particles into top quarks.

Finally, $t\bar{t}$ events form a major background in many searches for new physics and therefore need to be understood in all thoroughness.

All this calls for a detailed study of the top quark in general and a precise measurement of its mass in particular.

3. Top-Quark Production and Decay

3.1. Top-Quark Production

In the Standard Model, top quarks can be produced either via the strong or the electroweak interaction, see Sections 3.1.1 and 3.1.2. Both production mechanisms play a role in mass measurements as signal and background processes, respectively.

3.1.1. Single-Top Production via Electroweak Processes

Single top quarks can only be produced via the electroweak interaction which allows the creation of quark flavour via the exchange of a W-boson. The leading-order Feynman diagrams for single-top production are shown in Figure 3.1.[1]

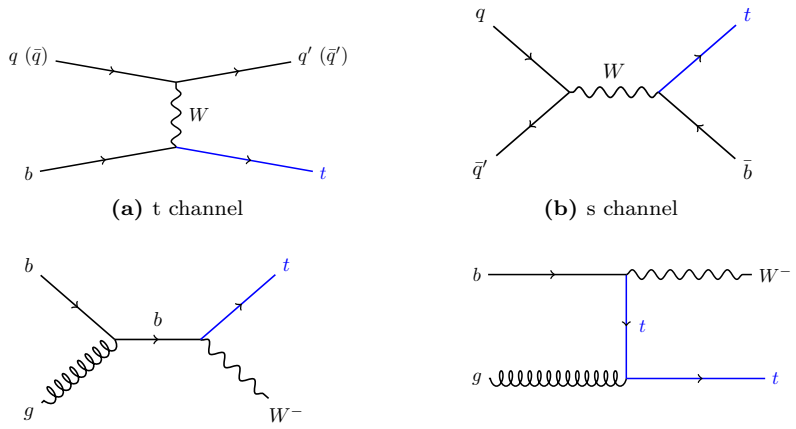

(a) t channel

(b) s channel

(c) Wt channel

Figure 3.1.: Leading-order single-top production

In the **t-channel**, a bottom quark turns into a top quark by exchanging a virtual W-boson with an up-type quark q (or anti-quark $\bar{q}$). This process is the dominant mechanism for single-top production at both the TeVatron ($\sqrt{s} = 1.96$ TeV) and the LHC ($\sqrt{s} = 7$ TeV) with respective

[1] These diagrams exist, of course, in an analogous form for the production of single anti-top quarks. The cross sections stated in the following comprise the production of both single top quarks and single anti-top quarks.

NNLO approximative cross sections [27]

$$\sigma^{\text{NNLOapprox}}_{\text{st\_t-channel}}(m_{\text{top}} = 173\ \text{GeV}, 1.96\ \text{TeV}) = 1.04^{+0.00}_{-0.02} \pm 0.06\ \text{pb}$$

$$\sigma^{\text{NNLOapprox, top}}_{\text{st\_t-channel}}(m_{\text{top}} = 173\ \text{GeV}, 7\ \text{TeV}) = 41.7^{+1.6}_{-0.2} \pm 0.8\ \text{pb}$$

$$\sigma^{\text{NNLOapprox, anti-top}}_{\text{st\_t-channel}}(m_{\text{top}} = 173\ \text{GeV}, 7\ \text{TeV}) = 22.5 \pm 0.5^{+0.7}_{-0.9}\ \text{pb}.$$

The first uncertainty stems from a variation of the renormalisation scale between $\mu = \frac{1}{2}\ m_{\text{top}}$ and $\mu = 2\ m_{\text{top}}$ and the second is related to the uncertainty of the parton-distribution functions (PDFs). All cross sections in this and the following subsection are calculated at $\mu = m_{\text{top}}$.

The production cross section for single top and anti-top quarks are the same at TeVatron but differ at the LHC: While in proton-anti-proton collisions (TeVatron) it is equally likely to have a quark and an anti-quark - either as valence or sea quarks - in the initial state, in proton-proton collisions (LHC) anti-quarks can only arise from virtual $q\bar{q}$ fluctuations, i.e. as sea quarks, which makes it much more unlikely to have an anti-quark in the initial state. This asymmetry accounts for the difference in the above cross sections for single-top and anti-top quark production at the LHC.

In the **s-channel**, a pair of quark and anti-quark from the same isospin dublett combines to form a W-boson that subsequently decays into a top (anti-top) and anti-bottom (bottom) quark. This channel has the smallest non-negligible contribution to single top production at both TeVatron and the LHC. The respective cross sections are given according to [28]:

$$\sigma^{\text{NNLOapprox}}_{\text{st\_s-channel}}(m_{\text{top}} = 173\ \text{GeV}, 1.96\ \text{TeV}) = 0.523^{+0.001\ +0.030}_{-0.005\ -0.028}\ \text{pb}$$

$$\sigma^{\text{NNLOapprox, top}}_{\text{st\_s-channel}}(m_{\text{top}} = 173\ \text{GeV}, 7\ \text{TeV}) = 3.1 \pm 0.06^{+0.13}_{-0.10}\ \text{pb}$$

$$\sigma^{\text{NNLOapprox, anti-top}}_{\text{st\_s-channel}}(m_{\text{top}} = 173\ \text{GeV}, 7\ \text{TeV}) = 1.42 \pm 0.01^{+0.06}_{-0.07}\ \text{pb},$$

Like for the t-channel, the production cross section for single anti-top quarks at the LHC is again smaller than that for single top quarks. In this case, however, the reason lies in the higher number of up-quarks compared to the number of down-quarks among the valence quarks of the proton. This leads to a higher probability of W^+-production compared to W^--production (see Figure 3.1b) and hence to a higher number of top quarks compared to anti-top quarks in the final state.

Finally, single top quarks can be produced in association with W-bosons (**Wt-channel**), a process that is negligible at TeVatron but yields a significant contribution to the overall single-top production cross section at the LHC (see [29]):

$$\sigma^{\text{NNLOapprox}}_{\text{st\_Wt-channel}}(m_{\text{top}} = 173\ \text{GeV}, 7\ \text{TeV}) = 7.8 \pm 0.02^{+0.5}_{-0.6}\ \text{pb}$$

which is the same for single-top and anti-top quark production because the initial state bottom and anti-bottom quarks can only arise from $b\bar{b}$ fluctuations within both protons and anti-protons and therefore occur with equal probability.

3.1.2. Top-Pair Production via the Strong Interaction

The dominant production mechanism for top quarks at hadron colliders is, naturally, via the strong interaction. Since these processes do not allow changes of quark flavour, top quarks can only be

produced in pairs, i.e. together with their anti-particle.[2]
The leading-order Feynman diagrams for strong top pair production are shown in Figure 3.2.

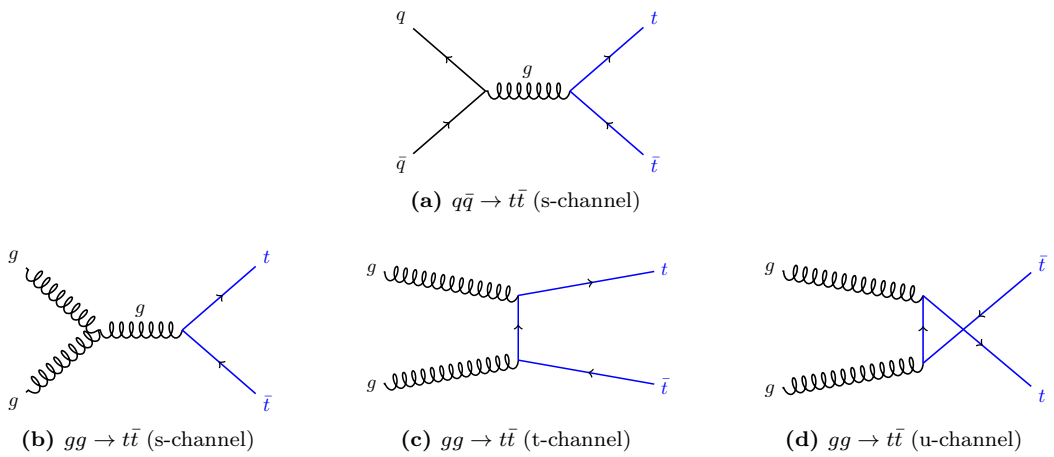

(a) $q\bar{q} \to t\bar{t}$ (s-channel)

(b) $gg \to t\bar{t}$ (s-channel)

(c) $gg \to t\bar{t}$ (t-channel)

(d) $gg \to t\bar{t}$ (u-channel)

Figure 3.2.: Leading-order $t\bar{t}$ production ($2 \to 2$ processes)

These processes fall into two categories depending on their initial-state partons: **quark-anti-quark annihilation** ($q\bar{q} \to t\bar{t}$; s-channel only) and **gluon-gluon fusion** ($gg \to t\bar{t}$; s-, t- and u-channel). While top pair production at TeVatron is dominated by quark-anti-quark annihilation with about 85% of the total cross section, the situation is just reversed at the LHC. [3]
The reason for this is twofold:

- Firstly, as explained above, both quarks and anti-quarks occur in abundance as valence quarks in proton-anti-proton colliders such as TeVatron. At a proton-proton collider like the LHC, however, anti-quarks can only arise from virtual fluctuations, making it much more unlikely to find a pair of quark and anti-quark with sufficient centre-of-mass energy to produce a top-anti-top pair.

- Secondly, the centre-of-mass energy is significantly higher at the LHC ($\sqrt{s} = 7$ TeV compared to 1.96 TeV at TeVatron) which leads to different shapes of the PDFs compared to the situation at TeVatron. The result is a higher probability of finding a pair of gluons with sufficiently high energy for top-pair production.

In addition to the leading-order $2 \to 2$ processes discussed so far, higher-order diagrams with more than two partons in the final state give non-negligible contributions to the top-pair production cross section. Additional final-state partons may arise from inital-state radiation (ISR) or final-state radiation (FSR) when one of the initial- or final-state partons (due to the gluon self-interaction these can be both quarks *and* gluons) radiates a gluon. This is illustrated in Figure 3.3. These processes are taken into account by general-purpose Monte Carlo generators such as Pythia and Herwig as part of the parton shower.

Moreover, associate production of a top pair with an additional quark or gluon in the final state as shown in Figure 3.4 is possible. These processes are not simulated by all Monte Carlo generators. For many top-quark analyses, however, in particular for precision measurements of the top-quark mass, they need to be taken into account. Therefore, many of these analyses rely on the **M**onte **C**arlo generator MC@NLO [30] which does not only simulate the hard scattering top-pair and single-top production processes at next-to-leading order (**NLO**) such as those in Figure 3.4 but also

[2] Top-quark pairs can also be produced via electroweak processes such as $Z \to t\bar{t}$ or $\gamma \to t\bar{t}$. These are, however, negligible compared to strong pair production due to their smaller gauge coupling.

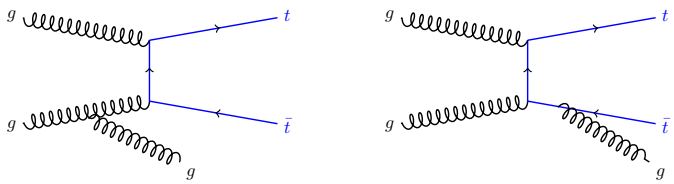

(a) ISR **(b)** FSR

Figure 3.3.: $t\bar{t}$ production with additional final-state partons from (a) initial-state and (b) final-state radiation

takes into account the interference between the different diagrams. MC@NLO is usually interfaced with Herwig to simulate parton showers and hadronisation.[3]

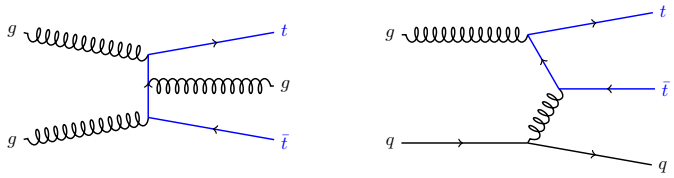

(a) **(b)**

Figure 3.4.: $t\bar{t}$ production with (a) an associated gluon and (b) an associated quark in the final state

The relevance of these higher-order processes, such as those illustrated in Figures 3.3 and 3.4, does not only lie in their contribution to the overall cross section; the additional partons in the final state also lead to additional hadronic jets which complicate the identification of the jets from the top-quark decay and therefore the reconstruction of the event. For details see Section 8.1.

The overall top-pair production cross section including NNLO approximative corrections is

$$\sigma_{t\bar{t}}^{\text{NNLOapprox}}(m_{\text{top}} = 173\ \text{GeV}, 1.96\ \text{TeV}) = 7.08^{+0.00\ +0.36}_{-0.24\ -0.27}\ \text{pb}$$

$$\sigma_{t\bar{t}}^{\text{NNLOapprox}}(m_{\text{top}} = 173\ \text{GeV}, 7\ \text{TeV}) = 163^{+7\ +9}_{-5\ -9}\ \text{pb}$$

at TeVatron and the LHC, respectively. [32] The cross section is more than 20 times higher at the LHC compared to the TeVatron due to its higher centre-of-mass energy. Together with its higher luminosity, this makes the LHC an excellent facility for studying the top quark and justifies the term “top quark factory” that has been coined for it.

Figure 3.5 illustrates the dependence of the top pair production cross section on the top mass both for the LHC and TeVatron. For a given centre-of-mass energy $\sqrt{s}$, the production cross section decreases with increasing top mass because more energy is required to produce a top-anti-top pair. This functional dependence can be used for indirect measurements of the top-quark mass via fully inclusive cross section measurements.

[3] With this setup, it can happen that one of the ISR or FSR processes in Figure 3.3 is simulated both by MC@NLO as part of the hard process and Herwig as part of the parton shower. An overlap removal tool is implemented at generator level to avoid double counting.[31]

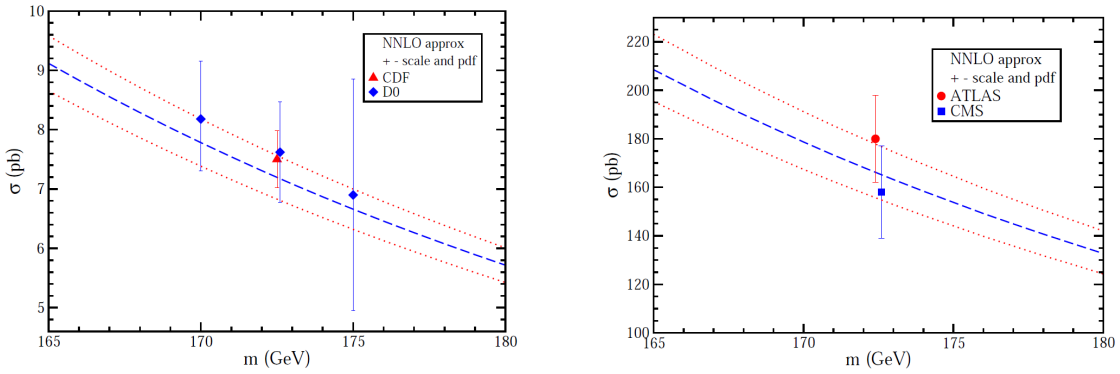

(a) **(b)**

Figure 3.5.: NNLO approximative top pair production cross section as a function of the top mass at the TeVatron (a) and at the LHC (b)

Compared to the combined cross section of the different single-top production channels the top-pair production cross section is more than twice as high which is one reason why most top-quark analyses focus on top-pair rather than single-top events. The other reason is that it is more difficult to identify top quarks in single top events due to a less distinctive event signature and larger background from other processes.[4]

The following analysis therefore uses only top-pair events to reconstruct the top quark and measure its mass. Single-top processes form a part of the physical background (see Section 6).

3.2. Top-Quark Decay

Top quarks decay into lighter quarks via the weak interaction. As explained in Section 2.1.3, with 1.29 GeV the decay width of the top quark is larger than the QCD energy scale $\Lambda_{QCD} \approx 200$ MeV, which means that top quarks decay before they can form hadrons.

In the Standard Model, the top-quark decay channels and their respective probabilites are determined by the CKM matrix (see section 2.1.5): Top quarks decay almost exclusively via

$$t \to W^+ + b$$

with a probability of $|V_{tb}|^2 \approx 99.8\%$, while the decays

$$t \to W^+ + s \qquad \text{and} \qquad t \to W^+ + d$$

with respective probabilities $|V_{tb}|^2 \approx 0.16\%$ and $|V_{tb}|^2 \approx 0.0074\%$ are extremely rare.

The W^+-boson[5] then decays either **leptonically** into a charged lepton and its corresponding neutrino

$$W^+ \to l^+ + \nu_l$$

[4] This also explains why more than ten years elapsed between the discovery of the top quark in top-pair events in 1995 and the observation of single-top events at TeVatron. [33, 34]

[5] The following equally applies to the charge-conjugated case.

where $l \in e, \mu, \tau$, or **hadronically** into a pair of quark and anti-quark

$$W^+ \to q_i + \bar{q}'_j$$

where q_i is an up-type quark and $\bar{q}'_j$ its (down-type) isospin partner.

The branching ratios for the leptonic and hadronic W-boson decays can be estimated as follows: Neglecting the non-diagonal elements of the CKM matrix, i.e. identifying the isospin eigenstates $\bar{q}'_j$ with the mass eigenstates $\bar{q}_j$, there are two possibilities for hadronic W decays: $\mathrm{W}^+ \to u + \bar{d}$ and $\mathrm{W}^+ \to c + \bar{s}$. (The decay $\mathrm{W}^+ \to t + \bar{b}$ is kinematically forbidden.) Since quarks come in three colours and there are three possible leptonic decays, this makes a total of 9 possible W-boson decays, with a branching ratio of $\approx \frac{2}{3}$ for the hadronic and $\approx \frac{1}{3}$ for the leptonic decay channel.

Top-pair events can be classified into three decay channels according to the decays of the W^+ and W^- bosons that stem from the decays of the top and anti-top quark, respectively: Each of these

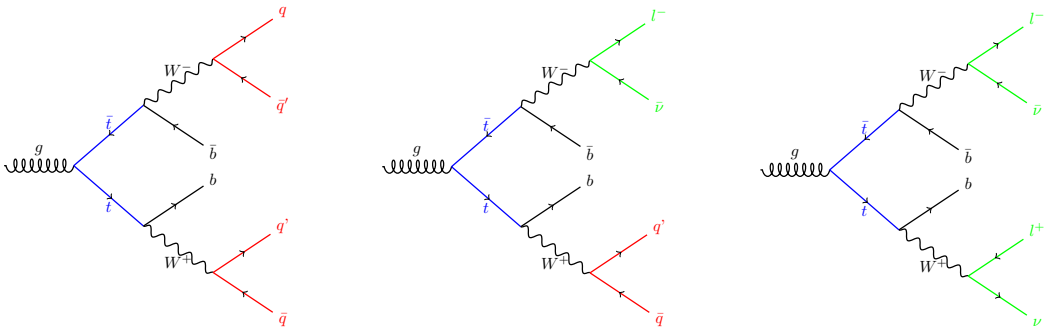

(a) allhadronic **(b)** semileptonic **(c)** dileptonic

Figure 3.6.: Overview of the decay channels for $t\bar{t}$ events

decay channels is characterised by its *detector signature* and corresponding dominant background processes and therefore requires its own specific methods of event selection and reconstruction. Top quark analyses such as the measurements of the top-quark mass are performed separately in all three channels thus providing an excellent opportunity for cross-checks between the different measurements.

All-hadronic/ All-Jets Channel

A $t\bar{t}$ event is called **all-hadronic** if both the W^+- and W^--bosons decay into quarks. The probability for this to happen is roughly $\frac{2}{3} \cdot \frac{2}{3} = \frac{4}{9}$ which makes the all-jets channel the dominant $t\bar{t}$ decay channel and proves very advantageous in terms of statistics. Allhadronic events are characterised by six jets in the final state: four light-quark jets and two b-jets. This does not only make it very hard to distinguish them from QCD multijet events, the dominant source of background in this channel, it also renders the reconstruction of the top quarks a challenging task because the large jet multiplicity makes it hard to correctly identify the jets from each top quark. A further drawback of this channel is the large jet-energy scale (JES) dependence, the uncertainty on the JES being one of the dominant sources of systematic uncertainty on the top-quark mass.

Dileptonic/Dilepton Channel

If both W-bosons decay leptonically, which happens with a probability of roughly $\frac{1}{3} \cdot \frac{1}{3} = \frac{1}{9}$, the event is classified as **dileptonic**. The small branching fraction for this channel results in low statistics

which is a significant drawback for early analyses based on small amounts of data but becomes less significant the more data are taken. The detector signature - two b-quark jets, two isolated, oppositely charged leptons and large missing transverse energy from the two neutrinos - facilitates the identification of dileptonic events and the efficient rejection of background processes such as the QCD multijet background with its large cross section. Hence the overall signal purity in this decay channel is high. The main background stems from events with one Z boson and additional jets in the final state. The reconstruction of the event kinematics, however, is a challenging task because the presence of **two** undetected particles, the two neutrinos, introduces six unknowns, the three momentum components of each neutrino. Five of these can be determined by using additional constraints such as the requirement that the sum of the transverse momenta of all particle in the event has to be zero. Without the top-quark mass as an additional constraint, however, the kinematics of the decay remains undetermined and more sophisticated approaches like matrix element or template methods are needed in order to determine the top-quark mass.

Semileptonic/Lepton + Jets Channel

A $t\bar{t}$ event in which one W-boson decays into leptons and the other into quarks is classified as **semileptonic**. The corresponding branching ratio in the above approximation is $2 \cdot \frac{1}{3} \cdot \frac{2}{3} = \frac{4}{9}$ and therefore comparable to that of the allhadronic channel. The decay W$\rightarrow \tau\nu_\tau$ is normally omitted in semileptonic analyses for two reasons: Firstly, τ-leptons constitute an additional source of missing energy because they decay via the weak interaction according to $\tau \rightarrow W + \nu_\tau$. Secondly, the W-boson arising from the τ decay has, as stated before, a probability of roughly $\frac{2}{3}$ to decay into quarks, thus giving rise to additional jets that further complicate event reconstruction. The detector signature of a semileptonic event, excluding W-boson decays into τ leptons, is characterised by four jets - two light-quark jets and two b-jets -, one isolated charged lepton and missing transverse energy from the neutrino. The main background stems from events with one (leptonically decaying) W-boson and additional jets in the final state. The semileptonic decay channel is often called the **golden channel** for top-quark analyses because, apart from having a reasonably large branching fraction and therefore providing sufficient statistics, the **leptonic branch** can be used to identify (**tag**) the signal events while the **hadronic branch** allows a full reconstruction of the respective top quark which can then be used to measure (**probe**) properties such as its mass.

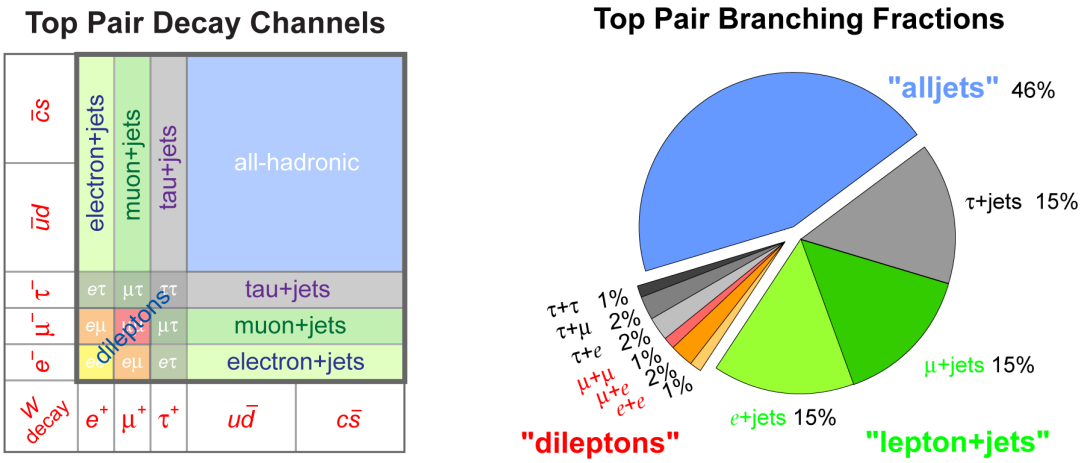

(a) **(b)**

Figure 3.7.: Top-pair decay channels and their respective branching fractions [26]

4. The Large Hadron Collider and the ATLAS Experiment

The huge mass of the top quark implies that considerable amounts of energy are needed for both single-top and top-pair production. These can only be provided by powerful particle colliders where the kinetic energy of highly-accelerated particles can be used to create new, massive particles according to A. Einstein's energy-mass equivalence principle $E = m$.[1]

For top-pair production - the nominal production mechanism for this and most other top-quark analyses - the centre-of-mass energy of the inital-state particles needs to equal or exceed twice the top-quark mass which is roughly 350 GeV. At hadron colliders such as the TeVatron and the LHC, the initial-state partons carry only a fraction x_i of the total energy of the hadron. The effective centre-of-mass energy squared $\hat{s} = E_{cm}^2$ of the parton system is therefore reduced by a factor of $x_a \cdot x_b$ compared to the centre-of-mass energy $\sqrt{s}$ of the colliding hadron beams. The threshold condition for top-pair production at hadron colliders is given by

$$\hat{s} = x_a \cdot x_b \cdot s \geq 4 \cdot m_t^2 \tag{4.1}$$

where the energy fractions x_a and x_b of the partons vary between 0 and 1. The probability of finding a parton with energy fraction x_i is determined by the parton distribution functions (PDFs) of the respective hadron and generally decreases for larger x_i. This implies that most top pairs are created close to the production threshold and consequently with low momentum. It also implies that since most partons are likely to have small energies, the centre-of-mass energy of the collider needs to be considerably higher than the energy threshold of 350 GeV in order to provide a sufficiently large number of events for precision measurements.[2]

Up to date, only two machines powerful enough to produce top quarks have ever been constructed on earth: The TeVatron at Fermilab near Chicago in the United States which operated as a proton-anti-proton collider at a maximum centre-of-mass energy $\sqrt{s} = 1.96$ TeV and the Large Hadron Collider (LHC).

4.1. The Large Hadron Collider

The Large Hadron Collider is a proton-proton collider at the European Organisation for Nuclear Research (CERN[3]) near Geneva in Switzerland. It has been designed to achieve an eventual centre-of-mass energy $\sqrt{s} = 14$ TeV and instantaneous luminosity of 10^{34} cm^{-1} s^{-1} [35] and is currently operating at 7 TeV.[4]

[1] This is given in natural units.

[2] Assuming, for example, that $x_a = x_b = 0.1$, the centre-of-mass energy required to produce a $t\bar{t}$ pair is $E_{cm} = \sqrt{s} = \frac{2m_t}{0.1} \approx 3.5$ TeV.

[3] The acronym stands for "**C**onseil **E**uropéen pour la **R**echerche **N**ucléaire", the French name for the provisional council set up by the 12 original member countries in 1952 in order to pave the way for the European research organisation which was founded in 1954 under the name "Organisation Européenne pour la Recherche Nucléaire" but kept the original acronym by which it is commonly known.

[4] This applies to the 2010 and 2011 data-taking periods. From March 2012, the centre-of-mass energy will be increased to 8 TeV.

The LHC has been built into the (approximately) circular tunnel previously used by the Large Electron-Positron Collider (LEP) which was in operation until 2001. The tunnel lies between 50 and 175 m below the Franco-Swiss border and has a circumference of roughly 27 km (see Figure 4.1).

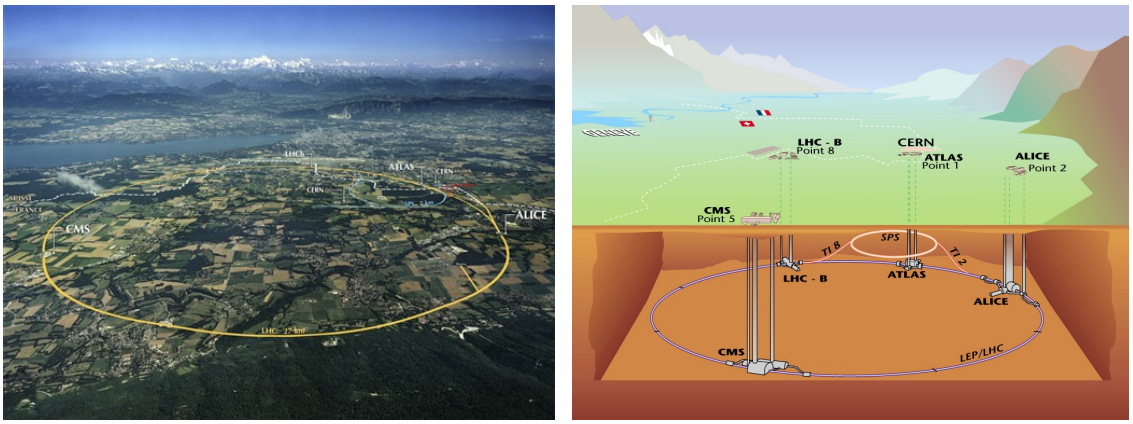

(a) **(b)**

Figure 4.1.: The Large Hadron Collider (LHC) near Geneva, Switzerland: (a) aerial and (b) schematic view [36]

The protons are obtained from the ionisation of hydrogen gas and pass a series of pre-accelerators formed by older, previously independent experiments that have been integrated into the present LHC acceleration chain: Linac2, the Proton Synchrotron Booster (PSB), the Proton Synchrotron (PS) and the Super Proton Synchrotron (SPS) (see Figure 4.2). The pre-accelerated protons are then injected into the LHC with an initial energy of 450 GeV and are further accelerated to reach their peak energy of currently 3.5 TeV per beam. Superconducting dipole and quadrupole magnets, cooled by superfluid helium to below 2 K and designed to operate at fields with a peak strengths above 8 TeV, are used to guide and focus the proton beams [37]. The protons in each beam are separated into bunches of about 10^{11} particles with a bunch spacing of 50 ns.[5]

The beams are brought to collision at four points along the LHC tunnel where the four detectors Alice, ATLAS, CMS and LHCb are situated. The Alice[6] detector was specially developed to record heavy-ion collisions and probe the quark-gluon plasma while LHCb[7] focuses on heavy-flavour physics, in particular on CP violation. ATLAS[8] and CMS[9] have both been designed as all-purpose detectors with the potential to discover new particles such as the Higgs boson or supersymmetric particles but also to probe Standard Model phenomena and perform precision measurements of Standard Model parameters. The fact that there are two independent experiments with similar aims is important because it allows cross-checks between the results, in particular with regard to potential discoveries.

[5] This applies to the data-taking period up to the end of 2011. Test runs with a reduced bunch-spacing of 25 ns have also been performed during that year.
[6] **A** **L**arge **I**on **C**ollider **E**xperiment.
[7] **LHC** **b**eauty.
[8] **A** **T**oroidal **L**HC **A**pparatu**S**.
[9] **C**ompact **M**uon **S**olenoid.

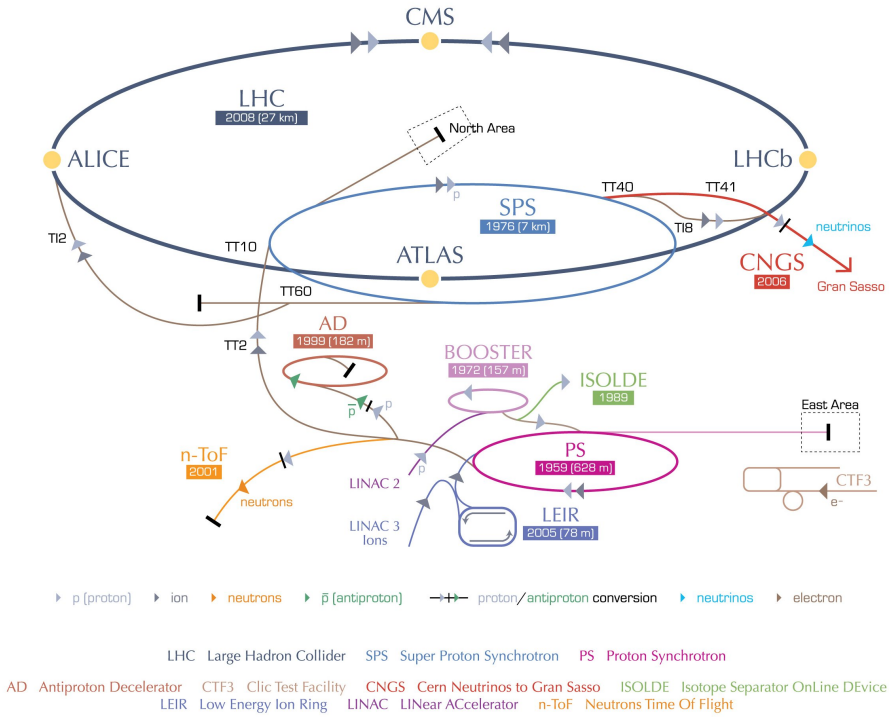

Figure 4.2.: The LHC acceleration chain [36]

4.2. The ATLAS Detector

The ATLAS detector was designed to meet a number of requirements that were dictated by the aim to construct an all-purpose detector which is to work efficiently at a high-energy, high-luminosity hadron collider: The highly-energetic decay products emerging from the beam-collision point into all spatial directions must not escape undetected. Hence an ideal detector must provide a full 4π-coverage around the collision point. In reality, this is not entirely possible since the beam pipe transverses the detector and particles emerging in the direction of the beam pipe are hard to impossible to detect.
The complexity of the interaction and the resulting high particle multiplicity - a direct consequence of the proton being a composite particle - require efficient methods to identify and distinguish between different kinds of particles such as pions and kaons. Moreover, precision measurements call for high-resolution detector components because they rely on an accurate knowledge of the energies and momenta of the particles of interest.
Finally, the high luminosity and resultingly high event rates require fast read-out electronics as well as an efficient trigger system that rejects unwanted hadronic background efficiently and filters out only the events that are of interest for further analyses.

These requirements have led to the construction of a barrel-shaped, left-right symmetric multi-layer detector (see Figure 4.3) centered around the collision point.

With its huge size - 44m in length and 25m in diameter - ATLAS is the biggest of the four detectors at the LHC[10].

[10]It is not, however, the heaviest with "only" 7,000 tons; this title goes to CMS with a weight of 12,500 tons.

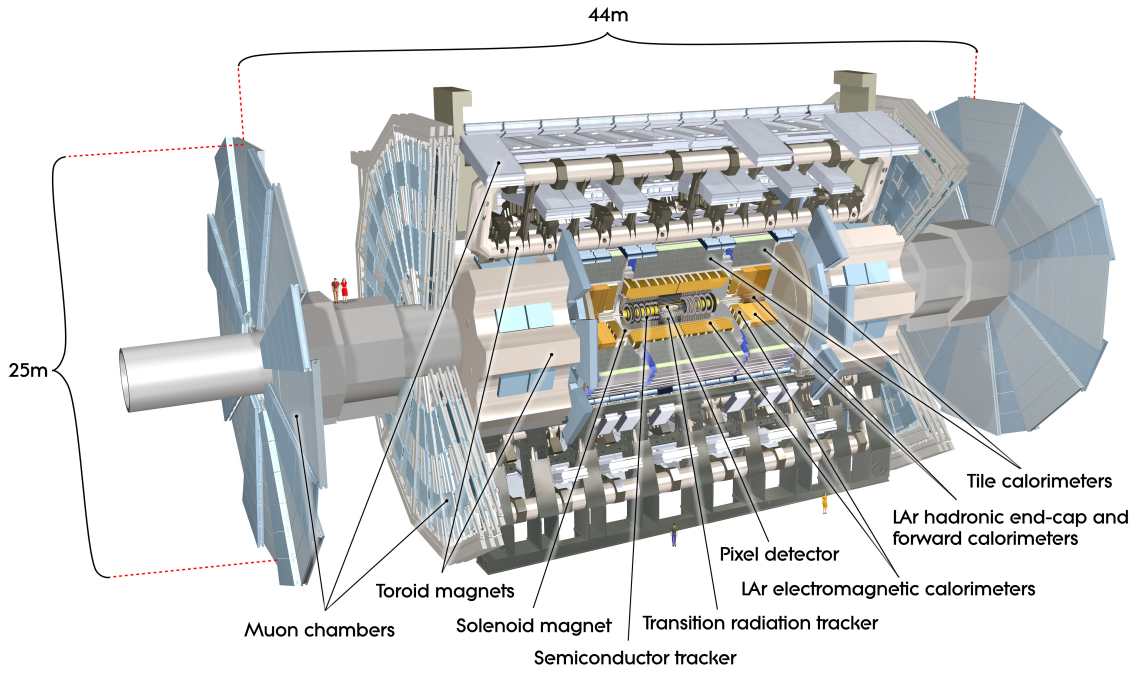

Figure 4.3.: Overview of the ATLAS detector [36]

4.2.1. The ATLAS Coordinate System

The barrel-shape detector geometry, mainly dictated by the traversing beam-pipe which marks the symmetry axis, implies the introduction of a specially adapted polar coordinate system that is used when it comes to defining measureable quantities such as particle momenta and reconstructing physics objects (see Section 5):

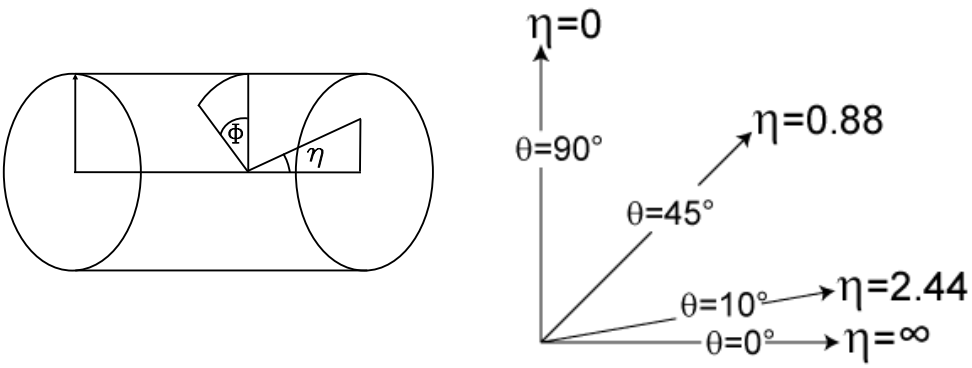

(a) (b)

Figure 4.4.: The ATLAS coordinate system: (a) modified polar coordinates (η, ϕ) and (b) pseudorapidity η [38]

The collision point of the two proton beams marks the origin of the coordinate system and the z-axis is defined to be in the direction of the beam axis. The x-axis points inwards towards the centre of the LHC ring and the y-axis is perpendicular to the surface, pointing upwards. The azimutal angle ϕ and the polar angle θ are defined, as usual, as the angle in the x-y plane and the angle from the beam axis, respectively (see Figure 4.4 (a)). However, the angle θ is commonly

replaced by the so-called **pseudorapidity** η:

$$\eta = -\ln[\tan\left(\frac{\theta}{2}\right)] \tag{4.2}$$

The introduction of this quantity is motivated by the fact that for massless particles[11] the pseudorapidity equals the Lorentz invariant quantity **rapidity** y which in high-energy physics is defined as

$$y = \frac{1}{2}\ln\left(\frac{E+p_z}{E-p_z}\right) \tag{4.3}$$

where E stands for the total energy and p_z for the z-component of the particle momentum.
Figure 4.4 (b) illustrates some values of the pseudorapidity: η is zero in the direction perpendicular to the z-axis, has small values in the central region and diverges rapidly in the proximity of the beam axis. Hard-scattering processes of interest tend to result in particles with high transverse momentum and, therefore, low $|\eta|$ whereas unwanted background effects, for example from the beam remnant, dominate in the high-$|\eta|$ which is therefore often excluded from the analysis. The replacement of the angle θ by the pseudorapidity η takes these facts into account by providing a high resolution of the central detector region. A further advantage is the invariance of the difference $\Delta\eta = \eta_1 - \eta_2$ under Lorentz boosts along the z-axis.

Distances between two particles i and j in the detector coordinate system are measured using the distance parameter

$$\Delta R_{i,j} = \sqrt{(\eta_i - \eta_j)^2 + (\phi_i - \phi_j)^2)} \tag{4.4}$$

The momentum $\vec{p}$ of a particle in this coordinate system is generally characterised by its component perpendicular to the beam axis, $p_\perp = (p_x, p_y, 0) = \sin(\theta)\cdot\vec{p}$ and the angles η and ϕ instead of its cartesian components (p_x, p_y, p_z). The preference of the transverse values of energies or momenta over the respective total values is due to the fact that in a hadron collider the exact values of the momenta of the initial-state partons in the direction of the beam axis are unknown since each parton carries only a fraction x of the total proton momentum. The exact value of x cannot be predicted for a particular event, only its probability can be given in the form the PDFs of the respective hadron. While the total event dynamics in the z-direction is underconstrained due to insufficient knowledge about the exact initial-state kinematics in the z-direction, it can be assumed that the transverse momenta of the initial-state partons and therefore those of the final-state particles add up to zero which means that the dynamics in the transverse plane is well-determined.

The ATLAS detector consists of various layers of sensitive material each of which is forward-backward symmetric and can be divided into a cylindrical *barrel* and a wheel-shaped *end-cap region*. Each layer is specially designed for the measurement of a different set of quantities. The combination of the measurements from all the individual components yields the *detector signature* for a particular event which - somewhat similar to a finger-print - allows the reconstruction and identification of this unique event.
In the following, the different detector layers shall be introduced briefly. The technical details and numerical values can be found in [35] and [39].

[11] This approximation applies to most particles produced at the LHC because due to the high centre-of-mass energy their kinetic energy by far exceeds their rest energy/mass. Notable exceptions are the top quark and - for many purposes - also the bottom quark.

4.2.2. The Inner Detector

The inner detector (Figure 4.5) has a length of 7 m and a radius of 1.15 m. It is contained within a solenoidal magnetic field of 2 T which bends the tracks of charged particles thus allowing the determination of the particle momentum from the curvature of its track in the magnetic field. The inner detector consists of three sub-components: The **Silicon Pixel Detector**, closest to the interaction point, and the surrounding **Semiconductor Tracker (SCT)** allow the determination of charged particle tracks with high resolution due to their fine granularity. They are mainly used for momentum measurement and the reconstruction of primary and secondary vertices, the precise determination of which is important in order to distinguish between multiple interactions that can occur within the same bunch-crossing or to tag b-quark jets (see also Section 5.6). The outermost part of the inner detector, the **Transition Radiation Tracker (TRT)** consists of (mainly Xenon-filled) straw-tubes. It provides additional tracking information and can, for example, be used to distinguish between electrons and pions.

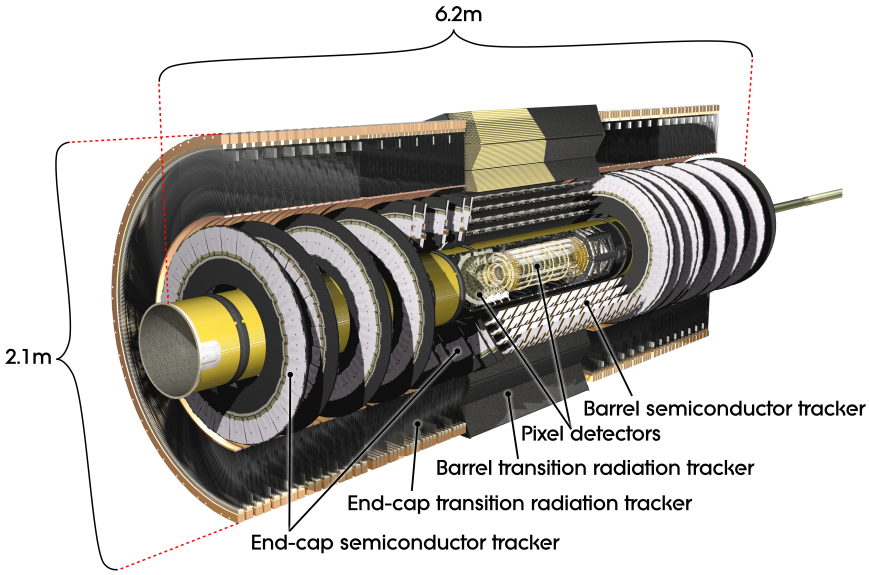

Figure 4.5.: The Inner Detector [36]

4.2.3. The Electromagnetic and Hadronic Calorimeter

The purpose of the Calorimeter System (Figure 4.6) is the determination of the energy of electrons, positrons and photons (Electromagnetic Calorimeter) and that of hadronic particles (Hadronic Calorimeter). An incident particle triggers a shower of secondary particles either via the emission of bremsstrahlung and electron-positron pair production and annihilation in the case of electrons, positrons and photons, or via inelastic scattering with the nuclei of the calorimeter material which leads to the creation of other hadronic particles, predominantly pions. While the charged pions $\pi^{\pm}$ can trigger further hadronic cascades, the neutral pions π^0 almost immediately decay into two photons that can give rise to electromagnetic sub-showers within the hadronic shower. These decays are problematic because they can lead to the mis-identification of a hadronic jet as an electromagnetic one, a so-called “fake electron” (see Section 6.1.5).

Apart from providing a way to measure the energy of the incident particle, the direction and profile of the shower in the calorimeter provide additional information about the momentum and the identity of the particle that triggered the jet.

In order to absorb all particles within the calorimeter, despite their high energies resulting from the high centre-of-mass energy of the collision, purely absorbing layers of material have been introduced between the sensitive ones that are used for the actual energy measurement: The Electromagnetic Calorimeter combines sensitive layers of liquid argon (LAr) with lead absorbers both in the barrel and the end-cap region while the Hadronic Calorimeter uses scintillator plates and iron absorbers in the central and a combination of liquid-argon layers and copper plates in the end-cap region.

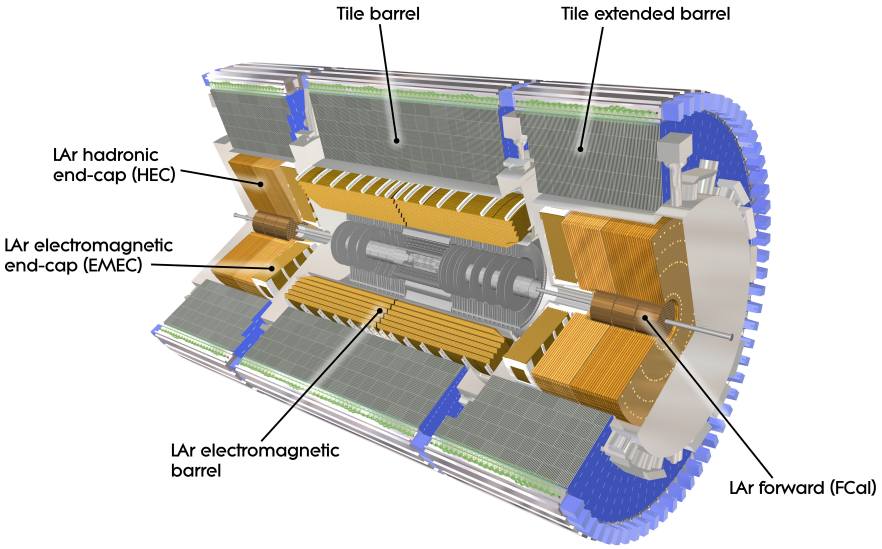

Figure 4.6.: The Calorimeter System [36]

The Calorimeter system has an outer radius of 4.25 m and a length of 12.20 m. It is designed to absorb all particles except for muons and neutrinos. While the latter leave the detector undetected, the muon properties are measured in the outermost component of the ATLAS detector.

4.2.4. The Muon Spectrometer

The Muon Spectrometer (Figure 4.7) has been designed to allow for stand-alone muon reconstruction (see Section 5.3). It consists of three layers of **Monitored Drift Tube (MDT) Chambers** combined with **Cathode Strip Chambers (CSCs)** at large pseudorapidities. The MDT chambers are made up of aluminium tubes with a central W-Re wire and filled with a mixture of 93 % argon and 7 % CO_2. They are arranged within a magnetic field of three air-core toroids in the barrel region and allow for a precise stand-alone reconstruction of the muon momenta (see Section 5.3 for details).

In addition, **Resistive Plate Chambers (RPCs)** and **Thin Gap Chambers (TGCs)**, installed in the barrel and end-cap region, respectively, provide fast hardware-based trigger systems with high time-resolution that are, for example, used to identify and distinguish between bunch-crossings.

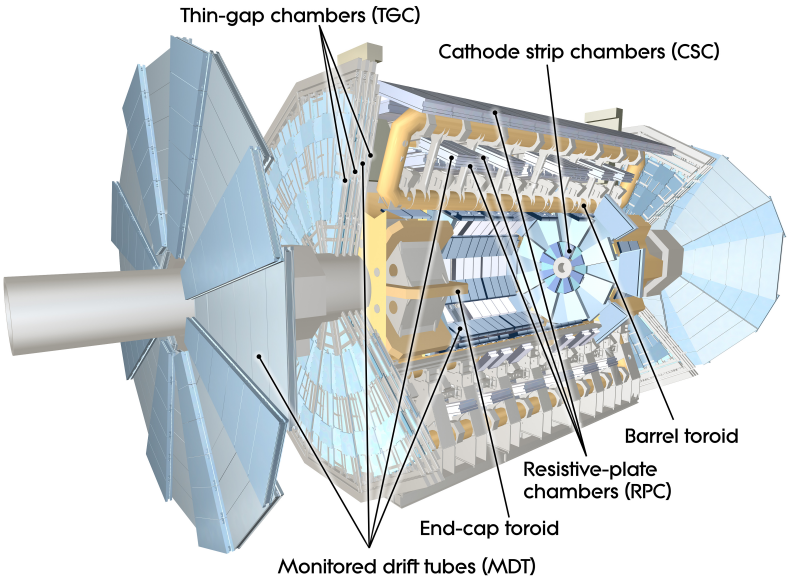

Figure 4.7.: The Muon Spectrometer [36]

4.2.5. The Trigger System

The wealth of information that is generated by the various detector components for each event, together with the high collision rates at the LHC, make it impossible to even temporarily store the information about each event. For the current bunch-spacing of 50 ns, there are 20 million bunch crossings per second. The average number of interactions per bunch crossing for the 2011 data-taking periods varies between 10 and 30 (for details consult [40]). Assuming 20 interactions per bunch crossing on average, this makes 400 million interactions per second. Once the bunch-spacing is decreased to its nominal value of 25 ns, the bunch-crossing rate will double to 40 MHz.
Only a small fraction of the events measured in the detector are of interest to physics analyses and deserve to be stored permanently. To pick out these events and thereby reduce the flood of data produced by the detector, a multi-level trigger system has been installed (Figure 4.8; for further details consult [39]):

The Level-1 (L1) Trigger: The first stage of the trigger system, the L1 trigger, is entirely hardware-based. It searches for high transverse-momentum muons, using the aforementioned RPCs and TGCs in the Muon Spectrometer, as well as high transverse-momentum electrons and jets and large missing transverse energy using reduced-granularity information from all calorimeter components. Based on this information, so-called *Regions-of-Interest* (RoIs) around interesting objects like the ones mentioned above are defined. The processing time per event at this stage is around 2.5 μs and the event rate is reduced to around 75 kHz. The selected events are stored in the *Read-Out-Drivers* (RODs) until the trigger decision is made at the next stage.

The Level-2 (L2) Trigger: At the next trigger stage, the software-based L2 trigger, all available detector information about the RoI defined by the L1 trigger is evaluated, making use of the full detector granularity and precision. The L2 selection reduces the event rate to approximately 3.5 kHz with an average processing time per event of roughly 40 ms.

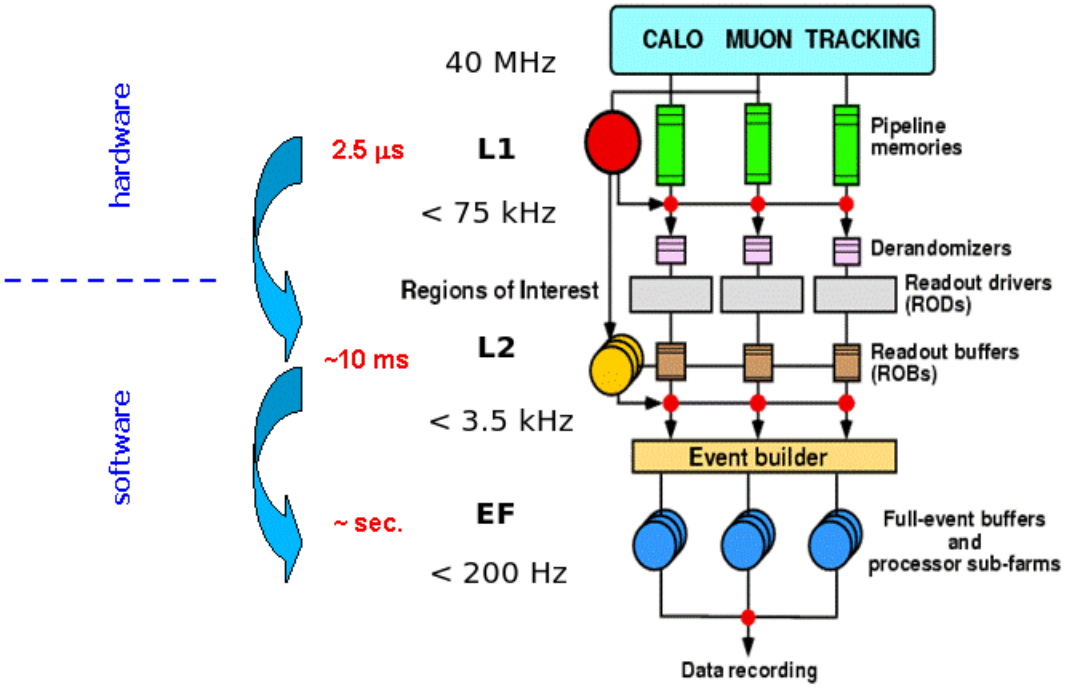

Figure 4.8.: The Trigger System (based on [35])

The Event Filter (EF): The final stage of the trigger chain is the Event Filter (EF). This event-selection process is based on a preliminary reconstruction of physics objects such as muons or jets with an average selection time per event of around 4 seconds. The EF reduces the event rate to roughly 200 Hz. The events that pass this final selection stage are written to permanent storage.

4.3. The Worldwide LHC Computing Grid (WLCG)

Despite the trigger system, the ATLAS as well as the other experiments produce huge amounts of raw data that need to be stored and processed. Moreover, extensive Monte Carlo simulations of physics processes and detector components are necessary to complement, cross-check and interpret the real-data output. To provide these services to an international community of particle physicists working at different institutes on serveral continents, the **W**orldwide **L**HC **C**omputing **G**rid (WLCG) has been developed. This computing network is formed by interconnected computing centres in different countries (the "nodes" of the network) that share their storage and processing resources and are hierarchically organised into different levels, called **Tiers** (see Figure 4.9 (a)): The CERN Computing Center (see image in Figure 4.9 (b)) forms the **Tier-0**. A copy of all raw datasets is kept there for storage and reconstruction. Backup copies are held at eleven major computing centres around the world that form the **Tier-1**. The German Tier-1 centre is the GridKa at the Karlsruhe Institute of Technology (KIT). The **Tier-2** sites, which are typically located at larger universities and research institutes, are allocated further copies of selected datasets by the Tier-1 sites and participate in event reconstruction and further analysis tasks as well as the production of Monte Carlo samples.

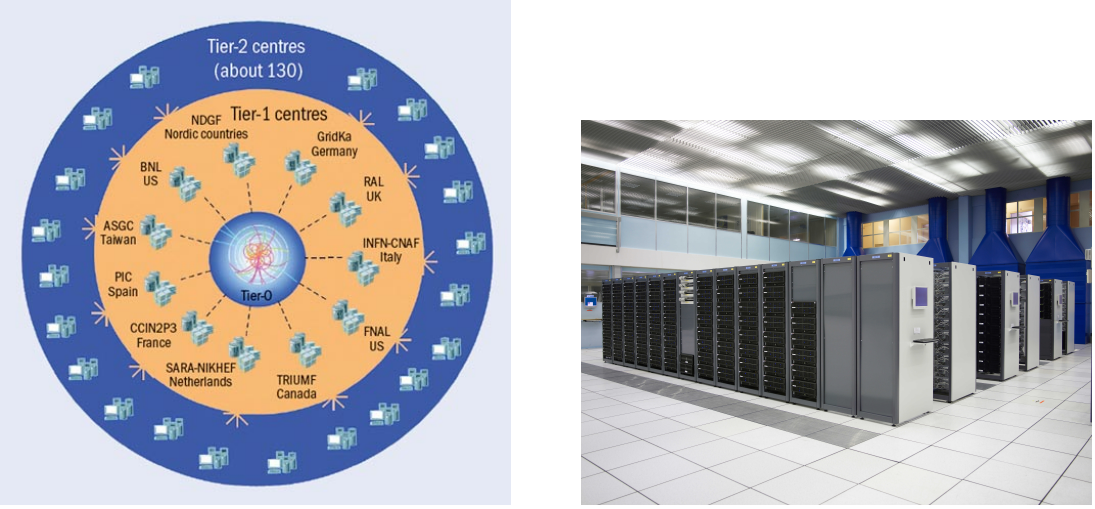

(a) **(b)**

Figure 4.9.: (a) Schematic overview of the WLCH [41] and (b) a view of the CERN Computing Center during the installation of the processors [36]

Analysis and simulation jobs by individual researchers are processed directly at one or several of the computing sites that are chosen by a brokerage system on the basis of various criteria such as the availability of the requested dataset and the current workload at a particular site thus making the transfer of huge datasets to local computers obsolete and allowing fast parallel processing of computing jobs.

5. Definition of Physics Objects

A single event such as the production and decay of a pair of top and anti-top quark gives rise to a unique and complex detector signature. The signals from the various detector components (see Section 4.2) need to be combined in order to reconstruct and identify the final-state particles. Only then is it possible to distinguish and select the events of interest to a particular analysis (see Section 6 on **Event Selection**) and to reconstruct the complete physics process including the four-momenta and masses of the final-state particles such as the top quark (see Section 8 on **Event Reconstruction**).
This section deals with the first step in the reconstruction chain, the **Reconstruction of Physics Objects**.

5.1. General Event Topology

In order to correctly reconstruct the physics objects in a particular event, one needs to take into account the complex event topology in high-luminosity hadron colliders such as the LHC:

The **hard-scattering processes**[1] that are of interest to most physics analyses generally cannot be observed isolated but are superimposed by a number of (usually) softer processes which are commonly summarised under the term **Underlying Event (UE)**[2]. These processes may either be related to the so-called *Beam-Remnant (BR)*, which consists of all partons that do not actively take part in the hard interaction but are colour-connected with the partons that do,[3] or they arise from additional interactions between other partons from the same pair of protons (*Multiple Parton Interactions (MPI)*). Both contributions are a direct result of the complex composite nature of the proton.

Moreover, additional elastic, diffractive or hard interactions between other protons of the *same bunch* may occur during a single bunch-crossing. These processes are commonly denoted as **in-time pile-up**. Finally, the signatures of interactions from *subsequent bunch-crossings* may overlap in the detector due to the limited read-out time of the detector electronics. This is known as **out-of-time pile-up**. Pile-up is directly related to the high luminosity of the LHC and its contribution is expected to increase with the luminosity, for example when the bunch-spacing is reduced from the current 50 ns to 25 ns.

These additional interactions complicate the identification of the hard-scattering process as well as, for example, the measurement of electron and jet energies because they lead to additional energy deposits in the calorimeter system that need to be taken into account during reconstruction.

[1] These are processes in which the colliding partons exchange a large four-momentum.
[2] It should be noted that in this analysis initial- and final-state radiation are not considered as part of the UE.
[3] This is another consequence of confinement (see Section 2.1.2): While the proton as a whole does not carry any colour, the constituent partons that participate in the hard-scattering do. Due to colour-charge conservation, the overall system remains colourless and confinement dictates that the scattered partons remain colour-connected with the remaining partons. For illustration see also the remarks on colour flux in the context of the string model introduced in Section 2.1.2.

5.2. Electrons

Electrons are reconstructed using the information from the Inner Detector (ID) and the Electromagnetic Calorimeter (EC): They deposit all their energy in the EC through the formation of electromagnetic showers and, due to their electric charge, leave a curved track in the magnetic field of the ID which helps to distinguish them from photons which also give rise to electromagnetic showers in the EC but have no associated track in the ID (see for example Figure 5.1).

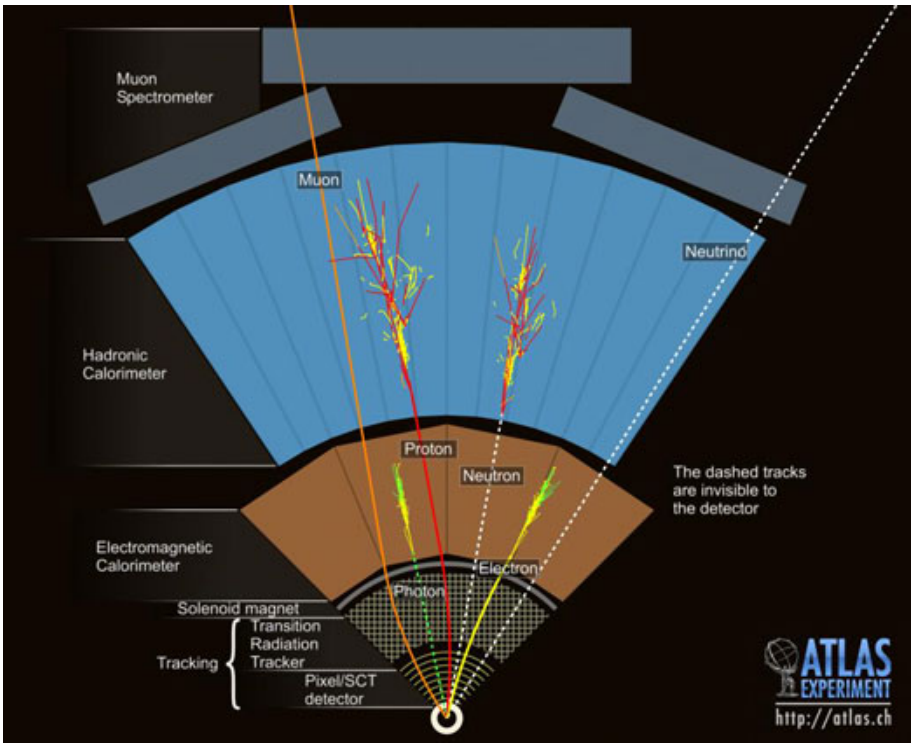

Figure 5.1.: Overview of the detector signatures of different particles [42]

In order to distinguish signal electrons (i.e. electrons from the primary decay) from background electrons that may arise through secondary processes such as photon conversion or Dalitz decays and from jets that may fake an electron-like signature, a number of quality requirements is imposed on the electron candidates. Depending on the choice of these quality cuts, the reconstructed electrons fall into three categories:

- **Loose**: Only shower-shape variables from the EC as well as information about a possible leakage of the shower into the Hadronic Calorimeter (HC) is used for the reconstruction.

- **Medium**: In addition to the requirements for loose electrons, an ID track matching the electromagnetic cluster in the EC is required. Both the ID track and the EC shower have to fulfil a set of additional quality criteria.

- **Tight**: Electrons in this category have to fulfil all the requirements for medium electrons but tighter quality criteria are imposed on the ID tracks and EC clusters as well as on the track-cluster matching and information from additional detector components such as the TRT is used to further improve the background rejection rate.

Tighter quality requirements result in a better rejection rate for background electrons but also a correspondingly lower selection efficiency for signal electrons. For further details on electron reconstruction see [43].

The choice of the reconstruction algorithms and the quality criteria as well as the application of additional quality cuts on the reconstructed objects depends heavily on the aims and requirements of the particular physics analysis and therefore differs between the various analysis groups at ATLAS.

The object definitions for electrons developed by the Top Working Group for Athena Release 16.6.5 and used throughout this analysis shall be outlined in the following. For further details see either Appendix 5.2 or the official Top Group Twiki page [44].

- Electron candidates must fulfil the quality requirements of the **tight** category.
- The reconstruction algorithm **starts from seeds of calorimeter cells** to form calorimeter clusters.[4]
- Electron candidates must have a **transverse energy** $E_{\perp} > 25$ GeV and a **pseudorapidity** $|\eta_{EC\_Cluster}| < 2.47$, excluding the crack region[5] $1.37 < |\eta_{EC\_Cluster}| < 1.52$. These cuts ensure that only electron candidates from detector regions with a sufficiently high resolution are used, thus allowing precision measurements of energies and momenta.
- To reject electrons that arise from weak decays inside hadronic jets (in particular b-jets), electrons are required to be **isolated**: The total energy deposit in the calorimeter cells within a cone of radius $\Delta R < 0.20$ around the electron candidate must be less than 3.5 GeV (exluding the energy deposit from the electron itself). Moreover, if there are one or more jets within the cone of radius $\Delta R < 0.20$ around an accepted electron, i.e. an electron that fulfils all quality criteria, the jet closest to the electron is removed (electron-jet overlap removal).
- Additional **object-quality cuts** are applied to exclude regions with dead or damaged detector material.

5.3. Muons

Muons interact considerably less with the detector material than electrons - a consequence of their 200 times greater mass. This means that they pass the ID and Calorimeter System almost unhampered and can therefore be detected in the outermost layer of the ATLAS detector, the Muon Spectrometer (MS). The MS has been designed to allow for stand-alone muon reconstruction but the use of additional information from the other detector parts generally leads to a better muon identification efficiency. Reconstructed muons can therefore be grouped into three categories:

- **Stand-Alone Muons**: Only information from the MS is used for the reconstruction. The tracks are reconstructed using either the Muonboy or Moore algorithm and are then extrapolated to the beam line.
- **Combined Muons**: Stand-alone muons found in the MS are matched to ID tracks using either the Staco or the MuID algorithm. The muon properties are then evaluated combining the information from both detector components.
- **Tagged Muons**: The reconstruction starts from suitable ID tracks which are extrapolated to the MS. The algorithms MuTag or MuGirl are then applied to search for hits in nearby MS segments.

[4] Alternative reconstruction algorithms may start with ID tracks.
[5] The crack region is the transition region between the barrel and end-cap part of the detector.

For further information on muon reconstruction see, for example, [45].

As in the case of electrons, analysis-specific quality cuts are then applied to the muon candidates to reject background muons such as muons arising from weak decays inside jets. The guidelines developed by the Top Working Group and used throughout this analysis are outlined in the following:

- Muons are reconstructed as **combined** muons using the **MuID algorithm**.
- Muon candidates are required to have a **transverse momentum** $p_\perp > 20$ GeV and lie within the **central detector region** ($|\eta_{EC\_Cluster}| < 2.5$) where the momentum resolution is highest.
- Further quality criteria are applied to the ID tracks. For details see Appendix 5.3.
- Muon candidates must fulfil a number of **isolation criteria**, similar to those for electrons. Additionally, a **muon-jet overlap removal** is performed by removing muon candidates for which there is a jet with $p_\perp > 20$ GeV within $\Delta R < 0.4$ (before jet-electron overlap-removal). This procedure aims at rejecting secondary muons that may result from weak decays inside hadronic jets.

5.4. Jets

While electrons and muons may give rise to cascades of secondary particles when they interact with the detector material and their reconstruction from the raw data is everything but trivial, the interpretation of their detector signatures is facilitated by the fact that they are long-lived elementary particles that can in principle be observed freely. Thus the reconstructed electron and muon objects can be much more readily related to the elementary electrons and muons in the final state of a hard-scattering process.
The reconstruction of coloured final-state particles such as quarks and gluons is more complicated because they are subject to confinement: As explained in Section 2.1.2, these particles trigger **parton showers** via gluon radiation or gluons splitting into pairs of quarks and anti-quarks which then form colourless bound-states, the hadrons. It is only these **hadron showers** that are observed in the detector: Charged hadrons like protons or $\pi^\pm$ leave **tracks** in the ID while neutral hadrons pass this detector layer unseen. Finally, all hadrons are absorbed within the Hadronic Calorimeter, depositing all their energy in **clusters** of calorimeter cells. The different stages of this process are illustrated in Figure 5.2.

In order to reconstruct the four-momentum of the original parton and, if possible, identify its flavour, the constituents of these hadronic showers or **jets** have to be identified. For this purpose, various **jet algorithms** have been developed, an overview of which shall be given in the following sections.

5.4.1. Jet Constituents

Jets can be reconstructed at different stages of their evolution process. Depending on the objects used as input to the jet algorithm, different classes of jets can be defined: At detector level, there can be either **track jets**, reconstructed from the tracks of charged particles in the ID, or **calorimeter jets**, formed by groups of calorimeter cells. The latter fall into two categories: **Tower jets** are formed by radial towers of calorimeter cells with a standard area of $\Delta\eta \times \Delta\phi = 0.1 \times 0.1$ in the $\eta - \phi$ -plane. **Topological jets**, which are used for this analysis, are built from topological clusters

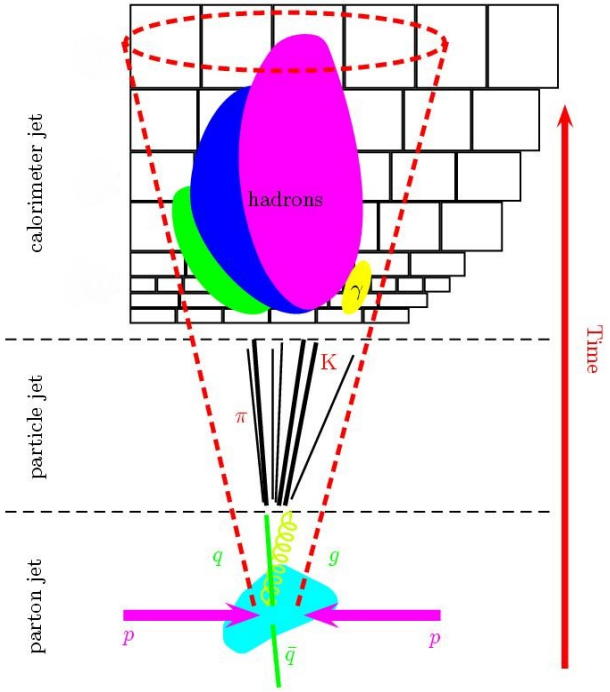

Figure 5.2.: The evolution of hadronic jets from final-state partons (adapted from [26])

of calorimeter cells that are constructed by a clustering algorithm starting from a seed cell with a signal-to-noise ratio above a certain threshold. A more detailed description of clustering algorithms and calorimeter jets in general can be found in [46].
At Monte-Carlo level, so called **truth jets** are formed from stable particles[6] exluding muons and neutrinos. These can be compared to jets at detector level in order to study the influence of detector effects on the reconstruction of jets.

5.4.2. Recombination Schemes

For each jet algorithm, a recombination scheme has to be chosen that defines in which way the four-momenta of the constituent particles are to be combined to yield the four-momentum of the jet. In the simplest recombination scheme, often denoted as the **E-scheme**, the jet four-momentum is given by the sum of the four-momenta of its constituents. This scheme is used throughout this analysis. For alternative recombination schemes consult [46].
One particularly important feature of the E-scheme is that jets aquire a mass even though their constituents may be massless. To illustrate this, consider the case of two massless particles with four-momenta p_1 and p_2 that are to be combined to form a (proto-) jet using the E-scheme. Since $p_{1,2}^2 = m_{1,2}^2 = 0$, the invariant mass M of the proto jet is given by

$$M^2 = (p_1 + p_2)^2 = m_1^2 + m_2^2 + 2 \cdot (E_1 \cdot E_2 - \vec{p}_1 \cdot \vec{p}_2) = 2 \cdot E_1 \cdot E_2 \cdot [1 - \cos(\alpha_{12})] \tag{5.1}$$

where α_{12} denotes the angle between the three-momenta of the two particles. Non-zero angles between the jet constituents therefore result in a non-zero mass M despite the fact that the jet constituents themselves as well as the original parton are (approximately) massless.

[6] "Stable" in this context refers to all particles with a lifetime $\tau > 10$ps.

The invariant mass distribution for the selected jets in the non-allhadronic $t\bar{t}$ sample[7] is shown in Figure 5.3. Jet masses in the E-scheme typically range between 5 and 10 GeV.

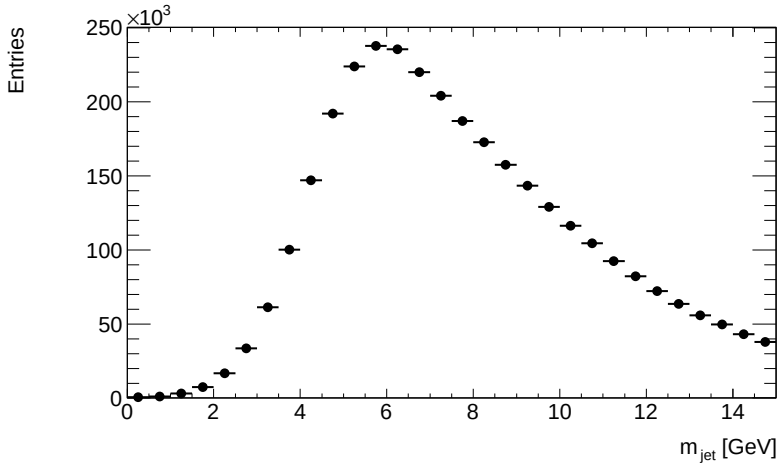

Figure 5.3.: Invariant mass distribution of the selected jets in the non-allhadronic $t\bar{t}$ sample

5.4.3. Jet Algorithms

There are various ways to build jets from a given set of input particles using a particular recombination scheme. The shape and multiplicity of the jets found in the same event may differ significantly between the different jet algorithms. Although it is tempting to think of a jet as a well-defined, more or less collimated bundle of particles with a common origin that reflects the properties of the orginal final-state parton, it is important to always keep this model dependence in mind when talking about jets as physical objects. Therefore, the jet algorithms and their parameters have to be chosen with care and should fulfil a few general requirements:

Infrared Safety: The presence or absence of soft gluons between jets should not alter the jet multiplicity of the event by causing the two jets to be combined into one as shown in Figure 5.4.

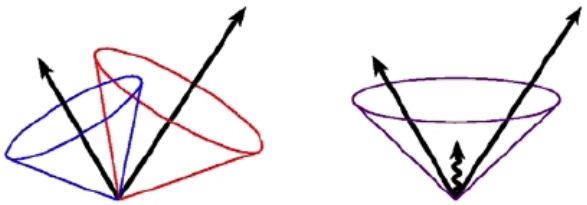

Figure 5.4.: The recombination of two jets into one in the presence of a soft gluon [38]

Collinear Safety: The splitting of a constituent particle into two highly-energetic, almost collinear particles should not lead to the splitting of the jet into two which would lead to a wrong jet multiplicity in the event.

[7]For details on this sample and the event-selection process see Section 6.

Order Independence: The result of the jet formation should be the same at different stages of the jet evolution, i.e. at parton, hadron and detector level.

Ideally, there should be no significant dependence on the Underlying Event or pile-up conditions or - when applied to simulated events - on the hadronisation model used by the respective Monte Carlo generator.

Out of the variety of jet algorithms used in physics analyses at ATLAS - an overview of which can be found in [47] - only the k_T and the anti-k_T algorithm shall be introduced here in detail. Both algorithms proceed in a similar way to reconstruct jets from a given set of input particles[8]:

Clustering procedure

1. For all pairs of input particles (i, j) the distance parameter

$$d_{i,j} = \min(k_{T,i}^{2p},\ k_{T,j}^{2p}) \frac{(\Delta R)_{i,j}^2}{R^2}$$

   is calculated where $k_{T,i}$ denotes the transverse momentum of the i^{th} particle and

$$(\Delta R)_{i,j}^2 = (y_i - y_j)^2 + (\phi_i - \phi_j)^2.$$

   is a measure of the geometric distance in the coordinate system of the detector.[9] Moreover, for each particle i the distance parameter

$$d_{i,B} = k_{T,i}^{2p}$$

   with respect to the beam axis is evaluated. The parameters p and R characterise the jet algorithm as explained below.

2. The smallest distance parameter is chosen among the $d_{i,j}$ and $d_{i,B}$. If it is one of the $d_{i,j}$, the respective particles are combined into a new object according to the chosen recombination scheme. If the smallest distance parameter is one of the $d_{i,B}$, the object i is considered a finished jet and removed from the list of objects.

3. The procedure is iterated with the updated list of particles until either all the particles have been absorbed into jets or all the distance parameters have values larger than some predefined cut value d_{cut}.

The anti-k_T algorithm

The anti-k_T algorithm, defined by the condition $p = -1$, is currently the standard algorithm for jet reconstruction at ATLAS. The parameter R that determines the jet size can be chosen to fit the needs of a specific analysis task. Common values are $R = 0.6$ or $R = 0.4$ which is the value chosen by the Top Working Group and applied in this analysis. The negative value of p implies that the algorithm clusters nearby particles with high transverse momentum first. The algorithm stops when all particles have been absorbed into jets.

[8] The term "particle" in this context applies to all objects that can be used as an input to a jet algorithm, such as partons, hadrons or calorimeter cells.

[9] Note that here the *rapidity* y is used in the calculation of the distance parameter instead of the *pseudorapidity* η used in Equation (4.4). For massless particles, however, there is no difference between the two definitions.

The k_T algorithm

The case $p = 1$ corresponds to the **inclusive** k_T algorithm: The $d_{i,j}$ are smallest for nearby low-p_T particles which are therefore clustered first. Hence the k_T algorithm can be said to reverse the QCD showering process which is ordered in Q^2, starting from hard (large-Q^2) parton emissions at large angles and evolving towards soft (small-Q^2) emissions at smaller angles. For more information on momentum and angular ordering in parton shower evolution see, for example, [48] and [49].
The k_T algorithm can also be used in the **exlusive** mode which differs from the inclusive one in two aspects: Firstly, when a $d_{i,B}$ is found to be the smallest distance parameter, the corresponding particle is not declared to be an individual jet but considered a part of the beam remnant and removed from the list. Secondly, an additional cut-off parameter d_{cut} is introduced: The clustering process is terminated if at some point all the $d_{i,j}$ and $d_{i,B}$ are larger than d_{cut} and all remaining particles are declared as jets. For small values of d_{cut} more jets are reconstructed than for large values. This allows to probe the substructure of jets by varying the value of d_{cut}.
In both the inclusive and the exclusive mode R is commonly set to 1.

Comparison of different algorithms and clustering parameters

Figure 5.5 shows how the choice of jet algorithms and their respective parameters influences the number and shape of the reconstructed jets: The four sub-plots show the p_T distribution in the $\eta - \phi$ plane for the stable final-state particles[10] of the same semileptonic $t\bar{t}$ event which has been generated with MC@NLO interfaced with Herwig+Jimmy for the simulation of the hadronisation and the Underlying Event. The detector simulation has not been applied at this stage, hence all reconstructed jets are truth jets. The FastJet [50] software, which provides an implementation of various jet algorithms, has been used for the jet reconstruction. Jets are coloured in the order of descending p_T as red, green, blue, yellow, magenta, etc. and particles not associated to any jet are shown in grey.

The upper two plots show the jets reconstructed with the k_T algorithm in the exclusive mode with $R = 1$. The d_{cut} parameter is 400.0 GeV^2 in the left plot and 300 GeV^2 in the right plot. In the latter case, five jets are reconstructed with two distinct but close-by high-p_T jets at $\eta \approx 2$ (red and yellow jets in the upper right plot). In the case of the higher d_{cut} value where the clustering is terminated at a later stage, these two jets have been merged into one (red jet), thus reducing the jet multiplicity in the event to four.
The two lower plots show the jet topology of the same event, this time reconstructed with the anti-k_T algorithm with a value of $R = 0.4$ (left plot) and $R = 0.6$ (right plot), respectively. In the latter case, a single high-p_T jet (red) is reconstructed from the particles at $\eta \approx 2$ while the cluster is resolved into two jets for $R = 0.4$.
These examples illustrate how much the jet shape and multiplicity of an event and therefore the outcome of the entire analysis depend on the choice of the jet algorithm and its parameters. In this context, Monte Carlo studies are essential because the truth information about the original hard-scattering process can be used to evaluate how far the properties of the reconstructed jets reflect the dynamics at parton level.

5.4.4. The Jet Energy Scale (JES)

The calorimeter jets that are used in most physics analyses, including the one presented in this thesis, are reconstructed by the chosen jet algorithm from energy depositions in the calorimeter

[10] Muons and neutrinos are not considered here in accordance with the conventions for truth jets.

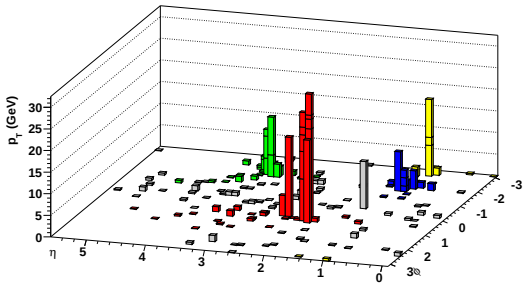

(a) k_T algorithm: d_{cut} = 400.0 GeV

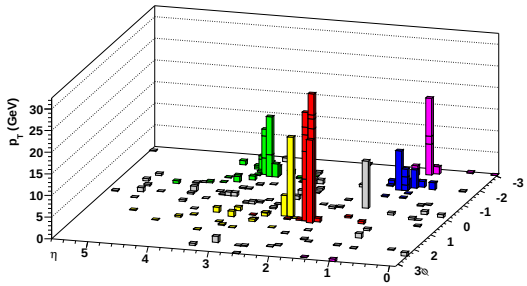

(b) k_T algorithm: d_{cut} = 300.0 GeV

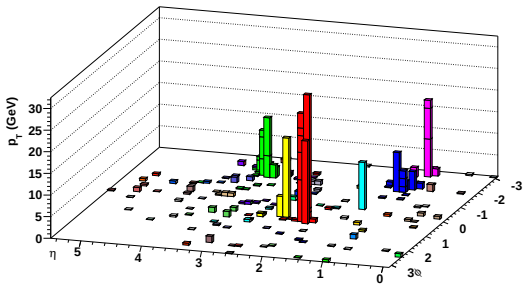

(c) anti-k_T algorithm: R = 0.4

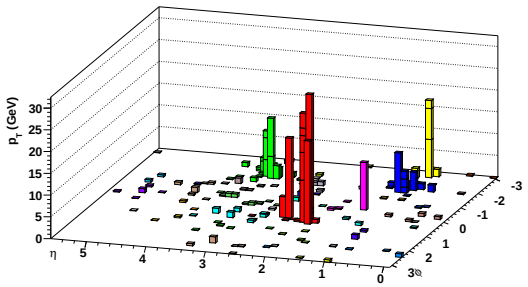

(d) anti-k_T algorithm: R = 0.6

Figure 5.5.: Comparison of jet topology for the same event reconstructed with different jet algorithms using FastJet

systems. These energies, however, cannot be related directly to the energy of the original parton but need to be corrected for various systematic effects:

- The calorimeter system has been calibrated to the so-called **Electromagnetic (EM) Energy Scale** which is established via test-beam and cosmic-ray measurements. For details on the calibration see [46]. It accounts correctly for energy depositions from electrons and photons but underestimates the energy deposited by hadronic showers.

- Energy losses may occur in regions with dead or damaged detector material or when highly-energetic particles are not fully absorbed in the calorimeter system (leakage).

- Moreover, it can happen that not all energy deposits in the calorimeter stemming from the same hadronic shower are also included in the corresponding calorimeter jet by the reconstruction algorithm.

- Multiple proton-proton interactions within the same bunch crossing (in-time pile-up) may lead to additional energy deposits in the jet area and thus to an overestimation of the jet energy while multiple interactions from a preceeding bunch-crossing (out-of-time pile-up) have the opposite effect.

To compensate for these and other effects and to retrieve the **Jet-Energy Scale (JES)** at which the energy of the jet is supposed to reflect that of the original parton, corrections must be applied to the energy of each reconstructed jet. This is done using Monte Carlo simulations in which the truth jet corresponding to a particular calorimeter jet can be retrieved and an energy-scale correction factor can be derived from the comparison of the truth-jet energy and that of the calorimeter jet. Various jet-energy calibration schemes exist (for details see [46]), among which the simplest is the so-called **EM+JES scheme** which is the calibration scheme currently recommended by the Top Working Group. In this scheme two types of corrections are applied to jets reconstructed at the **EM** scale:

1. **Vertex correction**: The four-momentum of the jet which has been reconstructed with respect to the origin of the detector coordinate system is corrected so that the jet now originates from the primary vertex of the event.

2. **JES calibration (including pile-up effects)**: For each pair of matched truth and calorimeter jets a response function $\mathcal{R}^{jet}_{EM}(\eta_{det}, E^{jet}_{EM}) = \frac{E^{jet}_{EM}}{E^{jet}_{truth}}$ is derived where E^{jet}_{EM} denotes the jet energy at the EM scale after the application of the aforementioned corrections. The Monte-Carlo samples in this context include a simulation of pile-up effects.[11] From this response function energy- and pseudorapidity-dependent correction factors $\mathcal{F}(E^{jet}_{EM})|_{\eta_{det}}$ are calculated which are then used to determine the energy of each jet at the **EM+JES scale**:

$$E^{jet}_{EM+JES} = \frac{E^{jet}_{EM}}{\mathcal{F}(E^{jet}_{EM})|_{\eta_{det}}}. \tag{5.2}$$

The determination of the jet-energy scale is a challening task due to the multitude of effects that have to be taken into account and that contribute to the overall **JES uncertainty**, which - like the JES calibration factor itself - is a function of the transverse energy and the pseudorapidity of the respective jet. Among the contributions to the JES uncertainty are uncertainties related to the Monte-Carlo model that is used to derive the JES correction factors, for example on the modelling of the parton shower or the underlying event. Further effects that influence the measured energy of a jet such as the pile-up conditions or the presence of close-by jets have to be taken into account as well. For details on the determination of the JES uncertainty consult [46]. The current[12] official values of the maximum fractional JES uncertainty for the anti-k_T algorithm with $R = 0.4$ in the EM+JES calibration scheme are summarised in Table 5.1. It is expected that these uncertainties will be reduced as more data are taken and a better understanding of detector effects will be achieved over time. Currently, in-situ measurements are being performed with the aim of determining the jet-energy scale at a greater accuracy: These measurements use, for example, the momentum balance in two-body decays with a single quark and a photon in the final-state in order to determine the momentum of the quark-induced hadronic jet from that of the photon as measured with the electromagnetic calorimeter.

At this point, it is also worth noting that the jet structure and therefore Jet Energy Scale is flavour dependent: For example, weak decays involving neutrinos, which lead to an underestimation of the jet energy measured in the calorimeter, tend to occur more often in b-jets than in light-quark jets. Hence, the jet-energy scale is different for light-quark jets and b-quark jets. This has to be taken into account by introducing an additional **bJES uncertainty** that needs to be added in quadrature to the JES uncertainty to obtain the overall JES uncertainty for b-jets. Table 5.2 summarises the current[13] values of the bJES uncertainty for different p_T-ranges.

[11] It is also possible to apply a direct pile-up correction before the vertex correction as follows: Based on the number of primary vertices reconstructed in the event, the additional energy deposit stemming from multiple proton-proton interactions in the same bunch crossing is estimated and subtracted from the measured jet energy.
[12] December 2011.
[13] As of February 2012.

η region	Maximum fractional JES Uncertainty		
	$p_{\mathrm{T}}^{\mathrm{jet}}$= 20 GeV	200 GeV	1.5 TeV
$0 \leq \lvert\eta\rvert < 0.3$	4.1%	2.3%	3.1%
$0.3 \leq \lvert\eta\rvert < 0.8$	4.3%	2.4%	3.3%
$0.8 \leq \lvert\eta\rvert < 1.2$	4.4%	2.5%	3.4%
$1.2 \leq \lvert\eta\rvert < 2.1$	5.3%	2.6%	3.5%
$2.1 \leq \lvert\eta\rvert < 2.8$	7.4%	2.7%	
$2.8 \leq \lvert\eta\rvert < 3.2$	9.0%	3.3%	
$3.2 \leq \lvert\eta\rvert < 3.6$	9.3%	3.5%	
$3.6 \leq \lvert\eta\rvert < 4.5$	13.4%	4.9%	

Table 5.1.: Overview of the maximum fractional JES uncertainties for the anti-k_T algorithm with $R = 0.4$ in the EM+JES calibration scheme [46]

p_T range [GeV]	20 - 40	40 - 80	80 - 210	210 - 600	> 600
Maximum fractional bJES uncertainty	2.5 %	2.0 %	1.7 %	1.1 %	0.76 %

Table 5.2.: Overview of the maximum fractional bJES uncertainties for the anti-k_T algorithm with $R = 0.4$ in the EM+JES calibration scheme [51]

A precise knowledge of the JES and bJES is essential for precision measurements at hadron colliders that rely on the reconstruction of the final-state partons from the hadronic signatures in the detector. This is the case for the top-mass measurement in the semileptonic decay channel (and even more so in the allhadronic channel) where the JES uncertainty constitutes one of the dominant sources of systematic uncertainty on the top-quark mass.

5.5. Missing Transverse Energy (MET)

Once all the physics objects like electrons, muons and jets have been reconstructed, the **Missing Transverse Energy (MET, $\not{E}_T$)** can be calculated: As explained in Section 4.2.1, the transverse momenta of all the particles *produced in an event* sum up to zero because the momentum components of the initial-state partons orthogonal to the beam axis can be assumed to be zero and momentum is conserved in each direction.

However, the sum of transverse momenta *measured in the detector* may take non-zero values for two reasons:

- Weakly interacting particles may escape the detector without leaving any measurable signature. This is the case for Standard Model processes with at least one neutrino in the final-state like the semileptonic top-quark decays that are the object of this thesis. Moreover, some Beyond-the-Standard-Model (BSM) theories predict the existence of new particles like the Lightest Supersymmetric Particle (LSP) which only interact weakly and would therefore lead to large MET in the detector.

- Energy losses in inactive regions or dead cells that are not properly compensated for during re-calibration may also lead to a transverse momentum imbalance, the so-called **fake Missing Transverse Momentum** $\not{p}_T^{fake}$.

It is essential, in particular with regard to searches for BSM physics, to minimise or compensate for the effects that lead to $\not{p}_T^{fake}$. An overview of the various approaches to reconstruct and calibrate the Missing Transverse Energy can be found in [52] and [53]. A short explanation of the $\not{E}_T$ scheme used for this analysis can be found in Appendix C.4.

5.6. B-Tagging

The identification of jets originating from bottom quarks, the so-called **b-tagging**, is of particular importance for analyses involving top quarks because these almost exclusively decay into a W-boson and a bottom quark (see Section 3.2). In the analysis presented in this thesis, b-tagging serves a twofold purpose: During event selection, it can be used to suppress background processes with only light quarks in the final-state, thus increasing the purity of the $t\bar{t}$ sample (see Section 6). Moreover, it facilitates the event reconstruction for which the two light-quark jets from the hadronically decaying W-boson decay need to be distinguished from the b-jets stemming from the decay of the two top quarks (see Section 8).

Various b-tagging algorithms have been developed, all of which exploit one or several characteristic properties of b-jets: After hadronisation, the bottom quark is contained within a b-hadron that still carries about 70 % of the momentum of the original quark [52] and has a comparatively high mass[14] of more than 5 GeV. Consequently, its decay products tend to have large momenta transverse to the jet axis. Most important for b-tagging, though, is the fact that the lifetime τ of b-hadrons is relatively long - typically of the order of 1.5 ps - because their decay is governed by the weak interaction. This implies that b-hadrons traverse a measurable distance $\langle l \rangle = \beta\gamma c\tau$ in the detector before they decay: Under the above assumptions, the decay length $\langle l \rangle$ of a b-hadron inside a jet with a momentum of, for example, 50 GeV can be estimated to be roughly 3 mm.

This implies that the ID tracks associated to charged decay products of the b-hadron cannot be extrapolated back to the primary vertex of the event but have a non-zero impact parameter as illustrated in Figure 5.6.

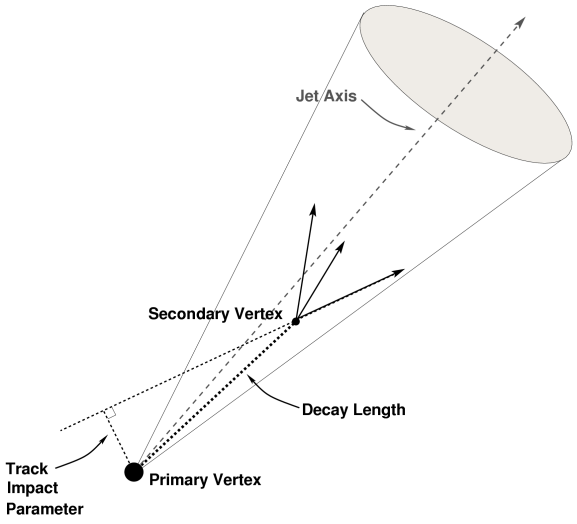

Figure 5.6.: Secondary vertex and decay length in a jet stemming from a bottom quark [54]

These tracks can be used to reconstruct the vertex associated to the b-hadron decay, the so-called

[14] Its mass is high compared to typical masses of hadrons formed of light quarks.

secondary vertex (SV), and measure its distance from the primary event vertex, the **decay length** L and, more importantly, its significance $\frac{L}{\sigma(L)}$. A jet is **tagged** as a b-jet if it has a secondary vertex with an associated decay-length significance above a certain threshold. Choosing a high cut value for the decay-length significance implies a high rejection rate $r_{uds,c}$ for light-quark (uds) and c-jets

$$r_{uds,c} = \frac{N(\text{true uds,c jets})}{N(\text{true uds,c jets tagged by the algorithm})}$$

or, in other words, a lower fraction of light jets accidentally tagged as b-jets. This, in turn, means a higher purity

$$\pi_b = \frac{N(\text{true b jets tagged by the algorithm})}{N(\text{all jets tagged by the algorithm})}$$

of true b-jets in the b-tagged sample but it also implies a reduced b-tagging efficiency

$$\epsilon_b = \frac{N(\text{true b jets tagged by the algorithm})}{N(\text{true b jets})}$$

because true b-jets that happen to have a lower decay-length significance are not tagged. The choice of the b-tagging threshold is therefore a trade-off between the requirement of a high purity/high rejection rate for non-b-jets and a high b-tagging efficiency.
In this analysis, the **SV0 algorithm**, which relies on the secondary-vertex b-tagging scheme outlined above, is used with a threshold value of the SV0 weight of > 5.85. An overview of the b-tagging performance at this cut value is given in Table 5.3. A more detailed description of the

SV0 cut	ϵ_b	π_b	r_{uds}	r_c
> 5.85	50.1 %	93.9 %	271	9

Table 5.3.: Performance of the SV0 algorithm for a cut value of 5.85 [55]

SV0 algorithm as well as an overview over alternative approaches can be found in [52]. For details on the performance of the SV0 algorithm see either [54] or [55].

6. Event Selection and Physical Background

Once the individual physics objects like electrons and jets have been reconstructed from the detector readings, they can be used to select the physics processes of interest. Semileptonic top-pair decays can be identified by the presence of a charged lepton with large transverse momentum, large Missing Transverse Energy and at least four highly energetic jets in the final state, two of which are b-jets. In this analysis, a cut-based approach is used to separate the semileptonic signal from the various background contributions.

6.1. Physical Background

The physical background to the semileptonic signal comprises all physics processes that may lead to a detector signature similar to that from a semileptonic top-pair decay. An overview of the dominant contributions to the physical background is given in this section.

6.1.1. Single Top

Single-top production has already been discussed in Section 3.1.1. Despite their comparatively small cross section of roughly 76 pb, these processes form an important part of the physical background because the presence of a top quark in the final state leads to considerable topological and kinematic similarities between single-top and $t\bar{t}$ semileptonic final-states. Hence these processes are most likely to pass the selection and cleaning cuts. (For a definition of the latter see Section 8.4). Figure 6.1

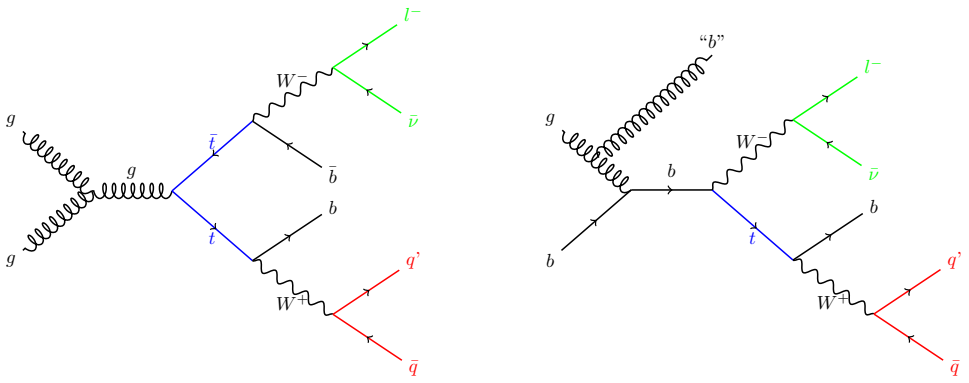

(a) Semileptonic signal process **(b)** Single-top background process

Figure 6.1.: Comparison of semileptonic (a) and single-top (b) final states

illustrates the similarities between the final-states of a semileptonic top-pair decay and a single-top process in the Wt-channel where the W decays leptonically, the top quark hadronically, and an additional jet arising from initial-state radiation is misidentified as a b-quark jet.

6.1.2. W + jets

The main contribution to the physical background in the semileptonic decay channel stems from events in which a W-boson is produced together with a number of strongly interacting partons that lead to hadronic jets. These processes are particulary important due to their comparatively large cross section and because the leptonic W decays may result in charged leptons with high transverse momentum as well as large Missing Transverse Energy which, in association with at least four additional hadronic jets, leads to detector signatures similar to that from semileptonic top-pair decays. This is illustrated in Figure 6.2a. B-tagging is particularly useful to reduce this background contribution, as will be shown in Section 6.3, because the fraction of b-jets among the additional jets in the event is small due to the high mass of the bottom quark.

6.1.3. Z + jets

Similarly, processes with a leptonically decaying Z boson and associated hadronic jets (Figure 6.2b) may fake a semileptonic signal, for example if one of the charged leptons from the Z decay is not reconstructed because it is emitted in a direction too close to the beam axis.

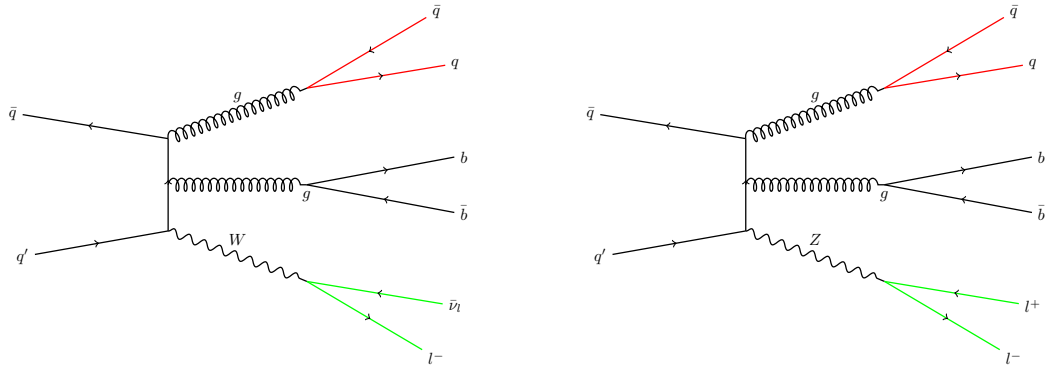

(a) W + jets background process

(b) Z + jets background process

Figure 6.2.: Examples of W+jets and Z+jets background processes

6.1.4. Diboson

Diboson processes can be categorised into processes with two W-bosons (WW), two Z-bosons (ZZ) or a W- and a Z-boson (WZ) in the final state. These processes may fake detector signatures of semileptonic top-pair decays if one boson decays leptonically, the other hadronically and additional jets occur in the event as illustrated in Figure 6.3a. However, due to their comparatively small cross section, dibosonic processes rank among the less significant background contributions in the semileptonic channel.

6.1.5. QCD Multijet

QCD multijet events, like the one illustrated in Figure 6.3b, are characterised by hard-scattering final states that contain only strongly interacting particles, i.e. quarks and gluons, but no leptons. There are, however, two processes that may lead to leptonic signatures in the detector:

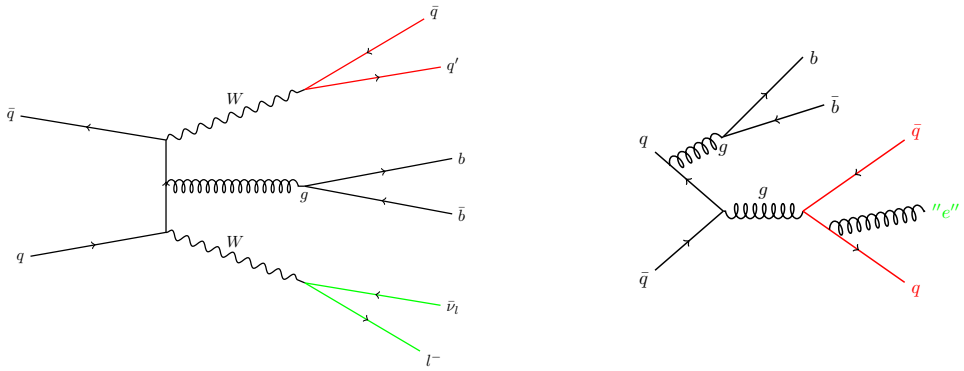

(a) WW + jets process

(b) QCD multijet background process with fake electron

Figure 6.3.: Examples of diboson and QCD multijet background processes

- Jets may be misidentified as electrons if the energy deposits in the electromagnetic calorimeter, for example from neutral-pion decays ($\pi^0 \to \gamma\gamma$), are unusually high. These jets are called **fake electrons**.

- Secondary, so called **non-prompt, leptons** may arise from weak hadron decays inside hadronic jets. If their momentum transverse to the jet axis is large, which is most likely to be the case for b-jets due to the high mass of b-hadrons, these leptons may pass the lepton isolation criteria (see Sections 5.2 and 5.3) and be identified as individual objects.

With a rate of approximately 1‰, both processes are extremely rare. Their significance for physics analyses at hadron colliders lies mainly in the huge cross section for QCD multijet events, which exceeds that of $t\bar{t}$ by several orders of magnitude.

Still, the QCD multijet background is among the minor contributions to the physical background in the semileptonic $t\bar{t}$ decay channel if appropriate selection cuts requiring both a charged lepton with high transverse momentum (Cut 2 in Section 6.2) and large MET (Cuts 8 and 9 in Section 6.2) are applied: Both the occurence of fake high-p_T leptons and large fake MET (see Section C.4) in QCD multijet events are relatively rare. For a QCD multijet event to pass the selection cuts, both (uncorrelated) processes have to coincide which is unlikely to happen frequently.

The QCD multijet contribution, in particular that of fake electrons, is hard to simulate and is therefore commonly estimated from data. By the end of 2011, no official tools for a data-driven estimate on a dataset larger than 1 fb^{-1} were available. Therefore, this background contribution is not included in the following analysis.

6.2. Selection Cuts

In the following, the selection cuts used to separate the semileptonic signal from the various background processes are presented: In this standard cut-based selection process, all events that might potentially be signal events are tested as to whether they fulfil a number of successively stricter conditions that have been optimised so that they should ideally be met by signal events only. At each stage, only events that pass a particular condition or **cut** are kept and passed on to the next stage while all other events are rejected. Only events that pass this so-called **cut-flow** are considered for further analysis.

While electrons, muons and taus occur with roughly equal probabilities in the leptonic branch of

semileptonic top-pair decays, only events with an electron (**e+jets channel**) or muon (μ+ **jets channel**) in the final state are selected for further analysis because they are significantly easier to identify and to reconstruct than events involving τ-leptons which are short-lived and decay via $\tau \to \nu_\tau W$ while still within the detector. The identification and reconstruction of these decays is problematic, firstly because they involve at least one neutrino, i.e. another source of Missing Energy, and secondly because, in roughly 65% of the cases [3], they decay hadronically and therefore give rise to additional jets.
Therefore, most analyses of semileptonic top-pair decays focus on the e+jets and μ+jets channels. These two channels have to be treated separately because the different final-states require a slightly different set of selection cuts. The results presented in this thesis have been obtained in the μ+jets channel.

The cut flow presented in this section is the official Top Working Group cut flow for ATHENA Release 16.6.5; for further details see [56]. Two additional cuts (Cut 15 and Cut 16) have been added to fit the particular requirements of this analysis.

- **Cut 0: Single-Lepton Trigger**[1]

  Keep only events with a leptonic detector signature, i.e. events which have passed the chosen event-filter trigger:

  - e+jets: EF_e20_medium, i.e. there is at least one electron candidate with $p_T > 20$ GeV
  - μ+jets: EF_mu18, i.e. there is at least one muon candidate with $p_T > 18$ GeV

- **Cut 1: Vertex quality requirement**

  The reconstructed primary event vertex must have at least 4 associated tracks.

- **Cut 2**

  - e+jets: Require at least one electron with $E_T > 25$ GeV
  - μ+jets: Require at least one muon with $p_T > 20$ GeV

  Here and in the following, only isolated electrons and muons are considered that have been reconstructed according to the object definitions introduced in the previous chapter (see Sections 5.2 and 5.3).

- **Cut 3**[2]

  - e+jets: Require exactly one electron with $E_T > 25$ GeV
  - μ+jets: Require exactly one muon with $p_T > 20$ GeV

- **Cut 4**

  - e+jets: No muon with $p_T > 20$ GeV
  - μ+jets: No electron with $E_T > 25$ GeV

[1] On data, the Good Runs List (GRL) is to be applied before Cut 0.
[2] The successively stricter cuts on the lepton numbers have been introduced to gain a better understanding of the lepton multiplicity in the various background contributions and to allow detailed cut-flow comparisons between the different working groups.

- **Cut 5: Trigger Matching**

  The selected lepton matches the corresponding trigger object within a cone of $\Delta R < 0.15$. For details on the trigger matching for electrons and muons consult [44].

- **Cut 6: Electron-Muon Overlap Removal**

  Remove events which contain an electron and a muon that have been reconstructed with the same ID track.

- **Cut 7: Jet Cleaning (data only)**

  Remove events in which at least one jet with $p_T > 20$ GeV is tagged as *bad* according to the loose jet-quality criterion. This cut is introduced to remove events with fake/background jets that may arise, for example, from calorimeter noise. For details on jet-quality criteria see [46].

- **Cut 8: MET Cut**

  In semileptonic events, the presence of one neutrino from the leptonic W-boson decay leads to Missing Transverse Energy (MET). To distinguish these signal events from QCD-multijet events in which fake MET may arise from calorimeter effects (see Section C.4), the MET in the selected events is required to lie above a certain threshold:

  - e+jets: MET > 35 GeV
  - μ+jets: MET > 20 GeV

- **Cut 9: W-boson Transverse Mass Cut**

  - e+jets: $M_W^T > 25$ GeV
  - μ+jets: MET + $M_W^T > 60$ GeV (**Triangular Cut**)

  M_W^T stands for the transverse invariant mass of the leptonically decaying W-boson which is defined as

  $$(M_W^T)^2 = (p^{MET} + p^l)^2$$

  where p^{MET} and p^l are the four-vectors of the MET object and the charged lepton (which is assumed to be massless), respectively.

  Like the MET cut, this cut primarily aims at rejecting QCD-multijet background.

- **Cut 10**

  Require at least two jets with $E_T > 25$ GeV and $|\eta| < 2.5$

- **Cut 11**[3]

  Require at least three jets with $E_T > 25$ GeV and $|\eta| < 2.5$

[3] As is the case of the cuts on the lepton number (Cuts 2 and 3), the successively stricter cuts on the jet number have been introduced to gain a better understanding of the jet multiplicity in the various background contributions and to allow detailed cut-flow comparisons between the different working groups.

- **Cut 12**

  Require at least four jets with $E_T > 25$ GeV and $|\eta| < 2.5$

- **Cut 13: At least 1 b-tag**

  Require at least one of the jets with $E_T > 25$ GeV and $|\eta| < 2.5$ has an SV0 weight > 5.85

- **Cut 14: LAr flag cut**[4]

  Remove events in which noise bursts occurred in the LAr calorimeter.

- **Cut 15: At least 1 b-tag and at least two non-b-tagged jets**

  Require at least two non-b-tagged jets. This is important for the reconstruction of the hadronic branch (see Section 8) where the two light-quark jets from the hadronic W decay need to be identified. Events for which one of these jets has not been reconstructed or accidentally tagged as a b-jet are therefore rejected during the selection process.

- **Cut 16: Exactly 2 b-tags**

  Require that exactly two of the jets with $E_T > 25$ GeV and $|\eta| < 2.5$ have an SV0 weight > 5.85

Figure 6.4 shows the cut-flow histograms with the different signal and background contributions (excluding the QCD multijet background). All samples here and in the following, unless stated otherwise, have been normalised to an integrated luminosity of 5.0 fb^{-1}. For details on the Monte Carlo samples used in this study see Appendix D.

The upper plot with a linear scale on the y-axis serves to illustrate the overall efficiency of the individual cuts as well as the fact that the background is dominated by the W+jets processes. In the lower plot, a logarithmic scale has been chosen for the y-axis in order to resolve the smaller background components such as single-top or diboson processes and to illustrate the increasing signal purity, in particular after Cuts 12 and 16. A quantitative discussion of the cut-flow is given in the next Section.

[4] This cut is only relevant for data from Period E onwards. It has only been included here for the sake of completeness and to allow a full comparison with the official Top Working Group event selection.

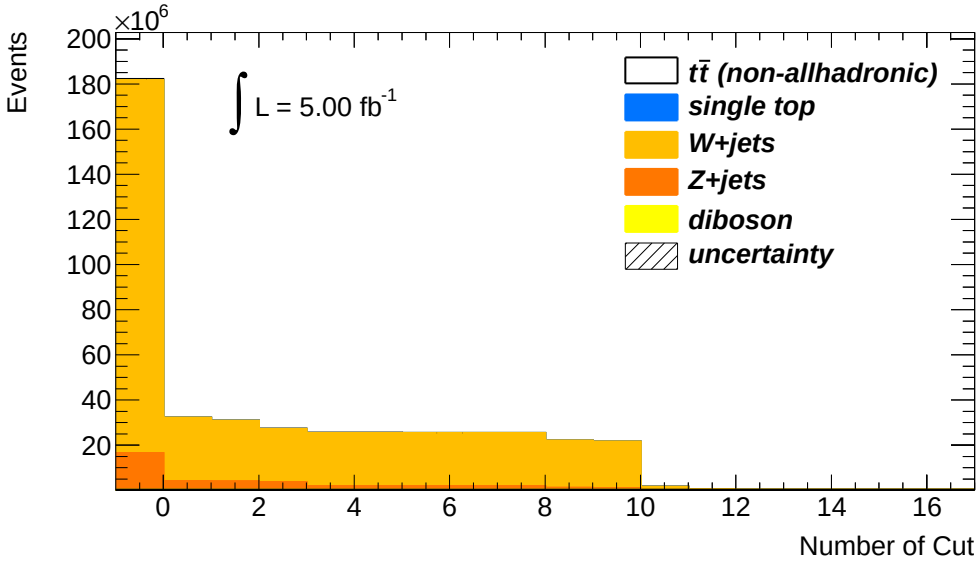

(a)

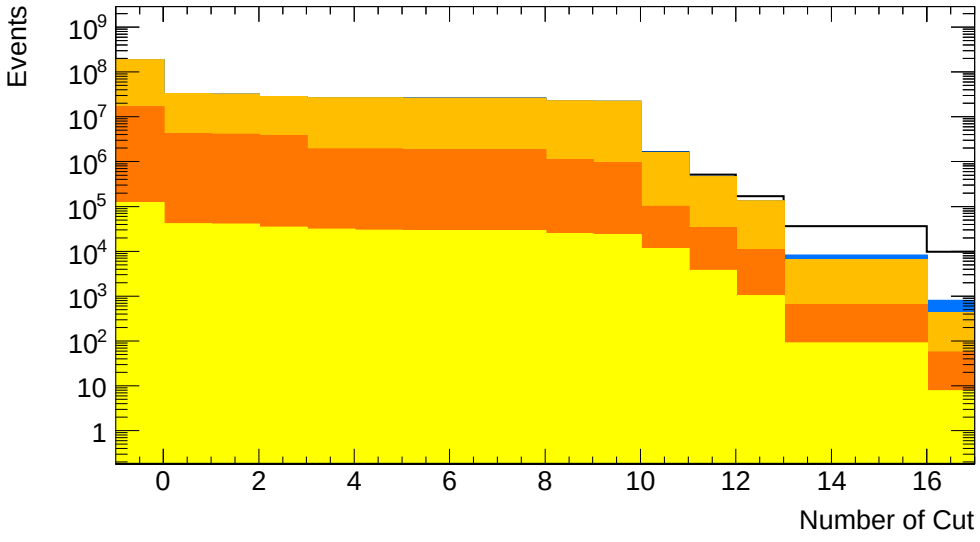

(b)

Figure 6.4.: Cut-flow histogram for signal and background events with (a) linear scale and (b) logarithmic scale on the y-axis

6.3. Evaluation of the Selection Cuts

It is not possible to entirely separate the semileptonic signal from the various background processes: Even if very tight selection cuts are applied, there may still be some background events with a detector signature similar enough to that of semileptonic top-pair decays (see Section 6.1) to pass the selection cuts. In order to quantify these "impurities" stemming from remaining background events, the concept of **signal purity** π_S has been introduced as the fraction of signal events after a particular cut:

$$\pi_{signal} = \frac{N(\text{signal events})}{N(\text{signal events}) + N(\text{all background events})} \tag{6.1}$$

Similarly, the fractions of background events can be calculated in order to evaluate the effect of a cut on a particular background process.

In principle, the signal purity can be increased by applying stricter cuts that remove more background events. However, each cut generally also removes some signal events: This may, for example, happen if not all of the jets from a semileptonic top-pair decay have been reconstructed, either because jets are too close to the beam axis or because jets stemming from the decays of highly-boosted particles are so close together that they are reconstructed as a single jet. Moreover, not all jets in semileptonic events may pass the minimum p_T threshold of 25 GeV. In these cases, signal events may be rejected by Cuts 10, 11 or 12. Hence, stricter cuts always lead to a reduction of the number of events available for further analysis which implies larger statistical errors on measured quantities such as the top-quark mass. To estimate the effect of cuts on the number of signal events, the **signal efficiency**

$$\epsilon_S = \frac{N(\text{signal events after Cut X})}{N(\text{signal events before all cuts})} \tag{6.2}$$

defined here with respect to the number of signal events before the cut-flow, can be calculated. The efficiencies for the individual background contributions are defined accordingly.[5]

Choosing and optimising a set of selection cuts therefore always means finding a compromise between a high signal purity on the one hand and a high signal efficiency on the other.

Table 6.1 summarises the efficiencies of selected cuts for the signal and the different background components with respect to the respective numbers of events before the cut-flow. The corresponding fractions of the signal and background contributions are given in Table 6.2 where the first line corresponds to the signal purity defined in Equation 6.1. The cuts have been chosen to illustrate the effect of b-tagging on the signal efficiency and purity: After Cut 12, the selected events fulfil all requirements of the semileptonic events selection except for the fact that b-tagging has not been used in the selection process yet. Cut 15 corresponds to the case where at least one jet is required to be b-tagged, Cut 16 stands for the stricter requirement that there are exactly two b-tagged jets in the event.

These numbers clearly illustrate the importance of b-tagging for the event selection: Requiring at least one b-tag reduces the fraction of W+jets background events from 69.3% after Cut 12 to 15.7%

[5] Throughout this thesis, all efficiencies and purities as well as their uncertainties are calculated according to the formulas in Appendix A which take into account the fact that the $t\bar{t}$ and single-top samples, generated with MC@NLO, contain events with both positive and negative weights of absolute value 1.

	after Cut 12 (no b-tagging)	**after Cut 15 (1 b-tag)**	**after Cut 16 (2 b-tags)**
$t\bar{t}$ (non-allhadronic)	$(8.75 \pm 0.04)\%$	$(6.35 \pm 0.04)\%$	$(2.03 \pm 0.02)\%$
single top	$(1.42 \pm 0.03)\%$	$(0.87 \pm 0.02)\%$	$(0.20 \pm 0.01)\%$
W + jets	$(7.18 \pm 0.02) \cdot 10^{-2}\%$	$(3.46 \pm 0.05) \cdot 10^{-3}\%$	$(2.2 \pm 0.1) \cdot 10^{-4}\%$
Z + jets	$(6.0 \pm 0.1) \cdot 10^{-3}\%$	$(3.3 \pm 0.1) \cdot 10^{-3}\%$	$(2.9 \pm 0.4) \cdot 10^{-4}\%$
diboson	$(0.83 \pm 0.03)\%$	$(7 \pm 1) \cdot 10^{-2}\%$	$(6 \pm 2) \cdot 10^{-3}\%$

Table 6.1.: Signal and background efficiencies of selected cuts evaluated with respect to the respective number of events before all cuts (see Equation 6.2)

	before all cuts	**after Cut 12 (no b-tagging)**	**after Cut 15 (1 b-tag)**	**after Cut 16 (2 b-tags)**
$t\bar{t}$ (non-allhadronic)	$(0.2452 \pm 0.0004)\%$	$(22.9 \pm 0.1)\%$	$(78.1 \pm 0.2)\%$	$(92.0 \pm 0.3)\%$
single top	$(0.1025 \pm 0.0002)\%$	$(1.55 \pm 0.03)\%$	$(4.5 \pm 0.1)\%$	$(3.7 \pm 0.2)\%$
W + jets	$(90.651 \pm 0.002)\%$	$(69.3 \pm 0.1)\%$	$(15.7 \pm 0.2)\%$	$(3.7 \pm 0.2)\%$
Z + jets	$(8.936 \pm 0.002)\%$	$(5.7 \pm 0.1)\%$	$(1.5 \pm 0.1)\%$	$(0.5 \pm 0.1)\%$
diboson	$(0.0654 \pm 0.0002)\%$	$(0.58 \pm 0.01)\%$	$(0.24 \pm 0.03)\%$	$(0.08 \pm 0.03)\%$

Table 6.2.: Signal purity and fractions of background events after selected cuts evaluated with respect to the total number of events after the respective cut (see Equation 6.1)

after Cut 15 and to only 3.7% if exactly two b-tags are required (Cut 16). A similar reduction can be observed in the number of Z+jets events. At the same time, the signal purity increases from 22.9% without b-tagging (after Cut 12) to 78.1% if one b-tag is required (Cut 15) and to even 92.0% if only events with exactly two b-tags are required.

It should also be noted that, as mentioned in Section 6.1, the fraction of single-top events even increases slightly during the event selection process because these events tend to be more similar to semileptonic $t\bar{t}$ events and are therefore more likely to pass the stricter cuts on the jet numbers and the b-tagging than W+jets or Z+jets events.

7. Estimators for the Top-Quark Mass

In the semileptonic decay channel, the top-quark mass is commonly determined from the properties of the decay products of the **hadronically decaying top quark**: the two light-quark jets from the W-boson decay and the corresponding b-quark jet.[1] There are various approaches to calculating the mass of the top quark from the measured properties of the three jets which may differ significantly in their dependence on the different sources of systematic uncertainty such as the jet-energy scale (JES). In this section, three estimators for the top-quark mass are introduced: The invariant three-jet mass $m_{3\text{jet}}$ and the two improved estimators $m_{\text{top, ratio}}$ and $m_{\text{top, angle}}$ which have been specifically designed to yield a reduced JES dependence of the top-quark mass.

7.1. The Invariant Three-Jet Mass

The most straight-forward approach to determining the mass of the top quark is to calculate the invariant mass $m_{3\text{jet}}$ of its three decay products which, due to energy and momentum conservation, equals the top-quark mass:

$$m_{3\text{jet}} = \sqrt{\left(\sum_{jet=1}^{3} E_{jet}\right)^2 - \left(\sum_{jet=1}^{3} \vec{p}_{jet}\right)^2} \tag{7.1}$$

As Equation (7.1) clearly illustrates, this mass estimator exclusively relies on the measurement of the energies and momenta of the three jets and is therefore expected to be extremely sensitive to variations of the JES:

Assuming, for simplicity, a global JES factor, i.e. a re-scaling of all measured jet energies and momenta by a constant factor j that is applied to all jets in an event independent of their transverse momenta and pseudorapidities[2]

$$E_{jet} \longrightarrow j \cdot E_{jet} \tag{7.2}$$
$$\vec{p}_{jet} \longrightarrow j \cdot \vec{p}_{jet}, \tag{7.3}$$

the invariant three-jet mass turns out to be directly proportional to that scale factor:

[1] It should be noted that it is also possible to use the leptonic branch for a mass measurement despite the fact that the presence of a neutrino in the final state of the leptonic W-boson decay renders the system of kinematic equations underconstrained. For details see [57].

[2] In this simplified model, the scale factor j essentially replaces the energy- and pseudorapidity-dependent correction factor $\mathcal{F}^{-1}(E_{EM}^{jet})|_{\eta_{det}}$ introduced in Equation (5.2).

$$m_{3\text{jet}} \longrightarrow m'_{3\text{jet}} = \sqrt{\left(\sum_{jet=1}^{3} j \cdot E_{jet}\right)^2 - \left(\sum_{jet=1}^{3} j \cdot \vec{p}_{jet}\right)^2} = j \cdot m_{3\text{jet}} \tag{7.4}$$

and hence the JES uncertainty directly translates into a systematic uncertainty on $m_{3\text{jet}}$.

7.2. The 3-to-2-Jet Invariant Mass Ratio

On the basis of the considerations concerning the JES dependence of $m_{3\text{jet}}$ in the previous section, an improved mass estimator $m_{\text{top, ratio}}$ with a reduced JES dependence has been introduced (see [58]):

Instead of taking the top-quark mass to be the invariant mass of its three decay products, the latter is divided by the invariant mass m_{2jet} of the two jets from the W-boson decay and this ratio is re-scaled by the W-boson mass m_W^{PDG} as stated by the Particle Data Group ($m_W^{PDG} = 80.399 \pm 0.023$ GeV [3]) to yield the top-quark mass.

$$m_{\text{top, ratio}} = \frac{m_{3\text{jet}}}{m_{2\text{jet}}} \cdot m_W^{PDG} \tag{7.5}$$

This mass estimator has the advantage that any global JES factors will cancel out between the numerator and the denominator

$$m_{\text{top, ratio}} \longrightarrow m'_{\text{top, ratio}} = \frac{j \cdot m_{3\text{jet}}}{j \cdot m_{2\text{jet}}} \cdot m_W^{PDG} = m_{\text{top, ratio}}. \tag{7.6}$$

Although the assumption of a global JES factor is a simplification of Equation (5.2) which takes into accounting the transverse-momentum and pseudorapidity dependence of the JES, it can be shown (see again [58] and Section 9.2) that the top-quark mass determined with this estimator has a reduced JES dependence compared to the top-quark mass determined with the estimator $m_{3\text{jet}}$.

7.3. The Determination of the Top-Quark Mass from the Angles between Jets

The two mass estimators introduced in the previous sections both exclusively rely on the measurement of the energies and momenta of the three jets from the top-quark decay. The determination of these quantities is intimately related to that of the jet-energy scale and its uncertainty which, as outlined in Section 5.4.4, is a challenging task due to the multitude of effects that have to be taken into account.

This calls for an alternative approach to determining the invariant mass of the top quark. The introduction of the new mass estimator described in this section is motivated by the fact that angles between jets can be measured much more accurately than their energies and momenta and

that it is therefore advantageous to express the top-quark mass in terms of the angles between its decay products only. This can be achieved by using the kinematic properties of the decay in the restframe of the top quark. In this frame, momentum conservation dictates that the b-quark and the W-boson from the top-quark decay are emitted back-to-back which implies that the three momentum vectors $\vec{j_b}$, $\vec{j_1}$ and $\vec{j_2}$ of the b-quark jet and the two light-quark jets, respectively, lie in the same plane. This is illustrated in Figure 7.1.

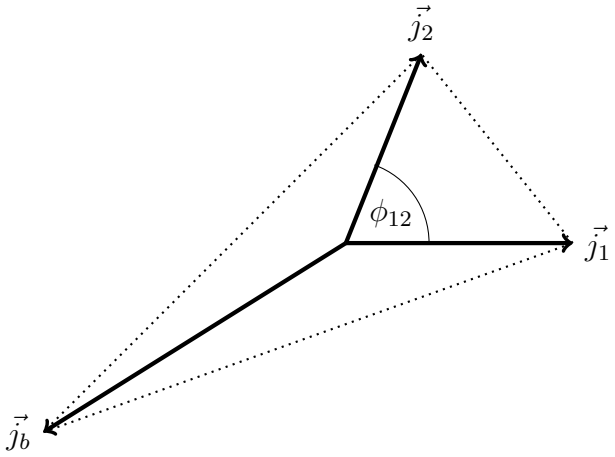

Figure 7.1.: Momentum vectors of the two light-quark jets $\vec{j_1}$ and $\vec{j_2}$ and the b-quark jet $\vec{j_b}$ in the restframe of the hadronically decaying top quark

The kinematics of the decay in this plane, given by the **shape of the triangle** that is formed by the ends of the three momentum vectors, is then - up to a global scale factor - uniquely determined by the **angles** ϕ_{12}, ϕ_{1b} and ϕ_{2b} between the three jets in this plane. The energy scale, given by the **size of the triangle**, is fixed by introducing the **W-boson mass** m_W^{PDG} as a reference point, similar to the re-scaling of the 3-to-2 jet invariant-mass ratio in the previous section.

The resulting expression for the mass estimator $m_{\text{top, angle}}$ is then given by the following equation:

$$\left(\frac{m_W}{m_{\text{top, angle}}}\right)^2 = \frac{2 \cdot \sin(\phi_{1b}) \cdot \sin(\phi_{2b}) \cdot [1 - \cos(\phi_{12})]}{[\sin(\phi_{12}) + \sin(\phi_{1b}) + \sin(\phi_{2b})]^2}. \tag{7.7}$$

The details of the analytical derivation of this equation can be found in Appendix E.

It should be noted that Equation (7.7) does not contain any **explicit** dependence on measured jet energies or momenta: The dimensionless ratio of the two invariant masses - $m_{\text{top, angle}}$ which is to be measured, and m_W^{PDG} which has been determined to great accuracy by previous experiments - is expressed in terms of the angles ϕ_{12}, ϕ_{1b} and ϕ_{2b} only.

These angles, however, cannot be measured directly because they are defined in the **restframe of the top quark** which is, in general, **boosted with respect to the laboratory frame** in which all quantities are measured. In order to determine the angles on the right-hand side of Equation (7.7) it is therefore necessary to measure the Lorentz boost of the hadronically-decaying top quark which, in turn, requires a measurement of the energies and momenta of the jets from its decay. Hence, the new mass estimator is expected not to be completely independent of the jet-energy scale. Its JES dependence is evaluated and compared to that of the other two mass estimators in Section 9.2.

8. Event Reconstruction and Combinatorial Background

Once the semileptonic events have been selected, the hadronically-decaying top quark needs to be reconstructed from its decay products. This means that among the four or more jets in the event the two light-quark jets from the decay of the corresponding W-boson as well as the b-quark jet from the hadronic branch have to be identified.

Events for which **both** the b-quark jet from the hadronic decay and the corresponding W-boson have been reconstructed correctly are called **signal events**. All other events form the **combinatorial background**. For a discussion of the combinatorial background see Section 8.1.

Various **reconstruction strategies** that rely on topological and/or kinematic properties of the semileptonic top-pair decays have been developed, an overview of which can be found in [59] and [60]. In Sections 8.3 and 8.4, two of the most promising strategies as well as a number of **cleaning cuts**, which can be applied to reduce the combinatorial background, are introduced and compared with particular regard to their suitability for a measurement of the top-quark mass with the three mass estimators introduced in Section 7.

All studies involving the combinatorial background are performed on a sub-sample of the non-allhadronic signal Monte-Carlo sample for which all decay products of the top and anti-top quarks can be matched to a reconstructed object at detector level such as an electron or jet, thus allowing to test whether the top quark has been reconstructed correctly. The method of **jet-parton matching** is described in Section 8.2.

Section 8.5 summarises the effects of the chosen cleaning cuts on the complete set of signal and physical-background samples with particular regard to the overall signal efficiency and purity.

Throughout this chapter, two sets of selected events are analysed and compared: The first set consists of events with at least one b-tagged jet which are selected by applying the selection cuts up to and including Cut 15 (see Section 6.2). This set will be referred to as the **1 b-tag case**. The second set, referred to as the **2 b-tags case**, comprises only events that fulfil the stricter requirement of containing exactly two b-tagged jets, which means that these events have passed all selection cuts up to and including Cut 16.

8.1. Combinatorial Background

The classification of the selected semileptonic events as either signal or combinatorial background events crucially depends on the requirements of the particular method that is chosen for the measurement of the top-quark mass: In the simplest case where the top-quark mass is taken to be the invariant mass of the three jets from the hadronic top-quark decay, $m_{3\text{jet}}$, it is sufficient to choose the three right jets out of the four or more jets in the event without having to distinguish between the b-quark jet and the two light-quark jets. The two more sophisticated mass estimators, $m_{\text{top, ratio}}$ and $m_{\text{top, angle}}$ as introduced in Section 7, however, require the identification of the two light-quark jets among the three jets from the hadronically-decaying top quark, i.e. the additional reconstruction of the hadronically-decaying W-boson. Therefore, in the following, only events in

which **both** the top quark from the hadronic branch **and** the corresponding W-boson have been correctly reconstructed are called signal events while all other events are classified as combinatorial background.

In an event with exactly four jets and no b-tagging information there are six possibilites to choose the two light-quark jets and another two possibilites to choose the b-quark jet belonging to the hadronic branch from the two remaining jets. Hence there are twelve possibilites to completely reconstruct the hadronic branch if all jets are chosen randomly, i.e. without using any additional geometric or kinematic properties of the semileptonic decays. Only one of these twelve possible assignments is correct which means that the fraction of correctly reconstructed events, the signal purity, is expected to be roughly 8%.

The situation is complicated further by the presence of additional jets in the event, for example from initial- or final-state radiation (see Section 3.1.2 for an overview of 2→3 processes). With only one additional jet and no b-tagging information available, the number of possibilities to reconstruct the hadronic branch rises to 30 and the signal purity is accordingly expected to drop to about 3%.

It is possible in principle to reduce the combinatorial background by selecting only semileptonic events with exactly four jets in the final state for the mass measurement. However, this additional selection cut results in a considerable loss of statistics since more than half of the events that remain after the event selection process presented in Section 6.2 have more than four jets in the final state (see Figure 8.1). It will also be shown in Section 8.5 that, for the purpose of this analysis, cutting on the number of jets does not yield any considerable advantage. Therefore, no upper bound on the jet multiplicity is used in the following analysis.

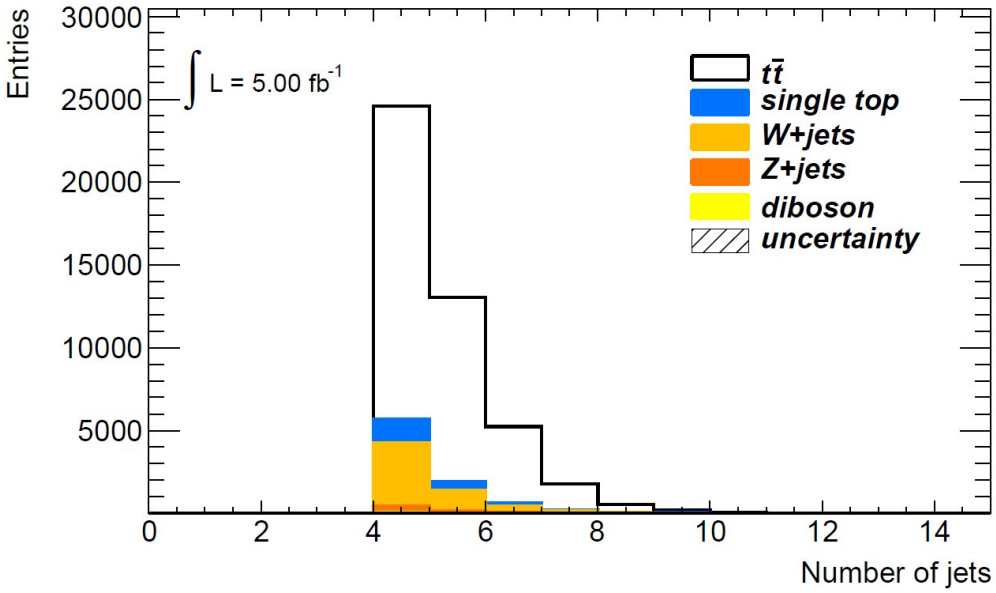

Figure 8.1.: Jet multiplicity in $t\bar{t}$ signal and physical background events after selection cuts (1 b-tag case)

B-tagging turns out to be extremely useful in order to restrict the number of possibilites of choosing a wrong combination of jets, thereby reducing the combinatorial background: If in a four-jet event one of the b-jets is tagged, there are only three possibilities to choose the two light-quark jets among the three non-b-tagged jets and therefore only six possbilities to reconstruct the hadronic top-quark decay. If both b-jets are tagged, the two non-b-tagged jets are automatically assigned to the hadronically-decaying W-boson, leaving only two possibilities to identify the right b-jets among the two tagged jets. In an event with five jets, the number of possible jet assignments is reduced

from 30 to 18 in the case of 1 b-tag and to only six if two jets are b-tagged. Hence b-tagging is not only a valuable tool for reducing the physical background in the event selection process, as shown in the previous section, but also for minimising the combinatorial background that arises from the reconstruction of the hadronic top-quark decay.

8.2. Jet-Parton Matching

In order to test whether the right jets have been assigned to the hadronically-decaying top quark and to evaluate and compare the different reconstruction algorithms, the jets in the event need to be identified with the final-state partons. The information about the latter, the so-called **truth information**, is contained in the Monte-Carlo samples. The procedure of assigning the reconstructed jets to the final-state partons is called **jet-parton matching** and has been implemented as follows:

1. Firstly, for each event, the complete information about the $t\bar{t}$ final state is retrieved from the Monte-Carlo sample. The latter contains a list of all the simulated particles that occur in an event, including information about their flavour, their four-momentum and their decay product(s). This information can be used to identify the six particles from the decays of the top and the anti-top quark in the non-allhadronic signal sample, i.e. the two b-quarks and the four particles from the decays of the two W-bosons.

   It should be noted that the parton-level information contained in the Monte-Carlo samples can be used to identify the dileptonic events in the non-allhadronic signal sample that pass the selection cuts. In both the 1 b-tag and the 2 b-tags case, the fraction of remaining dileptonic events is roughly 13 %. The fact that the additional cut on the number of b-jets has no effect on the fraction of remaining dileptonic events is not suprising because dileptonic and semileptonic final-states only differ in the decay of one W-boson but contain the same number of b-quarks.

   This procedure further reveals that in the majority of these dileptonic events, one of the W-bosons decays into a τ-lepton which in turn decays hadronically, thus giving rise to a detector signature similar to that of semileptonic top-pair decays.

2. Secondly, only events for which the four truth quarks and the charged truth lepton fulfil the requirements $|\eta| < 2.5$ and $p_T > 0.5$ GeV are considered in the jet-parton matching. These cuts are introduced in order to obtain a realistic matching efficiency: Since only jets with a pseudorapidity $|\eta_{jet}| < 2.5$ are selected for the analysis, the same requirement should be placed on the partons to which they are to be matched. The cut on the minimum transverse momentum of the jet ($p_{T,jet} > 25$ GeV) cannot directly be applied to partons because, as outlined in Section 5.4.4, the relation between the momenta at jet and parton level is non-trivial. Therefore, it is common practice to require the partons to only fulfil the minimal transverse momentum condition $p_T > 0.5$ GeV which is the threshold above which particles can be detected by ATLAS.

3. The matching of jets to partons is performed on the basis of the geomentric distance parameter $\Delta R = \sqrt{(\Delta\eta)^2 + (\Delta\phi)^2}$:

   - A hadronic jet is assigned to a truth quark if and only if ΔR(jet, quark) < 0.3 and there is no other jet within a cone of $\Delta R < 0.3$ around the truth quark.

   - A reconstructed electron or muon is assigned to the corresponding truth particle if ΔR(reconstructed lepton, truth lepton) < 0.1. The distance requirement for leptons is stricter than the one for hadronic jets because, as explained in Section 5.4.4, the fact

that leptons are colourless particles and therefore not subject to confinement allows the reconstructed electrons and muons to be related more directly to the original truth particle.

4. The jet-parton matching is considered complete if the four final-state quarks as well as the charged lepton have been uniquely matched to the hadronic jets or to the reconstructed charged lepton at detector level, respectively.

The efficiency of the jet-parton matching ϵ_{JPM} is commonly evaluated with respect to the number of events that are selected for matching in step 2 of the above procedure:

$$\epsilon_{JPM} = \frac{N(\text{semileptonic events with complete jet-parton matching})}{N(\text{semileptonic events selected for matching according to step 2})}. \tag{8.1}$$

Table 8.1 summarises the values of ϵ_{JPM} as well as, for completeness, the jet-parton matching efficiency with respect to the complete non-allhadronic sample after event selection

$$\epsilon'_{JPM} = \frac{N(\text{semileptonic events with complete jet-parton matching})}{N(\text{non-allhadronic events after selection cuts})}. \tag{8.2}$$

both for the 1 b-tag and the 2 b-tags case.

	1 b-tag	2 b-tags
ϵ_{JPM}	$(25.9 \pm 0.1)\%$	$(29.1 \pm 0.1)\%$
ϵ'_{JPM}	$(19.4 \pm 0.1)\%$	$(22.7 \pm 0.1)\%$

Table 8.1.: Jet-parton matching efficiencies ϵ_{JPM} and ϵ'_{JPM} for the 1 b-tag and the 2 b-tags case

These values demonstrate that only in a minority of events all four quarks as well as the charged lepton can be uniquely identified with a corresponding object at detector level. Various effects may lead to an incomplete jet-parton matching:

For example, the two light-quark jets from a highly boosted W-boson may be collimated in the direction of the momentum vector of the original W-boson and be therefore so close together that each lies within the $\Delta R < 0.3$ - cone around the truth quark corresponding to the other jet. Similarly, additional jets, in particular those from final-state radiation may lie close to a quark jet from the hard-scattering process. In both cases, the jet corresponding to the truth parton cannot be uniquely identified. It is also possible that the momentum direction of a jet is significantly altered by the emission of final-state radiation so that it does not lie within the $\Delta R < 0.3$ - cone around the original quark. Moreover, it may happen that one of the jets stemming from a quark from the hard process is not reconstructed, for instance because it is too close to the beam axis, and that instead an additional jet, for example one arising from initial- or final-state radiation, passes the selection cuts. This also explains the fact that the matching efficiencies are slightly higher in the 2 b-tags case because the stricter selection cut ensures that only events in which both b-quark jets have been reconstructed are considered for the matching.

It is important to keep these matching efficiencies in mind because it is only on this limited subset of the non-allhadronic signal sample that the reconstruction methods, cleaning cuts and the shape of the combinatorial background can be evaluated. The latter is of particular importance for the determination of the function which is to be fitted to the top-mass distribution in order to determine the top-quark mass. For further details on the fit see Section 9.1.

8.3. Reconstruction Algorithms

Various geometric and kinematic properties of the top-quark decay can be exploited in order to assign the right jets to the hadronically-decaying top quark and the corresponding W-boson. A comprehensive overview can be found in [59]. In the following, two of the most promising reconstruction methods are introduced and compared with particular regard to their suitability for the new mass estimator, $m_{\text{top, angle}}$, introduced in Section 7.3.

8.3.1. The ΔR-method

The ΔR-method is a reconstruction algorithm that relies solely on the geometric-distance measure $\Delta R = \sqrt{(\Delta\eta)^2 + (\Delta\phi)^2}$. It was originally developed for the early data-taking period at the LHC because it does not use jet energies and momenta or any related quantities such as invariant masses and is therefore particularly suited for measurements performed with a not yet fully calibrated calorimeter and correspondingly large uncertainties on the jet-energy scale.

The basic idea behind this reconstruction method is that, since the top and anti-top quark are emitted back to back in their centre-of-mass frame, the decay products of the hadronically-decaying top quark should on average be closer to each other than to those of the corresponding anti-quark. A similar argument applies to the decay products of the hadronically-decaying W-boson, the two light-quark jets, which are on average closer to each other than to the b-quark of the hadronic branch. Of course, the situation is complicated by the fact that, in general, the top-anti-top pair is boosted with respect to the laboratory frame which results in the decay products being collimated in the direction of the boost. Monte-Carlo studies, however, show that despite this fact the ΔR-method constitutes a suitable reconstruction method (see again [59] as well as the results shown in this section).

The ΔR-algorithm has been implemented as follows:

1. The distance parameters $\Delta R_{i,j}$ for all pairs of jets (i, j) are calculated.

2. The pair of non-b-tagged jets with the smallest value of $\Delta R_{i,j}$ is chosen to be the two light-quark jets from the hadronic W-boson decay.

3. The (not necessarily b-tagged) jet closest to the reconstructed W-boson is taken to be the b-quark jet from the hadronic branch.

4. If there is a second b-tagged jet in the event, it is defined to be the b-quark jet from the leptonic branch.

8.3.2. The χ^2-method

Another possibility to reconstruct the hadronic branch is to perform a χ^2-fit that takes the W-boson mass m_W^{fit} and width σ_W^{fit}, obtained from a fit to the respective Monte-Carlo signal distribution, as input variables in order to identify the two light-quark jets from the W-boson decay. The b-quark jet is then chosen exactly like in the ΔR-method.

The χ^2-algorithm is implemented similarly to the ΔR-algorithm:

1. The χ^2-values for all pairs of jets (i, j) are calculated as follows:

$$\chi^2_{i,j} = \left(\frac{m_{i,j} - m_W^{\text{fit}}}{\sigma_W^{\text{fit}}} \right)^2$$

where $m_{i,j}$ stands for the invariant mass of the two jets i and j.

2. The pair of non-b-tagged jets with the smallest value of $\chi^2_{i,j}$ is chosen to be the two light-quark jets from the hadronic W-boson decay.

3. The (not necessarily b-tagged) jet which, in terms of ΔR, is closest to the reconstructed W-boson is taken to be the b-quark jet from the hadronic branch.

4. If there is a second b-tagged jet in the event, it is defined to be the b-quark jet from the leptonic branch.

This kinematic fit has the advantage that it relies on Lorentz-invariant quantities to reconstruct the W-boson and that therefore the actual boost of the top quark, which varies from event to event, does not have an influence on this reconstruction step. Moreover, this method can be easily extended to include further input variables, such as the energy distributions of the two jets from the W-boson decay which allows a simultaneous determination of the jet-energy scale. For details see again [59].

8.3.3. Comparison of the Reconstruction Algorithms

Table 8.2 summarises the signal purities

$$\pi_{signal} = \frac{N(\text{signal events})}{N(\text{signal events}) + N(\text{combinatorial-background events})}$$

for the two reconstruction methods both for the 1 b-tag and the 2 b-tag case. As expected, the purities in the latter case are considerably higher due to the extra constraints on the combinatorics introduced by the use of two b-tags. Moreover, in both cases the χ^2-algorithm yields higher purities than the ΔR-algorithm.

	1 b-tag	2 b-tags
ΔR-method	$(28.6 \pm 0.1)\%$	$(40.8 \pm 0.2)\%$
χ^2-method	$(34.3 \pm 0.1)\%$	$(47.5 \pm 0.2)\%$

Table 8.2.: Signal purities for the ΔR-method and the χ^2-method in the 1 b-tag and the 2 b-tags case

It should be noted, however, that for a measurement of the top-quark mass it is not just the overall signal purity but also the shape of the combinatorial-background distribution that is important, because the signal and background distributions have to be fitted in order to determine the top-quark mass. Ideally, the signal peak should be located on top of a flat or at least sufficiently smooth (combinatorial) background that can be described by a function that is as simple, i.e. has as few parameters, as possible.

Figures 8.2 and 8.3 show the signal and combinatorial-background distributions for the three mass estimators $m_{3\text{jet}}$, $m_{\text{top, ratio}}$ and $m_{\text{top, angle}}$ in the 1 b-tag and 2 b-tags, respectively. The distributions in the left columns of each figure correspond to the ΔR-method, those in the right columns to the χ^2-method.

The combinatorial-background shapes of $m_{\text{top, ratio}}$ and $m_{\text{top, angle}}$ are very similar to each other but they differ significantly from that of m_{3jet}: Most notably, in the 2 b-tags case, the combinatorial background for m_{3jet} peaks in the signal region (see upper two plots in Figure 8.3). The reason for this behaviour lies in the specific way events are classified as either signal or combinatorial-background events: As described in the previous section, an event for which the right three jets have been assigned to the hadronically-decaying top quark but the wrong two out of these three jets have been chosen to form the W-boson is classified as a combinatorial-background event because the estimators $m_{\text{top, ratio}}$ and $m_{\text{top, angle}}$ rely on the additional reconstruction of the W-boson. However, these events still yield the correct invariant three-jet mass which causes the background distribution to peak in the signal region. This effect is not visible in the 1 b-tag case because the overall number of combinatorial-background events below the signal peak is higher as a result of the less stringent b-tagging constraints.

It should also be noted that the combinatorial background is generally flatter if the reconstruction has been performed using the ΔR-method (left column on both figures) rather than the χ^2-method (right columns): In the latter case, the kinematic constraint that the invariant two-jet mass should be close to the W-boson mass suppresses combinations with larger two-jet masses (see Figure 8.5 in the next section for illustration) and hence also larger top-quark masses, causing the distribution to decay more rapidly towards higher values of the reconstructed top-quark masses.

The main problem with the combinatorial-background distributions presented so far is that, with the exception of the χ^2-method in the 1 b-tag case, they differ considerably between $m_{\text{top, ratio}}$ and $m_{\text{top, angle}}$ on the one hand and m_{3jet} on the other. With regard to fitting the distributions and comparing the different mass estimators and their uncertainties it would, however, be preferable if the distributions could be described with the same set of functions. This can indeed be achieved by the application of so-called cleaning cuts as will be shown in the next section.

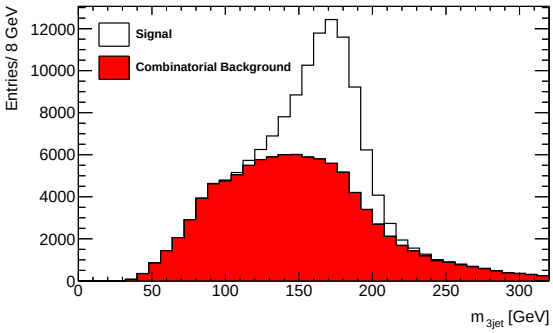

(a) ΔR-method, $m_{3\text{jet}}$

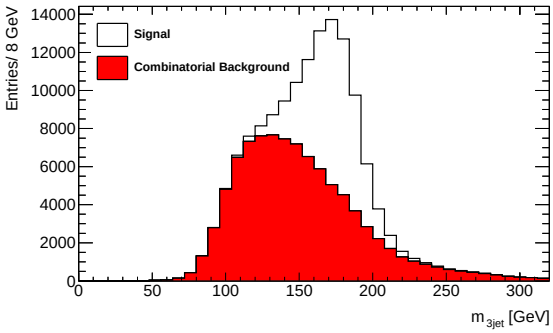

(b) χ^2-method, $m_{3\text{jet}}$

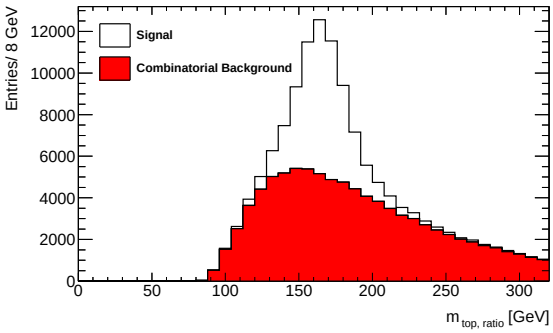

(c) ΔR-method, $m_{\text{top, ratio}}$

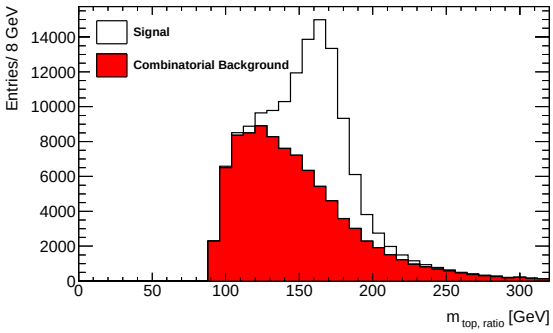

(d) χ^2-method, $m_{\text{top, ratio}}$

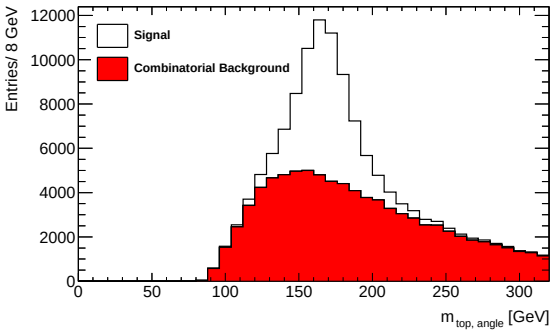

(e) ΔR-method, $m_{\text{top, angle}}$

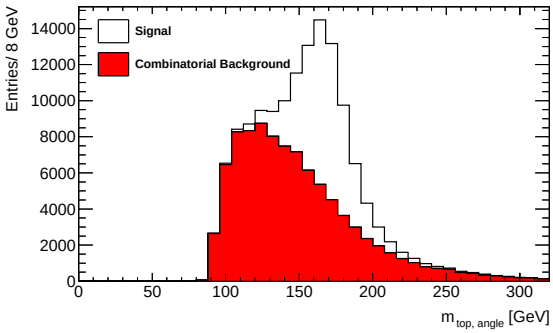

(f) χ^2-method, $m_{\text{top, angle}}$

Figure 8.2.: Signal and combinatorial-background distributions of the three top-mass estimators for events reconstructed with the ΔR-method and the χ^2-method in the 1 b-tag case

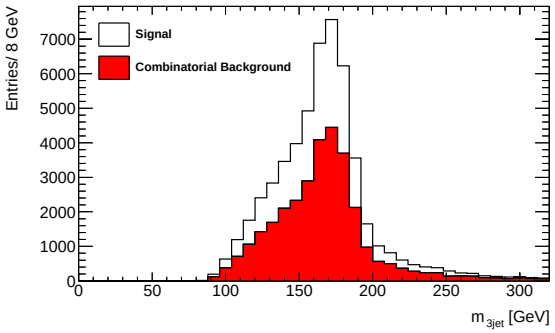

(a) ΔR-method, $m_{3\mathrm{jet}}$

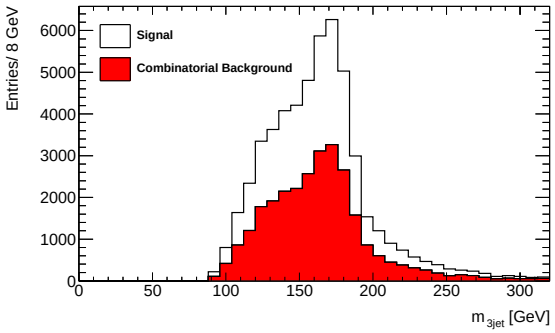

(b) χ^2-method, $m_{3\mathrm{jet}}$

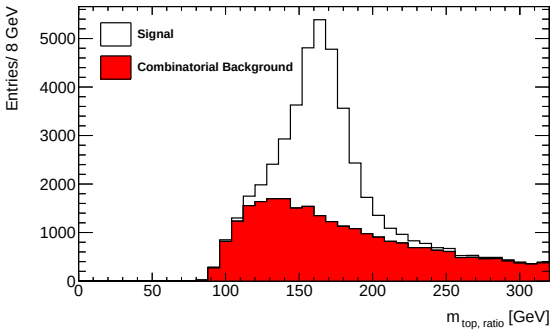

(c) ΔR-method, $m_{\mathrm{top,\ ratio}}$

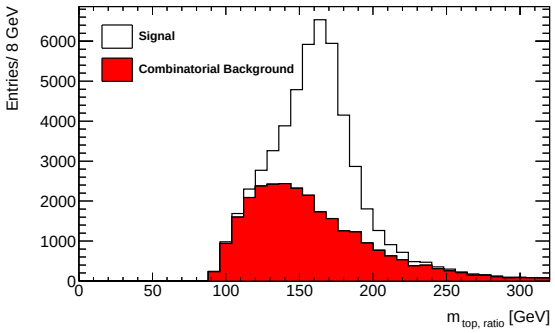

(d) χ^2-method, $m_{\mathrm{top,\ ratio}}$

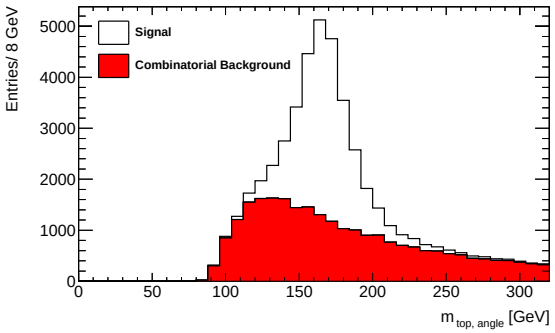

(e) ΔR-method, $m_{\mathrm{top,\ angle}}$

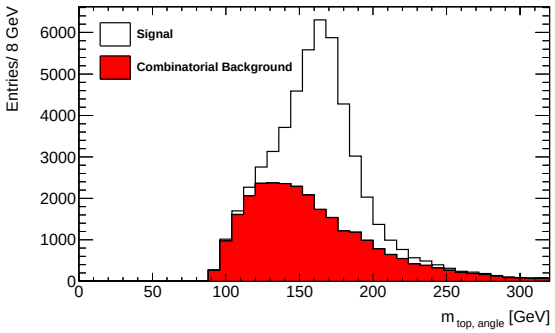

(f) χ^2-method, $m_{\mathrm{top,\ angle}}$

Figure 8.3.: Signal and combinatorial-background distributions of the three top-mass estimators for events reconstructed with the ΔR-method and the χ^2-method in the 2 b-tags case

8.4. Application of Cleaning Cuts

After the reconstruction of the hadronically-decaying top quark further cuts, the so-called **purification** or **cleaning cuts**, can be applied in order to reduce the combinatorial background and thereby increase the signal purity. The cleaning cuts also serve as an important means to influence the shape of the combinatorial background which, as mentioned in the last section, is of particular significance with regard to the necessity of finding appropriate functions to fit the signal and background distributions of the three mass estimators. All these aspects have to be considered when choosing an appropriate set of cuts.

8.4.1. Cleaning Cut 1 (CC1)

Like the reconstruction algorithms, cleaning cuts rely on geometric or kinematic properties of the decay to select correctly reconstructed events and reject those with wrong jet combinations. A commonly used cut, which can be applied in both the 1 b-tag and the 2 b-tags case, aims at rejecting events in which the hadronically-decaying W-boson has not been correctly reconstructed: The invariant-mass distribution of the two light-quark jets, m_{j1+j2}, peaks at the known value for the W-boson mass, i.e. around 80 GeV, if both jets have been chosen correctly. It is customary to keep only events that lie within a mass window defined by twice the width of the distribution around that peak:

- **Cleaning Cut 1 (CC1)**: Require $|m_{j1+j2} - m_{\text{2jet}}^{\text{peak, fit}}| < 2 \cdot \sigma_{\text{2jet}}^{\text{fit}}$.

Both the peak value $m_{\text{2jet}}^{\text{peak, fit}}$ and the width $\sigma_{\text{2jet}}^{\text{fit}}$ are obtained by fitting a Crystal-Ball function[1] to the signal distribution as shown in Figure 8.4 for the 1 b-tag case.

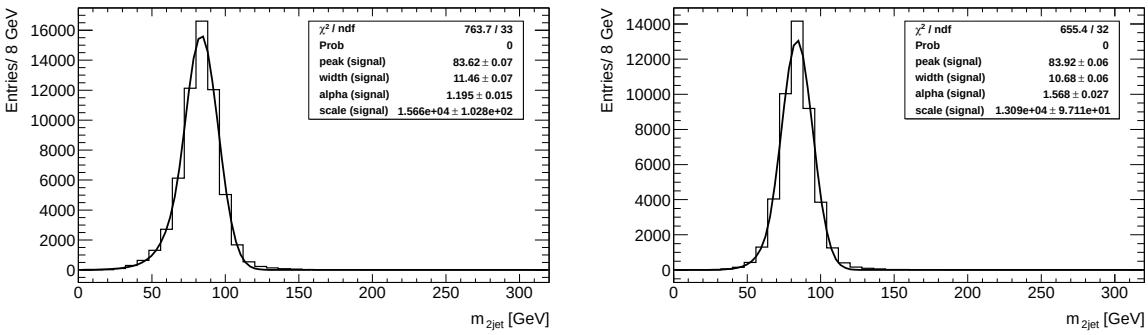

(a) ΔR-method **(b)** χ^2-method

Figure 8.4.: Fit of a crystal-ball function to the 2-jet invariant-mass distributions for correctly reconstructed W-bosons using the ΔR-method (a) and the χ^2-method (b) in the 1 b-tag case

The efficiencies[2] and purities for this cut are summarised in the first two columns of Tables 8.3 and 8.4, both for the ΔR- and the χ^2-method in the 1 b-tag and the 2 b-tags case.

[1] For a discussion of this function see Section 9.1. A formal definition can be found in Appendix B.
[2] The efficiencies are evaluated with respect to the number of events with complete jet-parton matching before and after the respective cut.

	after CC1 (1 b-tag)	**after CC1 (2 b-tags)**	**after (CC1+CC2+CC3) (2 b-tags)**
ΔR-method	$(56.1 \pm 0.1)\%$	$(64.1 \pm 0.2)\%$	$(32.4 \pm 0.2)\%$
χ^2-method	$(93.8 \pm 0.1)\%$	$(90.0 \pm 0.1)\%$	$(40.6 \pm 0.2)\%$

Table 8.3.: Efficiencies of the various cleaning cuts for the ΔR-method and the χ^2-method in the 1 b-tag and the 2 b-tags case

	after CC1 (1 b-tag)	**after CC1 (2 b-tags)**	**after (CC1+CC2+CC3) (2 b-tags)**
ΔR-method	$(46.6 \pm 0.2)\%$	$(57.7 \pm 0.3)\%$	$(79.6 \pm 0.3)\%$
χ^2-method	$(34.7 \pm 0.1)\%$	$(49.0 \pm 0.2)\%$	$(72.7 \pm 0.3)\%$

Table 8.4.: Purities of the various cleaning cuts for ΔR-method and the χ^2-method in the 1 b-tag and the 2 b-tags case

The differences between the two reconstruction methods with respect to this cut are striking: While the signal purites are increased from 28.6% to 46.6.% (1 b-tag) and from 40.8% to 57.7% (2 b-tags) for the ΔR-method, they remain almost the same for the χ^2-method. At the same time, the signal effiencies drop to 56% (1 b-tag) and 64% (2 b-tags) for the ΔR-method, while high signal efficencies of more than 90% are retained for the χ^2-method.

These effects are a direct result of the different approaches to the reconstruction of the W-boson used in the ΔR- and the χ^2-methods, respectively, because they lead to fundamentally different shapes of the combinatorial-background distribution of the cut parameter m_{j1+j2} as illustrated in Figure 8.5.

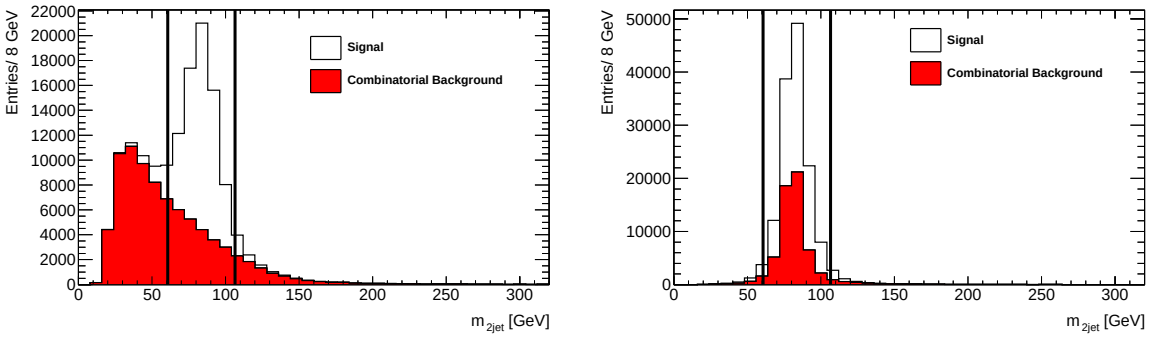

(a) ΔR-method **(b)** χ^2-method

Figure 8.5.: Signal and combinatorial-background distributions for the mass of the reconstructed W-boson in the 1 b-tag case using (a) the ΔR-method and (b) the χ^2-method. The black vertical lines mark the boundaries of the mass window selected by cleaning cut CC1.

In the ΔR-case, the distribution decreases monotonously towards increasing masses, reflecting the fact that jets with low transverse momenta occur more frequently than jets with high transverse

momenta, while in the χ^2-case the combinatorial background peaks at around 80 GeV - just like the signal distribution. This is a direct consequence of the fact that in the latter case the W-boson mass is already used as a kinematic constraint during the reconstruction process, which may result in wrong light-quark jet combinations being chosen because their invariant mass is close to the W-boson mass, thus forcing the combinatorial background into signal shape. Accordingly, the cleaning cut CC1 is not suited to remove much of the combinatorial background in this case, while it effectively rejects wrong jet combinations, in particular those with small invariant masses in the ΔR-case.

The corresponding distributions of signal and combinatorial background are shown in Figure 8.6 for the 1 b-tag case and in Figure 8.7 for the 2 b-tags case.

As expected, the effect of the cleaning cut CC1 on the shape of the combinatorial background is very small for the χ^2-method (see plots in the right columns of Figures 8.6 and 8.7) with the only exception of the m_{3jet}-distribution in the 2 b-tags case, where the cut effectively removes the peak of the combinatorial background below the signal peak.

The most notable conclusion to be drawn from Figures 8.6 and 8.7 is that after the application of cleaning cut CC1, the combinatorial background has a similar shape for all three mass estimators and can therefore potentially be fitted with the same type of function. As discussed in Section 8.3.3, this is due to the fact that the shape differences between the estimators $m_{\text{top, ratio}}$ and $m_{\text{top, angle}}$ on the one hand and m_{3jet} on the other before the cleaning cut are mostly caused by events with incorrectly reconstructed W-bosons which lead to incorrect masses for $m_{\text{top, ratio}}$ and $m_{\text{top, angle}}$ but not necessarily for m_{3jet} as long as the three right jets have been chosen for the hadronically-decaying top quark. Cleaning cut CC1 has been specifically designed to remove events with incorrect two-jet combinations, i.e. exactly those events for which the mass estimators potentially differ.

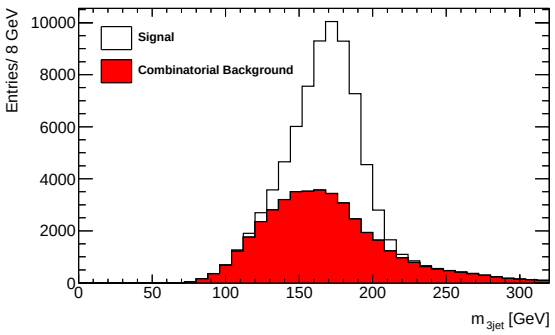

(a) ΔR-method, $m_{3\mathrm{jet}}$

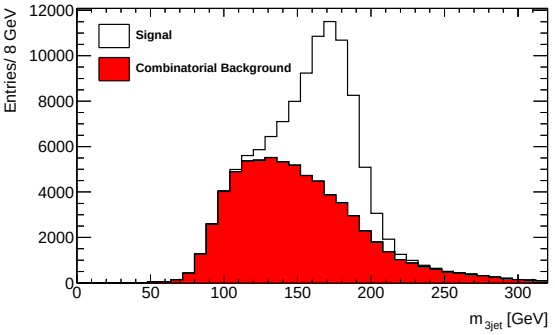

(b) χ^2-method, $m_{3\mathrm{jet}}$

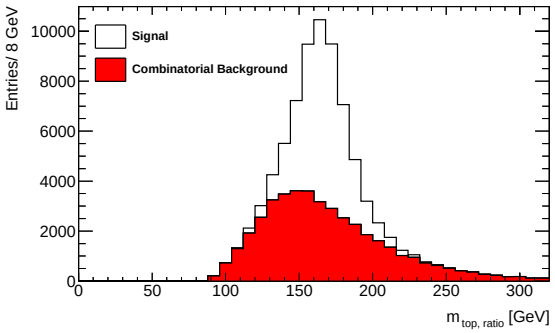

(c) ΔR-method, $m_{\mathrm{top,\ ratio}}$

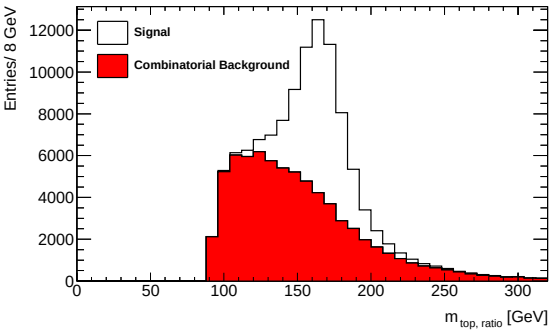

(d) χ^2-method, $m_{\mathrm{top,\ ratio}}$

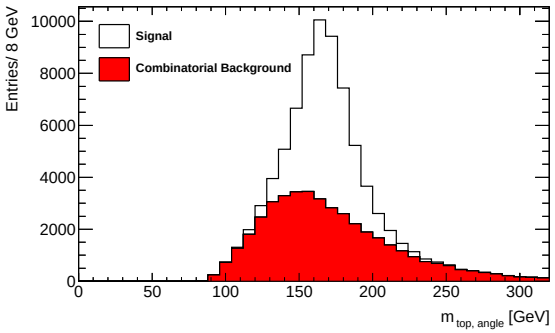

(e) ΔR-method, $m_{\mathrm{top,\ angle}}$

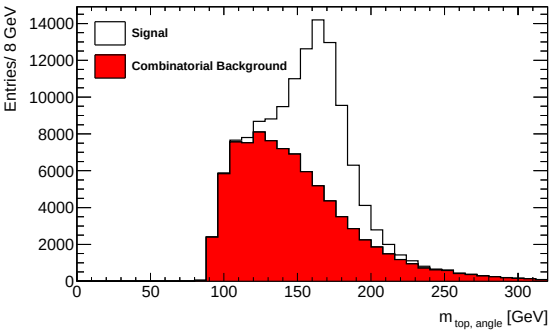

(f) χ^2-method, $m_{\mathrm{top,\ angle}}$

Figure 8.6.: Signal and combinatorial-background distributions after cleaning cut CC1 in the 1 b-tag case

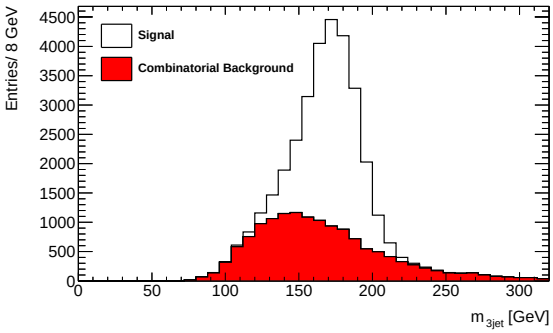

(a) ΔR-method, $m_{3\text{jet}}$

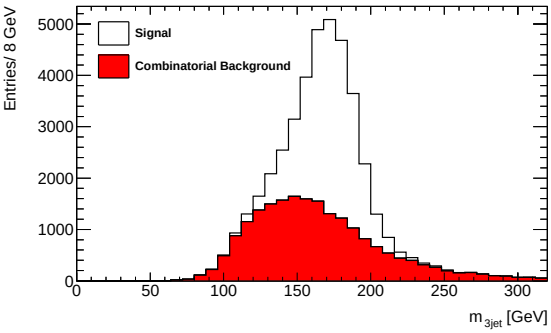

(b) χ^2-method, $m_{3\text{jet}}$

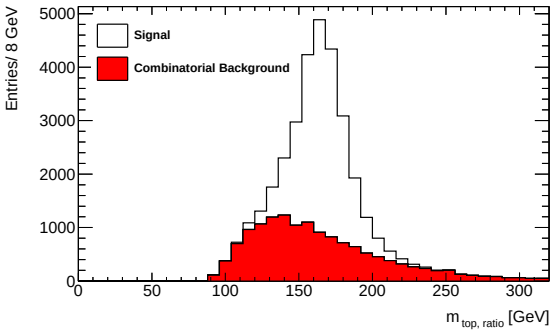

(c) ΔR-method, $m_{\text{top, ratio}}$

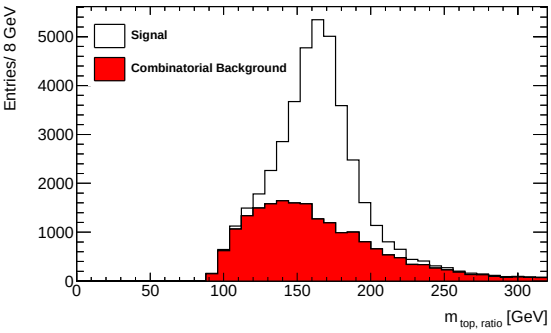

(d) χ^2-method, $m_{\text{top, ratio}}$

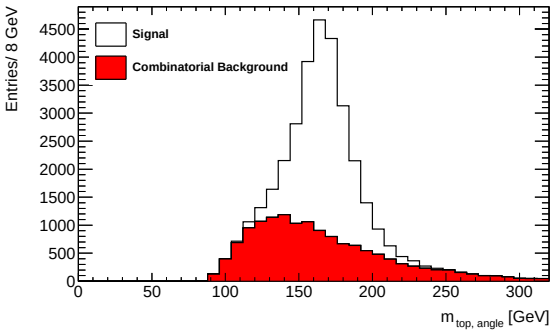

(e) ΔR-method, $m_{\text{top, angle}}$

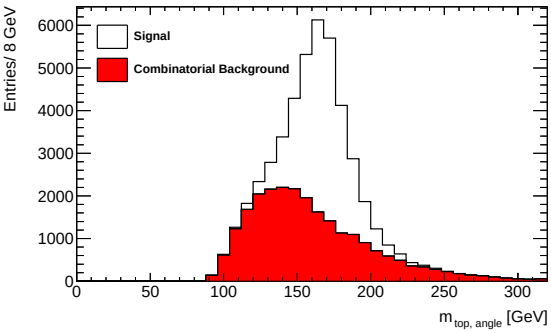

(f) χ^2-method, $m_{\text{top, angle}}$

Figure 8.7.: Signal and combinatorial-background distributions after cleaning cut CC1 in the 2 b-tags case

8.4.2. Cleaning Cut 2 (CC2)

For events with two b-tagged jets where one is used in the reconstruction of the hadronic branch and the other is then automatically identified as the b-jet from the leptonic branch, two more cleaning cuts can be applied. They both aim at removing events where at least one of the two b-jets has been incorrectly reconstructed.

The first additional cleaning cut aims at removing events in which the two b-jets have mistakenly been interchanged. If this is the case, the invariant mass $m_{j1+j2,bl}$ of the (correctly reconstructed) hadronically-decaying W-boson (j1+j2) and what is assumed to be the b-jet from the leptonic branch (bl) should peak at the top-quark mass, i.e. around 170 GeV. Since the top-quark mass is the quantity that is to be measured, it is not possible to directly cut on this parameter. Instead, a threshold value below which all events are rejected is derived from a comparison of the signal and background distributions of $m_{j1+j2,bl}$ as shown in Figure 8.8.

The cleaning cut is accordingly defined as follows:

- **Cleaning Cut 2 (CC2)**: Require $m_{j1+j2,bl} > 200$ GeV.

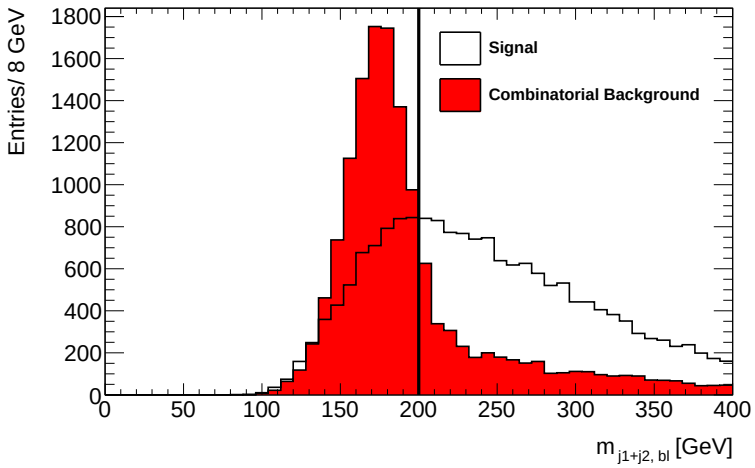

Figure 8.8.: Signal and combinatorial-background distributions for $m_{j1+j2,bl}$. The black line marks the cut value chosen for cleaning cut CC2.

8.4.3. Cleaning Cut 3 (CC3)

Another cleaning cut involving the leptonic branch can be applied. Due to four-momentum conservation, the invariant mass of the sum of the four-vectors of the neutrino, the charged lepton, and the corresponding b-quark jet must equal the top-quark mass. Accordingly, the invariant mass $m_{l,bl}$ of the charged lepton and the b-quark jet (bl) alone has to be below the expected top-quark mass of roughly 170 GeV because the neutrino is not taken into account. The signal and combinatorial-background distributions (Figure 8.9) imply a cut value of 150 GeV on $m_{l,bl}$:

- **Cleaning Cut 3 (CC3)**: Require $m_{l,bl} < 150$ GeV.

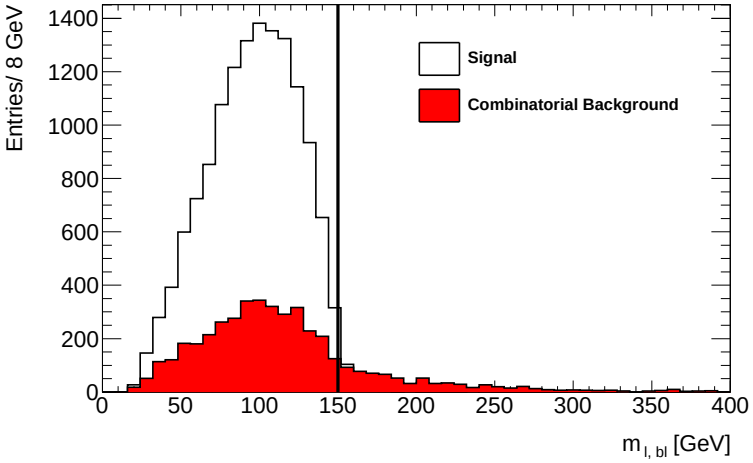

Figure 8.9.: Signal and combinatorial-background distributions for $m_{l,bl}$. The black line marks the cut value chosen for cleaning cut CC3.

8.4.4. Combination of Cleaning Cuts CC1+CC2+CC3 for the 2 B-Tags Case

The combined effect of all cleaning cuts (CC1+CC2+CC3) on the mass distributions for events with exactly 2 b-tags is shown in Figure 8.10, the corresponding efficiencies and purities can be found in the last column of Tables 8.3 and 8.4: The additional cleaning cuts lead to a considerable increase of the signal purity compared to the situation after CC1: For the ΔR-method, it rises from 58% to 80% and for the χ^2-method from 49% to 73%. At the same time, however, the overall efficiency is halved from 64% to 32% for the ΔR-method and from 90% to 40% for the χ^2-method.

Moreover, in all cases, the combinatorial background, though considerably reduced and relatively flat, is now centered below the signal region. This is a consequence of the stricter cuts that are only passed by background events that are sufficiently signal-like and hence are likely to yield masses close to the top-quark mass. These background events are particularly problematic because the larger the curvature of the background below the signal peak, the more difficult it is to exactly determine the peak position. Therefore, looser cleaning cuts should be preferred over stricter ones.

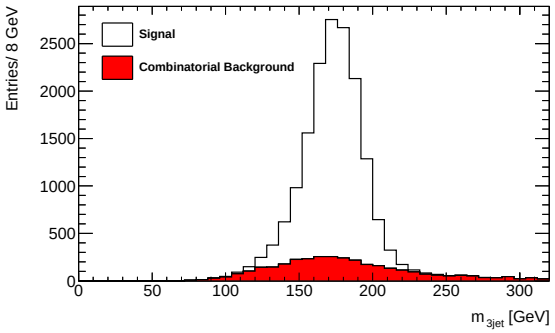

(a) ΔR-method, $m_{3\mathrm{jet}}$

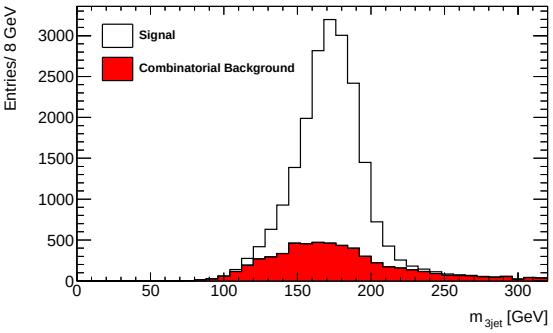

(b) χ^2-method, $m_{3\mathrm{jet}}$

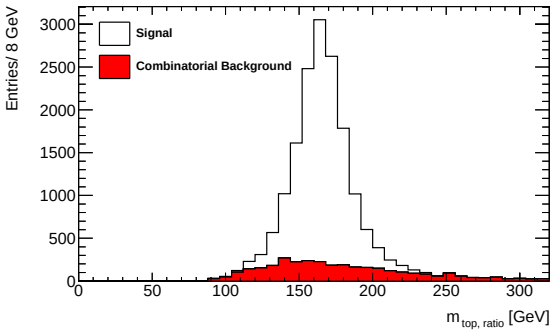

(c) ΔR-method, $m_{\mathrm{top,\ ratio}}$

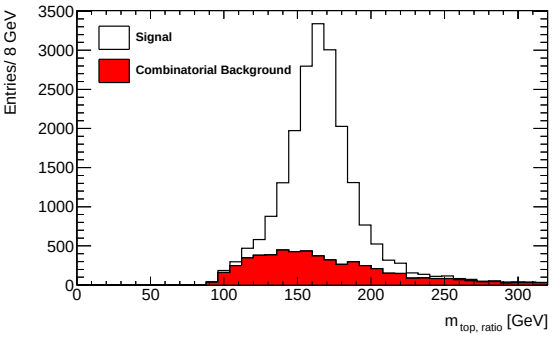

(d) χ^2-method, $m_{\mathrm{top,\ ratio}}$

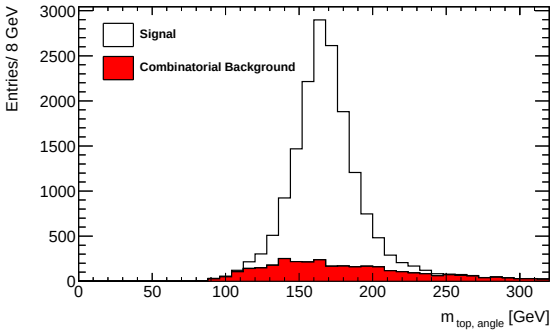

(e) ΔR-method, $m_{\mathrm{top,\ angle}}$

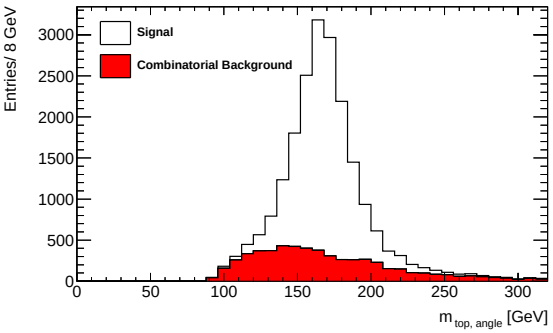

(f) χ^2-method, $m_{\mathrm{top,\ angle}}$

Figure 8.10.: Signal and combinatorial-background distributions after cleaning cuts CC1+CC2+CC3 in the 2 b-tags case

8.5. Final Evaluation of the Reconstruction Methods and Cleaning Cuts

In the previous sections two different reconstruction methods for the hadronically-decaying top quark in semileptonic $t\bar{t}$ events, the ΔR-method and the χ^2-method, have been introduced and compared with respect to different sets of cleaning cuts for both the 1 b-tag and the 2 b-tags case.

The choice of an optimal combination of reconstruction methods and selection/cleaning cuts is subject to various criteria: Firstly, it is desirable to achieve a **high signal purity** while also retaining a sufficiently **high signal efficiency** to provide sufficient statistics in order to keep the statistical uncertainties low. For a measurement of the top-quark mass with different mass estimators, however, the **shape of the combinatorial background** is equally important: The distribution must be smooth and simple enough to be described by a fit function with few parameters and, ideally, it should be flat in the signal region so that small uncertainties in the description of the background do not lead to considerable shifts of the signal peak. Finally, the background distributions for the different mass estimators should preferentially lend themselves to a description with the same type of fit function to allow for a more consistent comparison of the different estimators.

It has been demonstrated in Section 8.4.1 that the latter requirement can only be met if at least cleaning cut CC1 is applied to the samples. The application of further cleaning cuts in the 2 b-tags case leads to higher signal purities but also considerably lower efficiencies as shown in Section 8.4.4. Moreover, the corresponding background distributions, although being relatively flat, are centered below the signal peak which, as explained in Section 8.4.4, might potentially be problematic with regard to the determination of the exact position of the latter.

Therefore, in the following analysis, only cleaning cut CC1 is to be applied to the sample with the ΔR-method as the preferred choice for the reconstruction because it leads to a considerably flatter combinatorial-background distribution compared to the χ^2-method (see Figures 8.6 and 8.7).

As for the choice of selection cuts, the 2 b-tags case is preferred over the case where only one b-tag is required: In the latter case, the distribution of the combinatorial background is steeper and its peak is located at around 150 GeV and hence closer to the signal peak than in the 1 b-tag case where it peaks at roughly 140 GeV (see left columns of Figures 8.6 and 8.7).

Selection cuts	C1 - C16 (2 b-tags)
Reconstruction algorithm	ΔR-method
Cleaning cut	CC1

Table 8.5.: Summary of the selection and reconstruction methods that have been chosen for the following measurement of the top-quark mass

For completeness, it should be noted that with this choice of reconstruction algorithm and cleaning cuts no additional selection cuts to restrict the jet multiplicity in the events are required: As shown in Figure 8.11, a restriction of the jet number to five only leads to an overall loss of statistics (smaller number of entries in Figure 8.11b compared to Figure 8.11a) but no significant improvement of the signal purity, and the shape of the combinatorial background remains essentially the same. The effect is the same if the jet number is restricted to four (not shown here). The loss of statistics in this case is even bigger as is to be expected on the basis of the jet-multiplicity distribution in Figure 8.1.

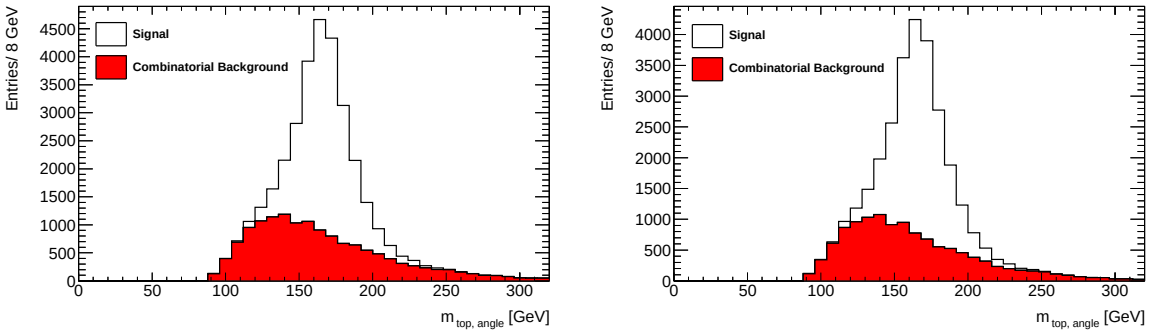

(a) no upper bound on the jet number

(b) ≤ 5 jets

Figure 8.11.: Signal and combinatorial-background distributions for the ΔR-method with cleaning cut CC1 in the 2 b-tags case and different selection cuts on the jet multiplicity

All studies in the previous sections were performed on the subsample of the non-allhadronic signal sample for which a complete jet-parton matching is possible because this allows to study the combinatorial background and the way it is influenced by the reconstruction methods and cleaning cuts. In the final analysis, however, the cleaning cuts are applied to all events that pass the event selection process, i.e. all events that pass selection cuts C15 (1 b-tag case) and C16 (2 b-tags case), respectively. The efficiencies and purities/fractions of the various cleaning cuts with respect to the complete set of signal and background samples are summarised in Tables 8.7 and 8.6 for the ΔR-algorithm.

The cleaning cuts lead to a further slight increase of the overall purity of non-allhadronic events with respect to the various background processes as is to be expected since they introduce additional kinematic constraints such as that on the invariant mass of the W-boson (CC1) which are more likely to be met by semileptonic events. It should also be noted that after the application of one or more cleaning cuts, the single-top background is the dominant background contribution in the 2 b-tags case (see second and third columns in Table 8.6). This is to be expected because the cleaning cuts aim at very specific kinematic properties of the top-quark and W-boson decay which are most likely to be met by events that actually contain a top quark in the final state.

	after CC1 (1 b-tag)	**after CC1 (2 b-tags)**	**after (CC1+CC2+CC3) (2 b-tags)**
$t\bar{t}$ (non-allhadronic)	$(81.9 \pm 0.4)\%$	(93.8 ± 0.4) %	(95.3 ± 0.5) %
single top	$(4.7 \pm 0.2)\%$	(3.4 ± 0.3) %	(3.2 ± 0.4) %
W + jets	$(11.9 \pm 0.3)\%$	(2.4 ± 0.3) %	(1.4 ± 0.3) %
Z + jets	$(1.2 \pm 0.1)\%$	(0.3 ± 0.1) %	(0.2 ± 0.1) %
diboson	$(0.19 \pm 0.04)\%$	$(0.06 \pm 0.04)\%$	-

Table 8.6.: Signal purity and fractions of background events after the cleaning cuts for the ΔR-algorithm in the 1 b-tag and the 2 b-tags case. An empty cell indicates that the respective number is not significant because the statistical uncertainty exceeds the value of the purity.

It should also be noted that the efficiencies with respect to the complete non-allhadronic sample

are lower than the corresponding efficiencies that are evaluated with respect to the subsample with complete jet-parton matching (Table 8.3). This can be explained by the fact that the subsample with complete jet-parton matching constitutes, in a sense, an idealised subset of events because the requirement that the jet-parton matching be complete excludes, for example, events in which not all the jets from the hadronic top-quark decay have been reconstructed. Therefore, a larger fraction of events in this subsample passes the cleaning cuts, thus leading to higher cut efficiencies compared to the complete non-allhadronic sample.

	after CC1 (1 b-tag)	**after CC1 (2 b-tags)**	**after (CC1+CC2+CC3) (2 b-tags)**
$t\bar{t}$ (non-allhadronic)	$(46.6 \pm 0.4)\%$	$(51 \pm 1)\%$	$(25 \pm 1)\%$
single top	$(41.0 \pm 0.1)\%$	$(36 \pm 3)\%$	$(17 \pm 2)\%$
W + jets	$(30 \pm 1)\%$	$(26 \pm 2)\%$	$(7 \pm 1)\%$
Z + jets	$(35 \pm 2)\%$	$(30 \pm 10)\%$	$(9 \pm 5)\%$
diboson	$(32 \pm 5)\%$	$(30 \pm 20)\%$	-

Table 8.7.: Signal and background efficiencies of the cleaning cuts for the ΔR-algorithm in the 1 b-tag and the 2 b-tags case. The efficiencies in the 1 b-tag case are evaluated with respect to the number of events of each sample after selection cut C15, and in the 2 b-tags case with respect to the number of events of each sample after selection cut C16. An empty cell indicates that the respective number is not significant because the statistical uncertainty exceeds the value of the efficiency.

The high purity of the event sample after the application of cleaning cut CC1 is most impressively illustrated by the resulting mass distribution for the estimator $m_{3\text{jet}}$ which is shown in Figure 8.12. The distribution corresponds to the set of selection and reconstruction methods summarised in Table 8.5 which is to be used throughout the following analysis.[3]

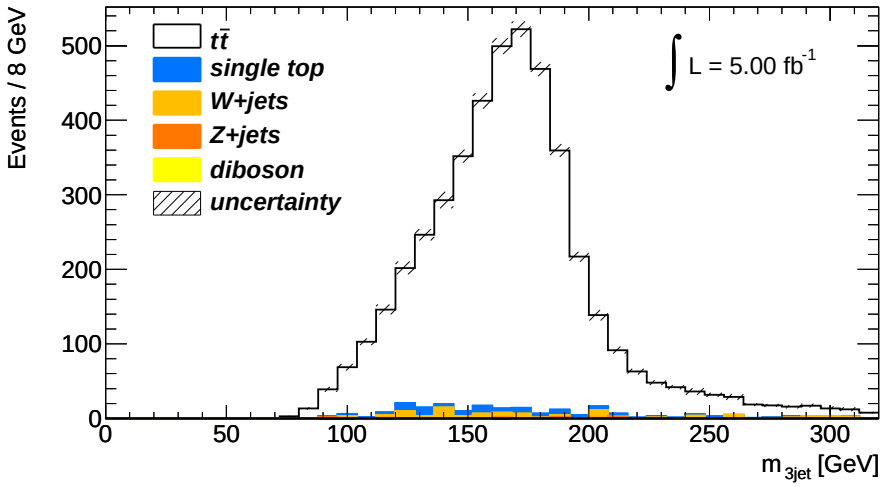

Figure 8.12.: Distribution of $m_{3\text{jet}}$ for the complete non-allhadronic $t\bar{t}$ and the physical background samples after cleaning cut CC1 in the 2 b-tags case

[3]The only exception is the $\beta\gamma$ method introduced in Section 9.4.

9. Comparison of the Mass Estimators

In the following chapter, the three estimators for the top-quark mass introduced in Section 7 are compared with particular regard to their JES and bJES dependence. To this end, the respective distributions are fitted with an appropriate set of functions to determine the position of the mass peak for each estimator. The details of the **fit** are explained in Section 9.1. The effect of a **variation** of the **jet-energy scale** and the **b-jet energy scale** on the fitted peak values is studied in Sections 9.2.1 and 9.2.2, respectively. The results are used to determine the corresponding **systematic uncertainties** on the different mass estimators. It turns out that the exact choice of the cut on the invariant mass of the W-boson (cleaning cut CC1, see Section 8.4) has a considerable impact on the JES and bJES dependence of the estimators. This effect is studied in Section 9.2.3. In Section 9.3, the **calibration curves** for the three mass estimators are presented. Finally, a method to **further reduce the JES dependence of the improved estimators** $m_{\text{top, ratio}}$ and $m_{\text{top, angle}}$ is introduced in Section 9.4.

All studies presented in this chapter, except for those in Section 9.4, are performed on the full set of signal and background samples and all distributions are normalised to an integrated luminosity of 5 fb^{-1} unless stated otherwise.

9.1. Fitting the Mass Distributions

To determine the exact position of the mass peak for each estimator, it is necessary to choose appropriate functions to describe the signal as well as the combinatorial- and physical-background distributions. Ideally, these functions should be as simple as possible, meaning that they should contain only a small number of parameters that are varied during the fitting procedure. This renders the fit more stable[1] under variations of the JES and bJES as well as under variations of the input value for the top-quark mass that is used in the Monte-Carlo generator.

All fits presented in this chapter are performed using the χ^2-minimisation algorithm implemented in the MINUIT [61] package within the ROOT [62] framework.

The studies of the signal and combinatorial-background shape carried out in the previous chapter on the subsample with complete jet-parton matching are a suitable starting point for choosing a fit function for the mass distribution shown in Figure 8.12[2] because they provide an opportunity for testing different fit functions separately on the signal and background distributions. These functions are then added to yield the fit function for the complete mass distribution. In the following, this procedure is demonstrated in detail for the distribution of $m_{3\text{jet}}$. The results obtained thereby can be directly applied to $m_{\text{top, ratio}}$ and $m_{\text{top, angle}}$ because, as explained in the previous section, the application of cleaning cut CC1 on the events reconstructed with the ΔR-method in the 2 b-tags case results in similarly shaped signal and combinatorial-background distributions for all mass estimators.

[1] A fit is regarded as stable if the parameters of the fit function vary continuously under a variation of the parameters that determine the shape of the distributions such as, for example, the generator value of the top-quark mass.

[2] This applies similarly to the corresponding distributions of $m_{\text{top, ratio}}$ and $m_{\text{top, angle}}$.

The common choice of a fit function for the **signal peak** of a mass distribution is a Gaussian function which can be described by a mere three parameters: its mean/peak position, its width and its scale. However, as illustrated in Figure 9.1a, this simple function does not describe the signal distribution satisfactorily: particularly in the lower mass regime there is an excess of events that is not described by the fit function, and the function peak seems to slightly underestimate the true peak value. This excess of events at the lower end of the distribution may be attributed to final-state radiation[3] which has a lowering effect on the momenta of the decay products from which the top quark is reconstructed, thus leading to an underestimation of the top-quark mass.

A much better fit result is obtained by restricting the fit range to values above 120 GeV and choosing a Crystal Ball function as a fit function. This is illustrated in Figure 9.1b. The Crystal Ball function is essentially a modified Gaussian function with an exponential correction factor below or above a certain value of the parameter α. The shape of this function is described by five parameters, one of which is kept fixed during the fit.[4] For positive values of α, the exponential correction factor is applied to the lower tail of the Gaussian which allows for a much better description of the excess of events in this region and also yields a better result for the peak position. It should be noted that neither a fit with a Gaussian function in a restricted fit range nor the choice of a Crystal Ball function for the complete range yield comparably precise fits.

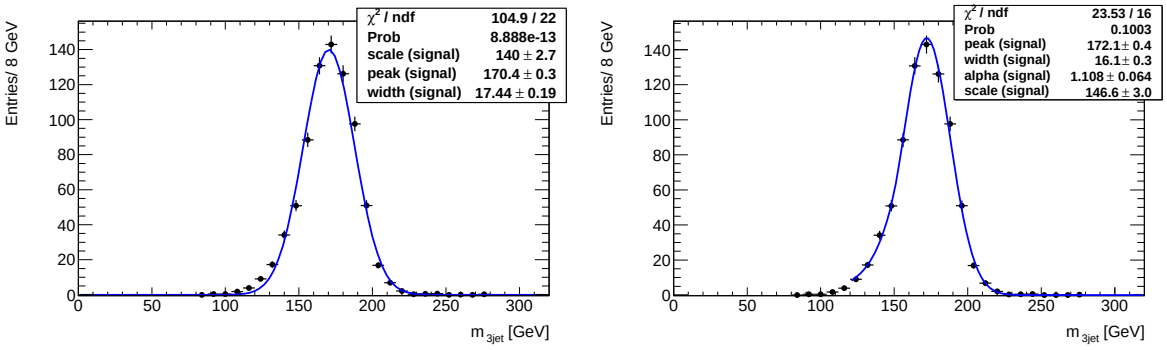

(a) Gaussian fit function

(b) Crystal Ball fit function

Figure 9.1.: Fit of the signal distribution of $m_{3\text{jet}}$ using a Gaussian function over the complete mass range (a) and a Crystal Ball function with lower cut-off at 120 GeV (b)

The preferred choice for the fit of the **combinatorial background** distribution would be a Landau function because it has only three parameters. As shown in Figure 9.2a, this function fits the distribution very poorly, in particular in the region below the signal peak (between roughly 130 GeV and 200 GeV) where a precise description of the background is essential. It turns out that again a Crystal Ball function, this time with a considerably larger width and a negative value of α, describes the combinatorial background very well if the fit range is restricted to mass values above 120 GeV.

It should be noted that the choice of the fit range and function of the combinatorial-background distribution is primarily dictated by the requirement that the fit function describes the shape of the background in the signal region as precisely and with as few parameters as possible. There are, a priori, no preditions for the functional shape of the background based on physical models. As shown in the previous chapter, this shape is primarily influenced by the choice of the reconstruction method and the cleaning cuts.

[3] This may be hadronic final-state radiation, for example of gluons radiated off either of the three quarks from the top-quark decay, or electromagnetic radiation off the W-boson.
[4] For details see Appendix B.

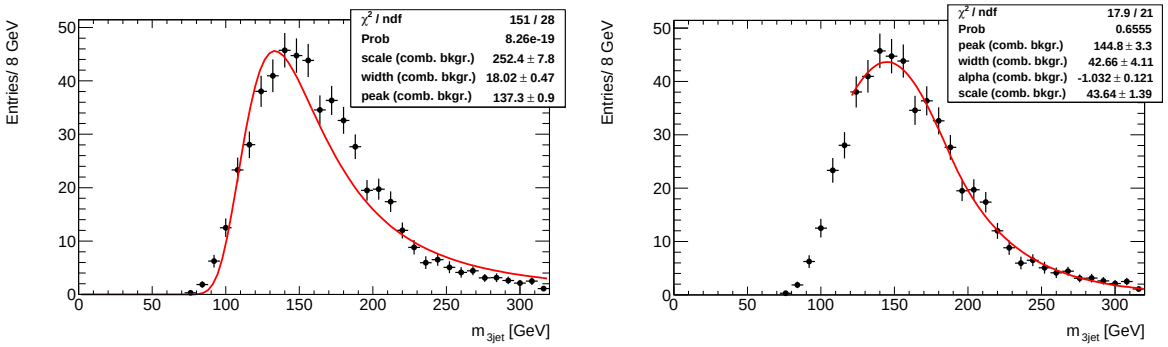

(a) Landau fit function **(b)** Crystal Ball fit function

Figure 9.2.: Fit of the combinatorial-background distribution of $m_{3\text{jet}}$ using a Landau function over the complete mass range (a) and a Crystal Ball function with lower cut-off at 120 GeV (b)

The sum of the two Crystal Ball functions is then used to fit the **stacked distribution** of the signal and combinatorial-background events in the **subsample with complete jet-parton matching**. This is shown in Figure 9.3a. When fitting a signal and a background distribution with the same type of function, it is important to make sure that the fit function for the background distribution does not propagate into the signal region, i.e. does not describe part of the signal distribution, because this would lead to a wrong result for the fitted value of the signal peak. A way to avoid this is to use the parameter values obtained from the separate fits of the two distributions as starting values for the fit of the stacked distribution. Moreover, the input values, in particular those of the width and the parameter α, differ significantly between the two functions. A comparison of Figure 9.3 with Figures 9.1b and 9.2 shows that the shape of the fit function and in particular the position of the peaks do not change significantly during the combined fit.

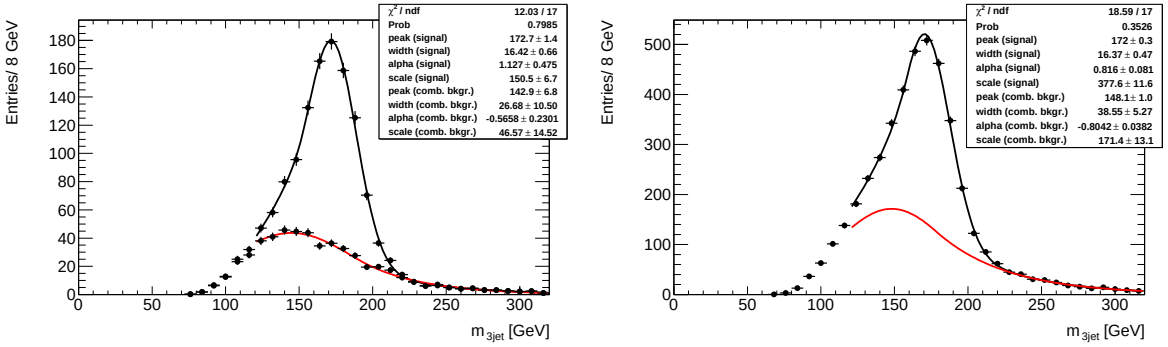

(a) Subsample with complete jet-parton matching **(b)** Complete non-allhadronic $t\bar{t}$ sample

Figure 9.3.: Fit of (a) the stacked signal and combinatorial background distributions on the subsample with complete jet-parton matching and (b) the complete non-allhadronic $t\bar{t}$ signal sample; in both cases the fit function is the sum of the two Crystal Ball functions and the parameters obtained from the separate fits to the signal and combinatorial background distribution are taken as an input to the combined fit

Next, the sum of the two Crystal Ball functions is used to fit the invariant-mass distribution for the **complete non-allhadronic t$\bar{\text{t}}$ sample**, see Figure 9.3b. The parameter values obtained from the fit to the stacked distributions for the subsample with complete jet-parton matching are used

as input values in this fit and it turns out that here again the peak values of the two functions do not deviate significantly from those of the individual fits. This is remarkable because, as discussed in Section 8.2, the subsample on which the shape of the signal and combinatorial-background distributions are studied comprises only about 20% of the complete non-allhadronic sample (see Table 8.1). Moreover, this subsample by definition contains only events for which all jets from the hadronic top-quark decay have been reconstructed. It can therefore be regarded as an idealised subsample of the complete non-allhadronic $t\bar{t}$ sample. This fact is reflected in the slight increase in the width and the relative height of the Crystal Ball function that models the combinatorial background in Figure 9.3b compared to that in Figure 9.3a.[5]

Finally, the mass distribution for the **physical background**[6] is fitted with a Landau function (Figure 9.4a) and the parameters from this fit as well as those from the fit of the complete non-allhadronic signal sample are used as input values in the fit of the **complete mass distribution** with a sum of two Crystal Ball functions and a Landau function (Figure 9.4b). A comparison of

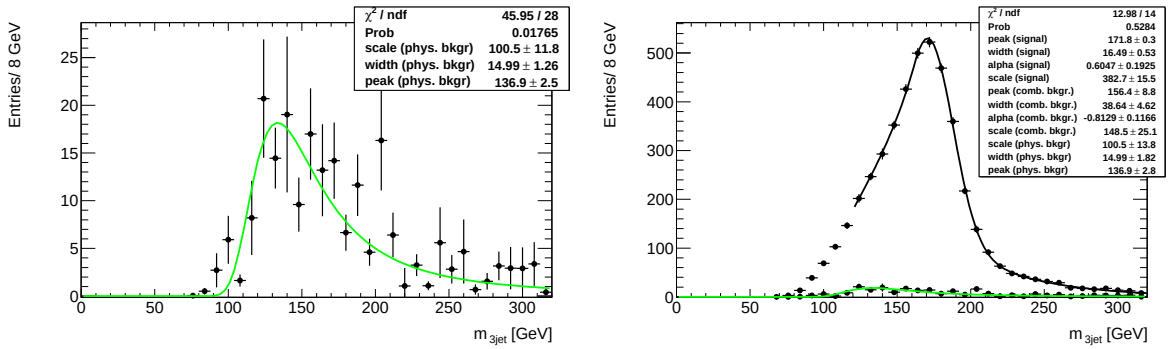

(a) Physical background **(b)** Fit of the complete distribution

Figure 9.4.: Fit of the physical background with a Landau function (a) and fit of the complete mass distribution (non-allhadronic signal and physical-background samples) with a sum of two Crystal Ball functions and a Landau function (b). The distribution on the right-hand side is identical to the one in Figure 8.12.

Figure 9.4b and Figure 9.1b shows that despite the fact that the fit to the complete distribution involves the variation of eleven free parameters, the fitted values for the top-quark mass peak do not differ significantly between the simple case where only the signal distribution is fitted ($m_{\text{top}}^{\text{peak}} = 172.1 \pm 0.4$ GeV) and the fit of the complete mass distribution ($m_{\text{top}}{}^{\text{peak}} = 171.8 \pm 0.3$ GeV) if the fitting procedure is carried out as described above with the parameters from previous fits being used as input parameters in the following fit.

The same fitting procedure is applied to the mass distributions for the estimators $m_{\text{top, ratio}}$ and $m_{\text{top, angle}}$. The results are shown in Figure 9.5b and Figure 9.6b. In addition, the results for the fit of the stacked signal and combinatorial-background distributions are given in Figure 9.5a and Figure 9.6a in order to illustrate that the combinatorial background is well-described in both cases.

[5] Due to the relatively large errors on these parameters in the latter case, however, this increase is not significant.
[6] The physical background distribution is the stacked distribution of all physical background samples used in this analysis (see Section 6.1).

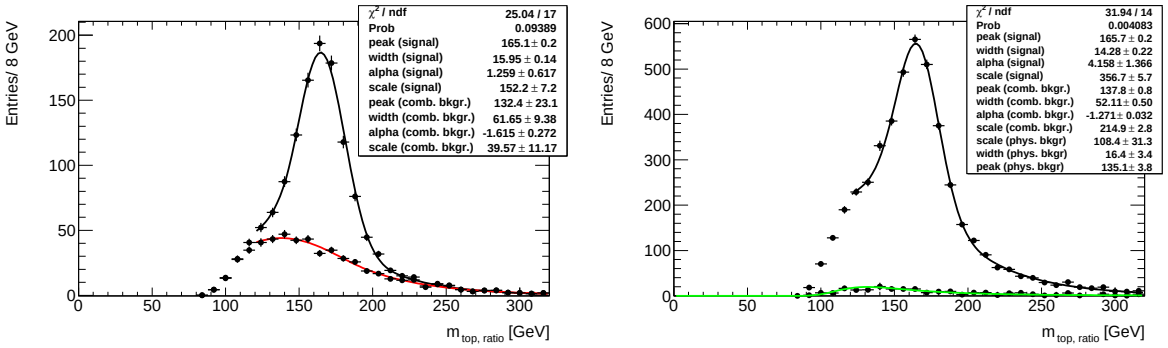

(a) Fit of the subsample with complete jet-parton matching **(b)** Fit of the complete distribution

Figure 9.5.: Fit of the stacked signal and combinatorial background distributions on the subsample with complete jet-parton matching using a sum of two Crystal Ball functions (a) and of the complete mass distribution (complete non-allhadronic signal and physical-background samples) with a sum of two Crystal Ball functions and a Landau function (b)

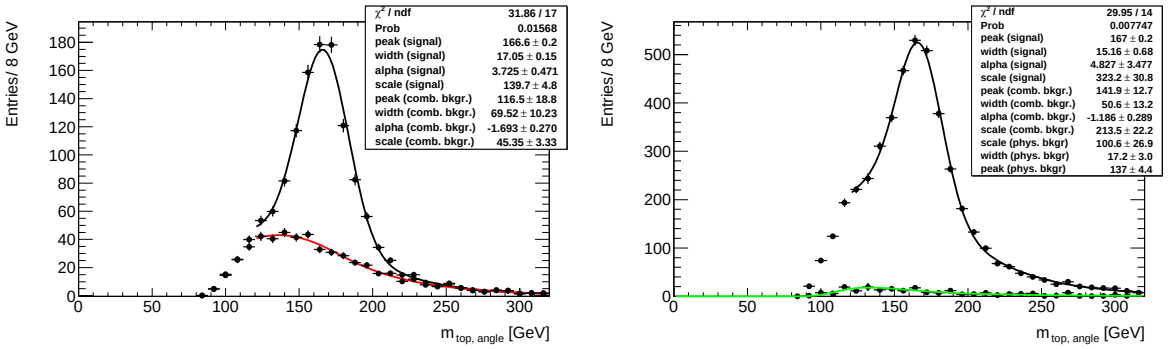

(a) Fit of the subsample with complete jet-parton matching **(b)** Fit of the complete distribution

Figure 9.6.: Fit of the stacked signal and combinatorial background distributions on the subsample with complete jet-parton matching using a sum of two Crystal Ball functions (a) and of the complete mass distribution (complete non-allhadronic signal and physical-background samples) with a sum of two Crystal Ball functions and a Landau function (b)

The fitted peak values for the three mass estimators and their statistical errors are summarised in Table 9.6. The uncertainties on the peak values for $m_{\text{top, ratio}}$ and $m_{\text{top, angle}}$ have been re-scaled by a factor

$$S = \sqrt{\frac{\chi^2}{\text{ndf} - 1}}$$

in accordance with the recommendations of the Particle Data Group [3] for χ^2-fits where the value of χ^2 divided by the number of the degrees of freedom (ndf) is larger but not significantly larger than one. This is the case for the two improved mass estimators (see Figure 9.5b and Figure 9.6b).

$\boldsymbol{m}_{\text{3jet}}$	(171.8 ± 0.3) GeV
$\boldsymbol{m}_{\text{top, ratio}}$	(165.7 ± 0.3) GeV
$\boldsymbol{m}_{\text{top, angle}}$	(167.0 ± 0.3) GeV

Table 9.1.: Overview of the fitted values of the top-quark mass peak and their statistical errors for the three mass estimators

All of these values for the reconstructed top-quark masses deviate from the simulated value of 172.5 GeV of the Monte-Carlo samples. This may have various reasons such as an incorrectly calibrated JES or bJES (see also the next two sections for details) or biases introduced by the selection process, the event reconstruction or the fit. The small values of the reconstructed masses for the two estimators $m_{\text{top, ratio}}$ and $m_{\text{top, angle}}$, which both rely on a measurement of the ratio $m_{\text{top, ratio/angle}}/m_{\text{W}}^{\text{PDG}}$, may, for example, be traced back to an over-estimation of the W-boson mass as illustrated in Figure 8.4: The fitted peak value $m_{\text{2jet}}^{\text{fit, peak}} \approx 83$ GeV deviates from that of $m_{\text{W}}^{\text{PDG}} = 80.4$ GeV by almost 3 GeV.[7]

To account for these effects and obtain the true top-quark mass $m_{\text{top, truth}}$ from the reconstructed masses $m_{\text{top, reco}}$, a calibration curve for each estimator is derived by reconstructing the top-quark mass for different simulated masses. For further details see Section 9.3.

Finally, it should be noted that the introduction of a lower limit for the fit range, the choice of which is to a certain extent arbitrary, yields an additional source of systematic uncertainty. The latter can be assessed by varying the cut-off value by ± 10 GeV. It turns out that the systematic uncertainties for the different estimators related to the choice of the lower cut-off value are below 0.5 GeV and therefore in the order of the statistical uncertainties.

[7] This shift may be a result of the specific choice of jet algorithm: The anti-k_T algorithm with parameter $R = 0.4$ introduces a minimum distance which leads to a suppression of smaller reconstructed two-jet masses.

9.2. Evaluation of the Systematic Uncertainties

In this section, the JES and bJES dependences of the three mass estimators are studied. The results are used to determine the respective systematic uncertainties on the top-quark mass under the assumption of a JES uncertainty of 5% and a bJES uncertainty of 2.5%.

9.2.1. JES Dependence

In order to compare the three mass estimators with respect to their JES dependence, a global JES factor j is applied to the energies and momenta of **all jets** (including the b-quark jets) in the event[8] according to Equation 7.2. This factor can be used to vary the energies and momenta of the jets in the range of $\pm 10\%$ in steps of 5%. The reconstructed top-quark masses $m_{\text{top, reco}}$ for the three estimators m_{3jet}, $m_{\text{top, ratio}}$ and $m_{\text{top, angle}}$ are plotted against the values of the JES factor j (Figure 9.7a-c).

The reconstructed top-quark masses for each estimator can be fitted with a linear function, the slope p1 of which is used to determine the corresponding systematic uncertainty for a given JES uncertainty as follows: According to the selection criteria for jets presented in Section 6.2, all jets used in this analysis have a transverse energy $E_T > 25$ GeV and a pseudorapidity $|\eta| < 2.5$. Based on the current values for the JES uncertainty listed in Table 5.1, a maximum JES uncertainty of 5% is assumed. The corresponding systematic uncertainty on the top-quark mass is then taken to be the variation $\Delta m^{\text{JES}}_{\text{top, reco}}$ of the reconstructed mass $m_{\text{top, reco}}$ over a JES interval of width 0.05:

$$\Delta m^{\text{JES}}_{\text{top, reco}} = 0.05 \cdot \text{p1}.$$

The resulting systematic uncertainties for the different mass estimators obtained from Figure 9.7 are listed in Table 9.2. The errors are obtained by scaling the errors on the slope by 0.05.

$\boldsymbol{\Delta m^{\text{JES}}_{\text{3jet}}}$	(7.7 ± 0.1) GeV
$\boldsymbol{\Delta m^{\text{JES}}_{\text{top, ratio}}}$	(0.8 ± 0.1) GeV
$\boldsymbol{\Delta m^{\text{JES}}_{\text{top, angle}}}$	(0.8 ± 0.1) GeV

Table 9.2.: Systematic uncertainties and their errors for the three mass estimators assuming a global uncertainty of 5% on the JES

The differences in the systematic uncertainties for the three mass estimators are striking: The replacement of the simple estimator m_{3jet} by either of the improved mass estimators $m_{\text{top, ratio}}$ or $m_{\text{top, angle}}$ leads to a reduction of the systematic uncertainty from 7.7 GeV to a mere 0.8 GeV. Hence the improved estimators, which have been specifically designed with the aim of reducing the JES dependence of the top-quark mass (see Section 7 for details), do indeed yield a significant reduction of the systematic uncertainty related to a global JES factor.

The model used to derive these systematic uncertainties on the top-quark mass is, of course, a simplified one because it relies on the assumption of global, i.e. p_T- and η-independent, JES factors with global uncertainties for all jets. As explained in Section 5.4.4, the JES factors to be applied to the measured jet energies, however, depend on the transverse momentum and the pseudorapidity of each jet. The same applies to the uncertainties on these local JES factors. The p_T-

[8] This is done before the event selection in order to take into account the slight changes in the efficiencies of the selection cuts, in particular those on the transverse momenta of the jets.

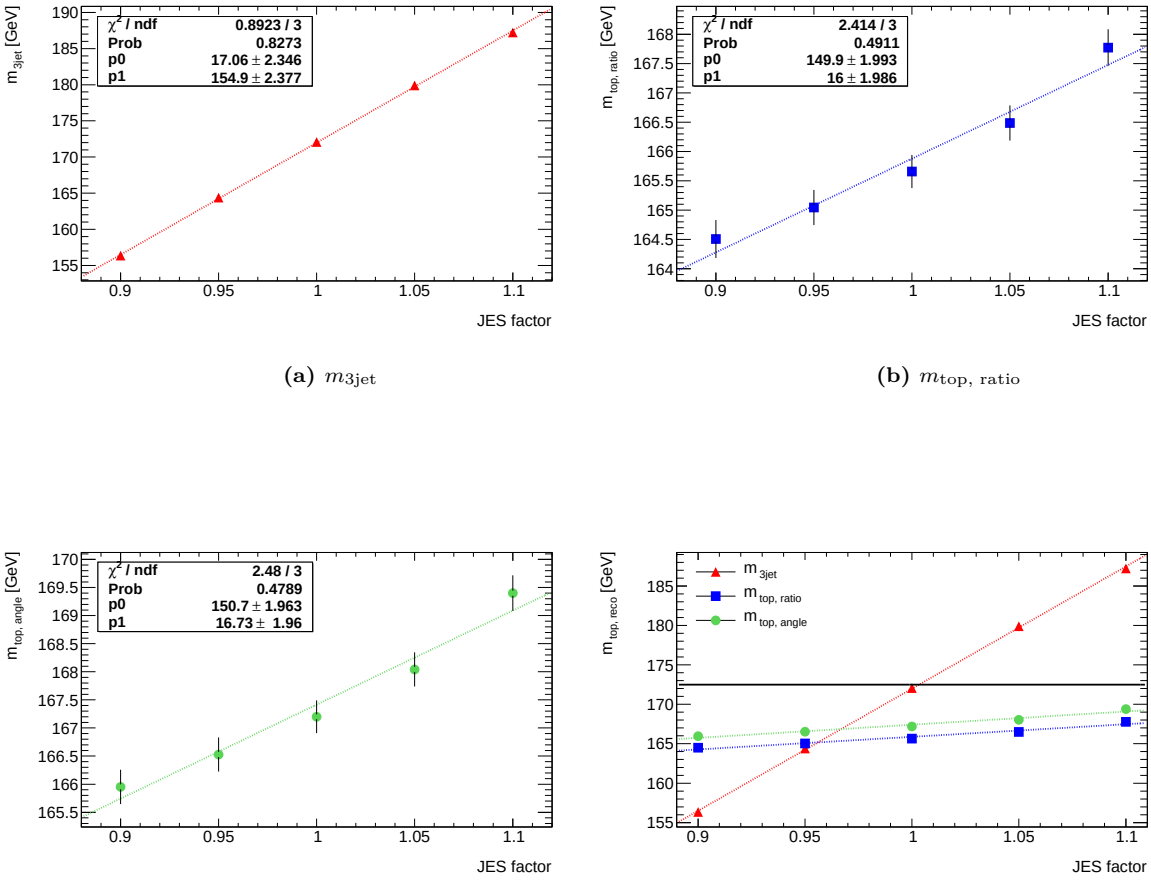

(a) $m_{3\text{jet}}$ **(b)** $m_{\text{top, ratio}}$

(c) $m_{\text{top, angle}}$ **(d)** Comparison of the estimators

Figure 9.7.: JES dependence of the three mass estimators; the reconstructed masses $m_{\text{top, reco}}$ are plotted against the global JES factor and a linear function is used to fit the mass points (a - c); (d) is a combination of the three subplots that serves to illustrate the remarkable differences in the JES dependence of the three mass estimators. The black horizontal line marks the generator mass $m_{\text{top, truth}} = 172.5$ GeV.

and η-dependence of the JES factors has already been taken into account during the reconstruction of the jets in the context of the full detector simulation which is part of the Monte-Carlo samples used in this analysis. In the context of this refined model, the systematic uncertainties on the top-quark mass would then need to be derived from the local JES uncertainties for each jet via error propagation. The same applies to the bJES-related uncertainties discussed in the following section.

9.2.2. bJES Dependence

The bJES dependence of the three mass estimators is evaluated in complete analogy to the JES dependence in the previous section. This time, the Monte-Carlo truth information about the jet flavour is used to apply a scaling factor j_b to all (true) b-quark jets in the events before the selection process. The scaling factor j_b is chosen to model the **additional** uncertainty on the energy of b-quark jets (see Section 5.4.4 for details). In the simplified model with global scaling factors used throughout this thesis, the measured energies and momenta of u-, d-, s-, c-quark jets are re-scaled with the factor j only,

$$E_{u,d,s,c} \longrightarrow j \cdot E_{u,d,s,c},$$

while the energies and momenta of b-quark jets are re-scaled with both j and j_b,

$$E_b \longrightarrow j \cdot j_b \cdot E_b,$$

i.e. j_b is taken to be an additional (smaller) correction factor for b-quark jets.

To study the bJES dependence of the different estimators, j_b is varied in a range of $\pm 5\%$ in steps of 2.5% while j is kept at a constant value of 1. The functional dependence of $m_{\text{top, reco}}$ on the bJES factor j_b is illustrated in Figure 9.8.

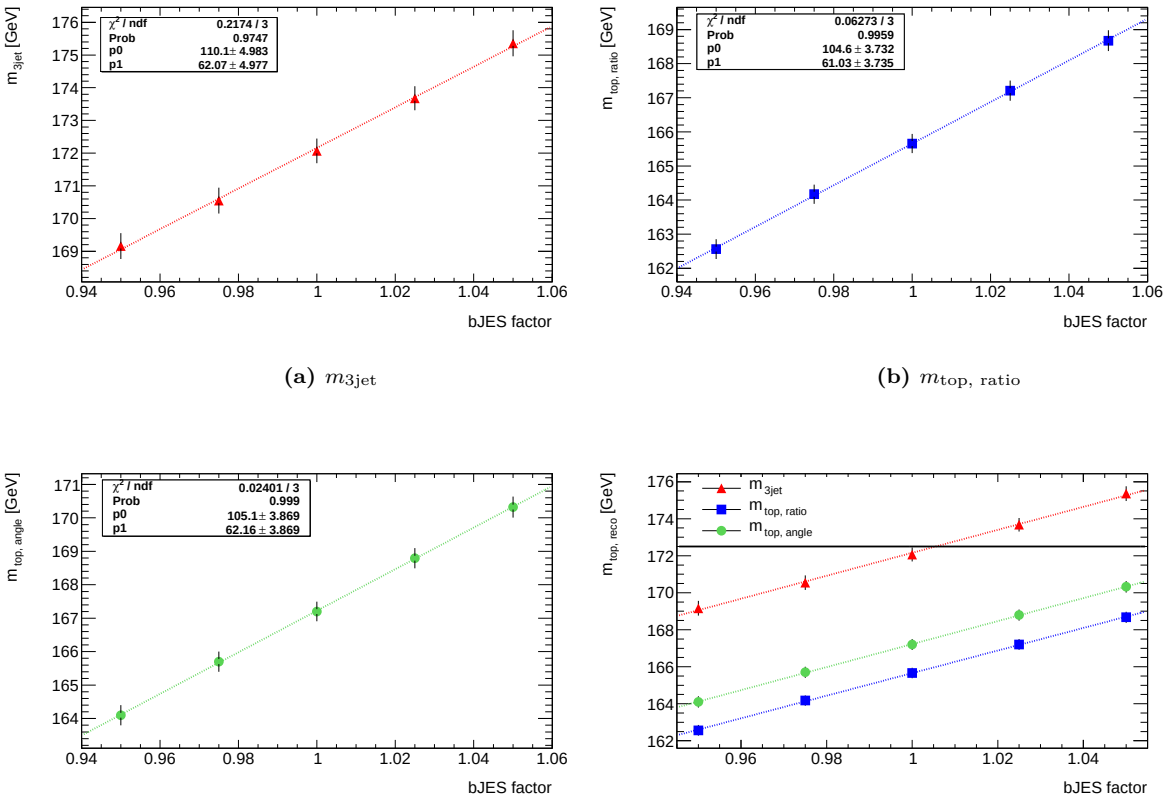

(a) $m_{3\text{jet}}$ **(b)** $m_{\text{top, ratio}}$

(c) $m_{\text{top, angle}}$ **(d)** Comparison of the estimators

Figure 9.8.: bJES dependence of the three mass estimators; the reconstructed masses $m_{\text{top, reco}}$ are plotted against the global bJES factor and a linear function is used to fit the mass points (a - c); (d) is a combination of the three subplots (a - c) to allow for a better comparison of the estimators. The black horizontal line marks the generator mass $m_{\text{top, truth}} = 172.5$ GeV.

The corresponding systematic uncertainties on the top-quark mass are evaluated under the assumption of a bJES uncertainty of 2.5% (based on the values stated in Table 5.2). Their values are summarised in Table 9.3.

$\boldsymbol{\Delta m_{\text{3jet}}^{\text{bJES}}}$	(1.6 ± 0.1) GeV
$\boldsymbol{\Delta m_{\text{top, ratio}}^{\text{bJES}}}$	(1.5 ± 0.1) GeV
$\boldsymbol{\Delta m_{\text{top, angle}}^{\text{bJES}}}$	(1.6 ± 0.1) GeV

Table 9.3.: Systematic uncertainties and their errors for the three mass estimators assuming a global uncertainty of 2.5% on the bJES

All three mass estimators show a comparable bJES dependence. In the case of the mass estimators m_{3jet} and $m_{\text{top, ratio}}$, this can straight-forwardly be explained by a comparison of Equations (7.1) and (7.5). The estimators differ only by a factor $\frac{m_W^{PDG}}{m_{\text{2jet}}}$ which does not depend on the bJES. In other words, if the energies and momenta of all b-jets are re-scaled by $j \cdot j_b$ and by a factor of j in the case of all other jets, the JES factors j in the numerator and the denominator of $\frac{m_{\text{3jet}}}{m_{\text{2jet}}}$ cancel out whereas the bJES factors do not because they only appear in the numerator:

$$\frac{m_{\text{3jet}}}{m_{\text{2jet}}} = \frac{\sqrt{\left(\sum_{jet=1}^{2} E_{jet} + E_{bjet}\right)^2 - \left(\sum_{jet=1}^{2} \vec{p}_{jet} + \vec{p}_{bjet}\right)^2}}{\sqrt{\left(\sum_{jet=1}^{2} E_{jet}\right)^2 - \left(\sum_{jet=1}^{2} \vec{p}_{jet}\right)^2}}$$

$$\xrightarrow{j \cdot j_b} \frac{\sqrt{\left(\sum_{jet=1}^{2} j \cdot E_{jet} + j \cdot j_b \cdot E_{bjet}\right)^2 - \left(\sum_{jet=1}^{2} j \cdot \vec{p}_{jet} + j \cdot j_b \cdot \vec{p}_{bjet}\right)^2}}{\sqrt{\left(\sum_{jet=1}^{2} j \cdot E_{jet}\right)^2 - \left(\sum_{jet=1}^{2} j \cdot \vec{p}_{jet}\right)^2}}$$

$$= \frac{\sqrt{\left(\sum_{jet=1}^{2} E_{jet} + j_b \cdot E_{bjet}\right)^2 - \left(\sum_{jet=1}^{2} \vec{p}_{jet} + j_b \cdot \vec{p}_{bjet}\right)^2}}{\sqrt{\left(\sum_{jet=1}^{2} E_{jet}\right)^2 - \left(\sum_{jet=1}^{2} \vec{p}_{jet}\right)^2}}$$

The bJES dependence of $m_{\text{top, angle}}$ can be explained geometrically: A change of the JES factor j which is applied to all three jets independently neither changes the orientation of the plane defined by the ends of the corresponding momentum vectors in the top-quark restframe nor the angles of the triangle defined by the vectors in this plane (see Figure 7.1). It simply re-scales the overall size of the triangle. Hence, the right-hand side of Equation (7.7) does not change under variations of j. It is, however, not invariant under j_b because this factor is applied to only one of the jets, thus changing both the orientation of the plane, obtained by the Lorentz boost back to the restframe of the top quark, as well as the shape of the triangle within it.

9.2.3. Impact of the Choice of Cleaning Cut CC1 on the Systematic Uncertainties

The studies of the JES and bJES dependence of the mass estimators presented in the two previous sections have been performed on a sample of events that have passed cleaning cut CC1 after reconstruction: Only events for which the invariant mass of the reconstructed W-boson lies within a specified range around the fitted W-boson mass peak $m_{\text{2jet}}^{\text{peak, fit}}$ are considered for further analysis (see Section 8.4.1). The width of this mass window is determined by a multiple of the width $\sigma_{\text{2jet}}^{\text{fit}}$ of the distribution. The standard choice for the cut value is to require $|m_{j1+j2} - m_{\text{2jet}}^{\text{peak, fit}}| < \mathbf{2} \cdot \sigma_{\text{2jet}}^{\text{fit}}$ because, as illustrated in Figure 8.5, this allows to keep the majority of the events for which the W-boson has been reconstructed correctly. The exact choice of the cut value $x \cdot \sigma_{\text{2jet}}^{\text{fit}}$, however, is to some extend arbitrary: Instead of setting $x = 2$, slightly different values could be chosen, for example $x = 1.8$ or $x = 2.2$, or the purity of the sample could be increased further at the cost of a lower efficiency by choosing a significantly smaller mass window, for example $x = 1$.

It turns out that the exact choice of the value of x has a considerable effect on the JES dependence of the mass estimators and hence on the systematic uncertainty of the measurement: Table 9.4 summarises the values of the systematic uncertainties of the three mass estimators for different choices of x. As before, a JES uncertainty of 5% is assumed.

	$x = 1$	$x = 1.5$	$x = 2$
$\boldsymbol{\Delta m_{\text{3jet}}^{\text{JES}}}$	(5.9 ± 0.1) GeV	(7.0 ± 0.1) GeV	(7.7 ± 0.1) GeV
$\boldsymbol{\Delta m_{\text{top, ratio}}^{\text{JES}}}$	(2.3 ± 0.1) GeV	(1.4 ± 0.1) GeV	(0.8 ± 0.1) GeV
$\boldsymbol{\Delta m_{\text{top, angle}}^{\text{JES}}}$	(2.4 ± 0.1) GeV	(1.5 ± 0.1) GeV	(0.8 ± 0.1) GeV

Table 9.4.: Systematic uncertainties $\Delta m_{\text{top, reco}}^{\text{JES}}$ and their errors for the three mass estimators assuming a global uncertainty of 5% on the JES

Again, the uncertainties for the estimators $m_{\text{top, ratio}}$ and $m_{\text{top, angle}}$ are comparable to each other and both are significantly smaller than that for m_{3jet}. However, this difference decreases with decreasing value of x, i.e. with decreasing width of the mass window for the cut: Narrower mass windows correspond to smaller uncertainties for m_{3jet} but larger uncertainties for $m_{\text{top, ratio}}$ and $m_{\text{top, angle}}$.

The effect of a variation of the cut value on the bJES-related uncertainties is negligible (see Table 9.5). This is to be expected because cleaning cut CC1 relies exclusively on the properties of the light-quark jets from the W-boson decay, hence a variation of the energies of the b-quark jets in the event does not have any effect.

	$x = 1$	$x = 1.5$	$x = 2$
$\boldsymbol{\Delta m_{\text{3jet}}^{\text{JES}}}$	(1.6 ± 0.1) GeV	(1.6 ± 0.1) GeV	(1.6 ± 0.1) GeV
$\boldsymbol{\Delta m_{\text{top, ratio}}^{\text{JES}}}$	(1.6 ± 0.1) GeV	(1.5 ± 0.1) GeV	(1.5 ± 0.1) GeV
$\boldsymbol{\Delta m_{\text{top, angle}}^{\text{JES}}}$	(1.6 ± 0.1) GeV	(1.6 ± 0.1) GeV	(1.6 ± 0.1) GeV

Table 9.5.: Systematic uncertainties $\Delta m_{\text{top, reco}}^{\text{bJES}}$ and their errors for the three mass estimators assuming a global uncertainty of 2.5% on the bJES

These observations are an artefact of the analysis: They result from the interplay between the **variation** of the JES factor and the choice of a **fixed** cut value for the cleaning cut CC1. A global variation of the JES causes the signal peak of the two-jet invariant mass distribution m_{2jet} to shift

partly out of the mass window for CC1. This is illustrated schematically in Figure 9.9 for the two values $x = 1$ (solid green lines) and $x = 2$ (solid blue lines), respectively. The average W-boson mass measured in the respective mass windows is shifted in the direction of the peak but to a lesser extent since events are cut at the boundary. For smaller mass windows fewer events contribute and hence the average value of $m_{2\text{jet}}$ (dashed green line) lies closer to the peak position of the unshifted distribution (solid black line) than the corresponding value for a larger window (dashed blue line). Hence, stricter cuts lead to smaller variations of $m_{2\text{jet}}$ and consequently also of $m_{3\text{jet}}$ under a variation of the JES. The effect is just reversed for the two improved estimators $m_{\text{top, ratio}}$ and $m_{\text{top, angle}}$ where smaller W-boson masses in the denominator lead to larger top-quark masses.

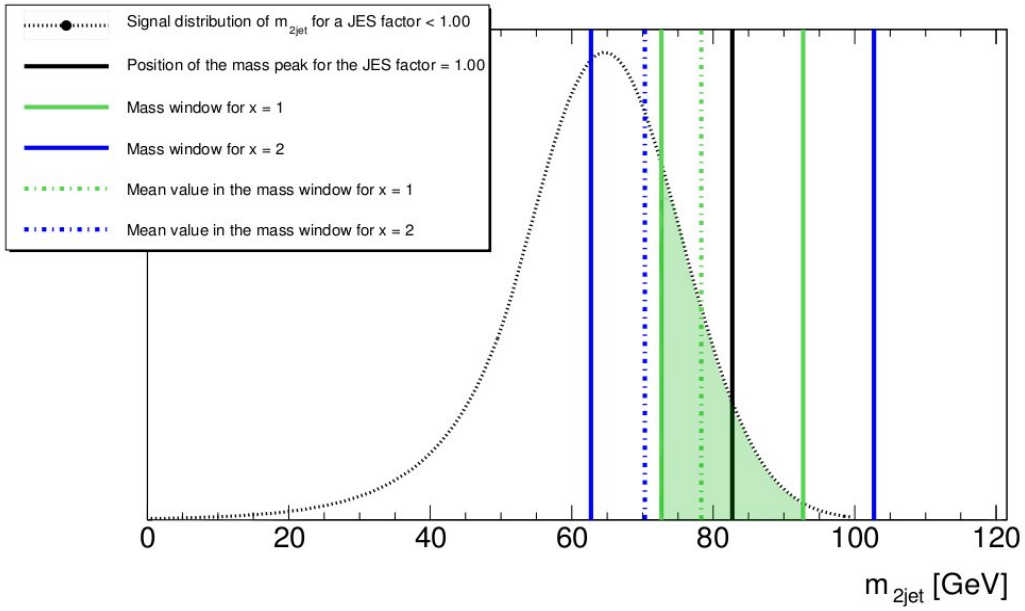

Figure 9.9.: Schematic representation of the effect of different choices for the values of the parameter x on the average reconstructed W-boson mass $m_{2\text{jet}}$: The solid green and blue lines represent the boundaries of the mass windows for $x = 1$ and $x = 2$, respectively. Both mass windows are centered around the fitted peak value of $m_{2\text{jet}}$ for a JES factor of 1.00. The dashed grey curve represents the signal distribution of $m_{2\text{jet}}$ for a JES factor smaller than 1.00. The dashed green line marks the mean value of this distribution within the mass window for $x = 1$ (green shaded area under the curve) and the dashed blue line stands for corresponding mean value of the distribution in the larger mass window for $x = 1$.

The observations described in this section are an important reminder that the choice of cuts applied during the analysis may have a profound influence on the JES-related systematic uncertainties on the top-quark mass. This does not only apply to the simplified model of a global JES uncertainty discussed in Section 9.2.1 but has also to be taken into account in a future refined model in which the systematic uncertainty on the top-quark mass is derived from the local JES uncertainties via error propagation. It is imperative to ensure that the introduction of selection or cleaning cuts does not lead to an overestimation of the systematic uncertainty on the top-quark mass.

9.3. Calibration Curves

As explained in Section 9.1, the fitted peak values for the top-quark mass need to be re-calibrated in order to determine the true top-quark mass. To obtain the calibration curves, various Monte-Carlo samples with different simulated top-quark masses (160 GeV, 170 GeV, 180 GeV and 190 GeV) are used. For each estimator, the reconstructed masses $m_{\text{top, reco}}$ are plotted against the corresponding simulated values of $m_{\text{top, truth}}$ as shown in Figure 9.10 for $m_{3\text{jet}}$. In addition, the JES factor is varied for each value of the simulated mass to show that the JES dependence of the mass estimator is linear for any choice of the input mass.

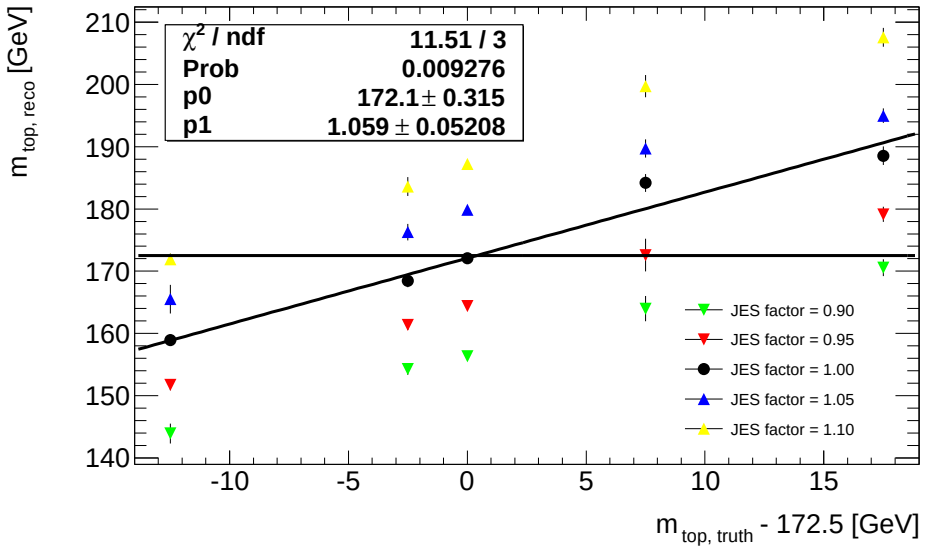

Figure 9.10.: Calibration curve for $m_{3\text{jet}}$ obtained from a linear fit to the reconstructed mass points for different simulated mass points

The functional dependence between $m_{\text{top, reco}}$ and $m_{\text{top, truth}}$ can be parametrised by a linear function

$$m_{\text{top, reco}}[\text{GeV}] = \text{p1} \cdot (m_{\text{top, truth}}[\text{GeV}] - 172.5) + \text{p0}, \tag{9.1}$$

which can be solved for $m_{\text{top, truth}}$.

The parameters p[0] (offset) and p1 (slope) are obtained from a linear fit to the mass points for a JES factor of 1 (black points in Figure 9.10).[9]

The calibration curves for the estimators $m_{\text{top, ratio}}$ and $m_{\text{top, angle}}$ (Figure 9.11) are obtained in a similar fashion.

[9] It should be noted that in order to obtain the final calibration curve, all systematic uncertainties on the reconstructed masses and their correlations need to be taken into account. This can, however, only be done at the final stage of any analysis when all the additional systematic uncertainties, for example those from ISR and FSR, have been studied as well.

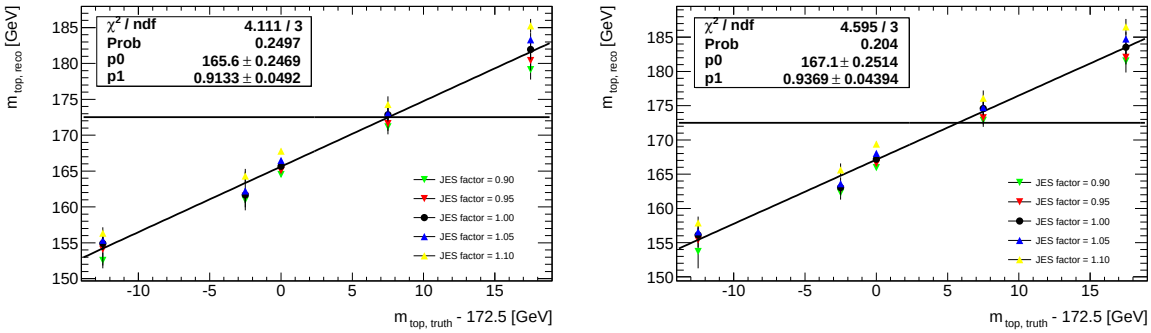

(a) $m_{\text{top, ratio}}$ **(b)** $m_{\text{top, angle}}$

Figure 9.11.: Calibration curves obtained from a linear fit to the reconstructed mass points for different simulated mass points for $m_{\text{top, ratio}}$ (a) and $m_{\text{top, angle}}$ (b)

Equation (9.3) is then solved for $m_{\text{top, truth}}$ to derive the re-calibrated top-quark masses from the fitted peak values stated in Table 9.6. The statistical uncertainties on the re-calibrated values are obtained from simple error propagation. The results are summarised in Table 9.6. The top-quark masses for all three estimators are now in agreement with the generated mass value of 172.5 GeV.

$\boldsymbol{m_{\text{3jet}}}$	(172.2 ± 0.3) GeV
$\boldsymbol{m_{\text{top, ratio}}}$	(172.6 ± 0.3) GeV
$\boldsymbol{m_{\text{top, angle}}}$	(172.4 ± 0.3) GeV

Table 9.6.: Overview of the fitted values of the top-quark mass peak and their statistical errors for the three mass estimators

9.4. Improvement of the Angles Method

As shown in Section 9.2.1, the new estimator for the top-quark mass, $m_{\text{top, angle}}$, introduced in this thesis, yields a significantly reduced JES dependence compared to the commonly used estimator m_{3jet}. However, a small dependence on the jet-energy scale remains even for this improved mass estimator. For a precision measurement of the top-quark mass it would be preferable to further reduce or even eliminate this remaining JES dependence and the corresponding systematic uncertainty.

In this context, it is important to understand the reason for the remaining JES dependence of $m_{\text{top, angle}}$: As has already been noted in Section 7.3, the mathematical expression for this estimator, given in Equation (7.7), does not depend explicitly on the energies and momenta of the three jets from the top-quark decay and therefore not on the jet-energy scale. The angles on the right-hand side of the equation, however, are defined in the restframe of the (hadronically-decaying) top quark and cannot be measured directly in the detector because the top quarks are, in general, boosted with respect to the laboratory frame.

In order to determine the angles between the jets in Equation (7.7), it is necessary to perform a Lorentz transformation from the laboratory frame to the restframe for which the determination of the boost of the top quark from the measured four-vectors of its decay products is required. This leads to an indirect JES dependence of $m_{\text{top, angle}}$.

In the light of these considerations, it would be preferable to select top quarks that are produced with a negligible Lorentz boost, i.e. top quarks that decay while at rest within the detector. In that case, the angles between the jets could be measured directly, rendering the measurement of the four-vectors of the jets unnecessary.

The boost of the top quarks is expressed as the product $\beta\gamma$ where $\gamma = (1-\beta^2)^{-\frac{1}{2}}$ and $\beta = \pm|\vec{v}| = \pm\frac{|\vec{p}|}{E}$ are the common Lorentz factors of Special Relativity and the product $\beta\gamma$ has been chosen because it is proportional to the energy E of the particle. The sign of β and $\beta\gamma$, respectively, is positive if the momentum $\vec{p}$ of the top quark has a positive z-component and negative if it has a negative z-component. Figure 9.12 shows the distribution of the Lorentz boost $\beta\gamma$ of the hadronically-decaying top quarks that have been correctly reconstructed using the ΔR-algorithm.[10]

Here, as well as in all other histograms in this section, all events that pass selection cut C15 (1 b-tag case, see Section 6.2) are considered, and no additional cleaning cuts have been applied to the sample. The reason for choosing this looser set of cuts is to provide sufficient statistics for the procedure described further below.

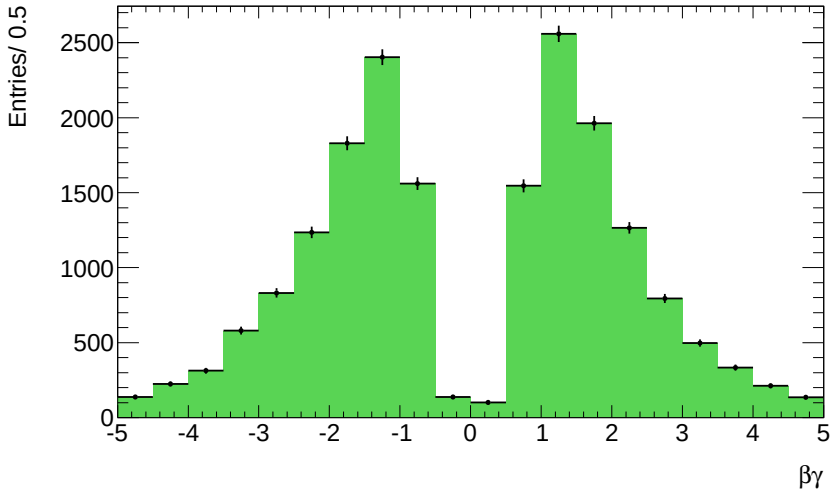

Figure 9.12.: Distribution of the Lorentz boost $\beta\gamma$ of the hadronically-decaying top quarks reconstructed with the ΔR-algorithm after selection cut C15; negative values of $\beta\gamma$ indicate that the component of the top-quark momentum in the direction of the beam axis is negative

The distribution peaks at values of $|\beta\gamma|$ between roughly 1 and 2 and decreases monotonously towards larger values of $|\beta\gamma|$ as is to be expected due to the smaller differential cross section for

[10] The slight asymmetry of the distribution is probably a result of the way the hard-scattering process is modelled in the Monte-Carlo generator: The first initial-state parton is chosen randomly among the partons of the first proton; the second parton is then picked from the proton with opposite momentum along the beam axis and only events in which the two partons have sufficiently large momenta to create a $t\bar{t}$ pair are kept. Since it is more likely to pick a parton with low momentum from the first proton, the events with a top-anti-top pair in the final state are more likely to be those in which the second parton has a considerably higher energy, thus leading to the observed asymmetry in the boost of the top quarks in the final state.

the production of top-anti-top pairs with large momentum. The most important conclusion to be drawn from Figure 9.12, however, is that events containing top quarks with small Lorentz boost ($|\beta\gamma| < 0.5$) are extremely rare. This is a consequence of the application of the selection cuts, in particular those on the minimum transverse jet momentum (C10 - C12 in Section 6.2): These cuts disfavour events with small values of $|\beta\gamma|$ because the decay products of a top quark with small Lorentz boost tend to have smaller momenta than those from highly boosted top quarks and are therefore less likely to pass the selection cuts.

Hence, instead of focussing on the comparatively few top quarks with small values of $|\beta\gamma|$ for the mass measurement, a different approach is chosen: The idea is to evaluate the top-quark mass $m_{\text{top, angle}}$ for different values of the Lorentz boost $\beta\gamma$ and then derive its value at $\beta\gamma = 0$ by interpolation.

Figure 9.13 shows the distribution of the estimator $m_{\text{top, angle}}$ plotted against the Lorentz boost $\beta\gamma$ for correctly reconstructed top quarks.

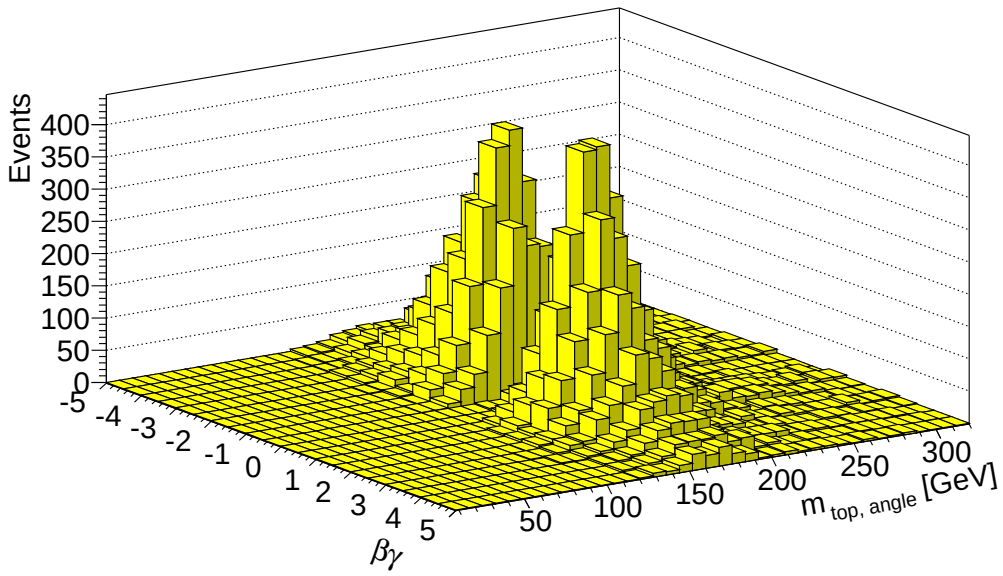

Figure 9.13.: Distribution of $m_{\text{top, angle}}$ plotted against the Lorentz boost $\beta\gamma$ of the hadronically-decaying top quark; events are required to have passed selection cut C15 (1 b-tag) and only correctly reconstructed top quarks are considered

The signal distribution of $m_{\text{top, angle}}$ in each slice in $\beta\gamma$ is fitted with a Crystal Ball function[11] to determine the peak values $m^{\text{peak}}_{\text{top, angle}}(\beta\gamma)$ which are then plotted against $\beta\gamma$ as shown in Figure 9.14. For the interpolation to the mass value at $\beta\gamma = 0$, two linear functions are chosen to fit the mass points for $\beta\gamma < 0$ and $\beta\gamma > 0$, respectively. The requirement that these two functions must intersect at the same mass value p[0] for $\beta\gamma = 0$ imposes an extra constraint on the fit which renders it more stable under statistical fluctuations of the mass points $m^{\text{peak}}_{\text{top, angle}}(\beta\gamma)$ on either side, thus allowing for a more precise determination of p[0] $= m_{\text{top, angle}}(\beta\gamma = 0)$.

[11] Due to the looser set of selection cuts, the shape of the signal distributions in each slice (compare Figure **??**) cannot a priori be assumed to be the same as the one in Figure 9.1. Several functions have been tested on the distributions read out of the individual slices, and the Crystal Ball function has been found to yield again the best fit results.

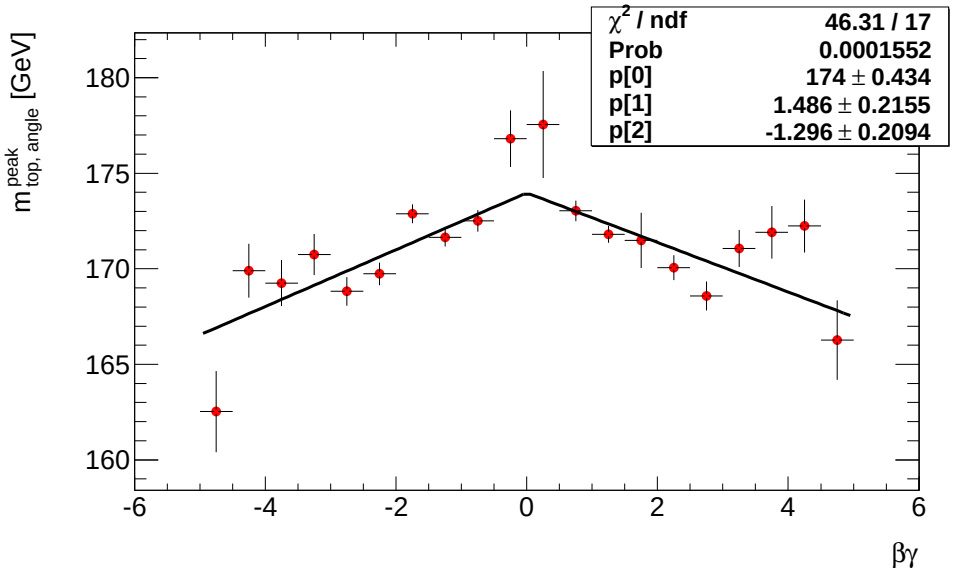

Figure 9.14.: Values of $m^{\text{peak}}_{\text{top, angle}}(\beta\gamma)$, obtained from fitting each slice in $\beta\gamma$ individually, plotted against the Lorentz boost $\beta\gamma$

The fit is not perfect: While the assumption of a linear functional dependence $m^{\text{peak}}_{\text{top, angle}}(\beta\gamma)$ clearly seems justified for the mass points in the range $0.5 < |\beta\gamma| < 3$, the two central points as well as the mass points for values of $|\beta\gamma| > 3$ systematically deviate from the linear curve towards larger mass values. A comparison with Figures 9.12 and 9.13 indicates that this behaviour may be a consequence of the low statistics in the corresponding $\beta\gamma$-slices. For the bins with $0.5 < |\beta\gamma|$, it may be a result of the selection cuts on the minimum transverse momentum of the jets. These cuts disfavour events in the lower tail of the top-quark mass peak, in particular in the case of top quarks with small Lorentz boost. Hence the peak position determined in the fit is systematically shifted towards larger masses, an effect similar to that described in the context of cleaning cut CC1 in Section 9.2.3.

To ensure that the particular shape of the distribution in Figure 9.14 is not simply a result of systematic biases introduced by the fit of the distributions in these slices, the mean values $m^{\text{mean}}_{\text{top, angle}}$ of the mass distributions are additionally evaluated for each slice and plotted against $\beta\gamma$. The result is shown in Figure 9.15. The distribution of the mass points is very similar to that in Figure 9.14. In particular the deviation from the linear fit function towards larger mass values in the bins with lower statistics is clearly visible. This shows that this effect is not just a result of an imperfect fit of the distributions in these slices. A more detailed study of the functional dependence between $\beta\gamma$ and $m^{\text{peak}}_{\text{top, angle}}$ will be possible as soon as larger Monte-Carlo samples become available.

The central mass point p[0] $= m^{\text{peak}}_{\text{top, angle}}(\beta\gamma)$ derived from the interpolation corresponds to top quarks that are (approximately) at rest in the laboratory frame. Based on the considerations at the beginning of this section, p[0] should therefore be taken as an improved estimator for the top-quark mass.

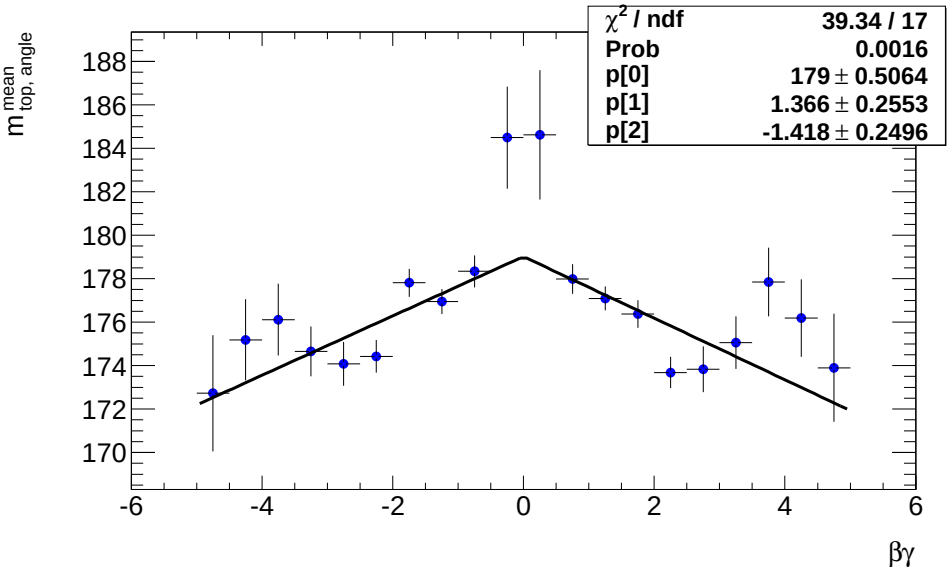

Figure 9.15.: Mean values $m^{\text{mean}}_{\text{top, angle}}(\beta\gamma)$ of each slice in $\beta\gamma$ plotted against the Lorentz boost $\beta\gamma$

Its JES-related systematic uncertainty is studied by varying the energies and momenta of all jets in the event by a global JES factor j as described in detail in Section 9.2.1. The resulting $\beta\gamma$-plots of the mass points $m^{\text{peak}}_{\text{top, angle}}$ including the respective interpolation functions are shown in Figure 9.16 for JES factors of 0.90, 0.95, 1.05 and 1.10.

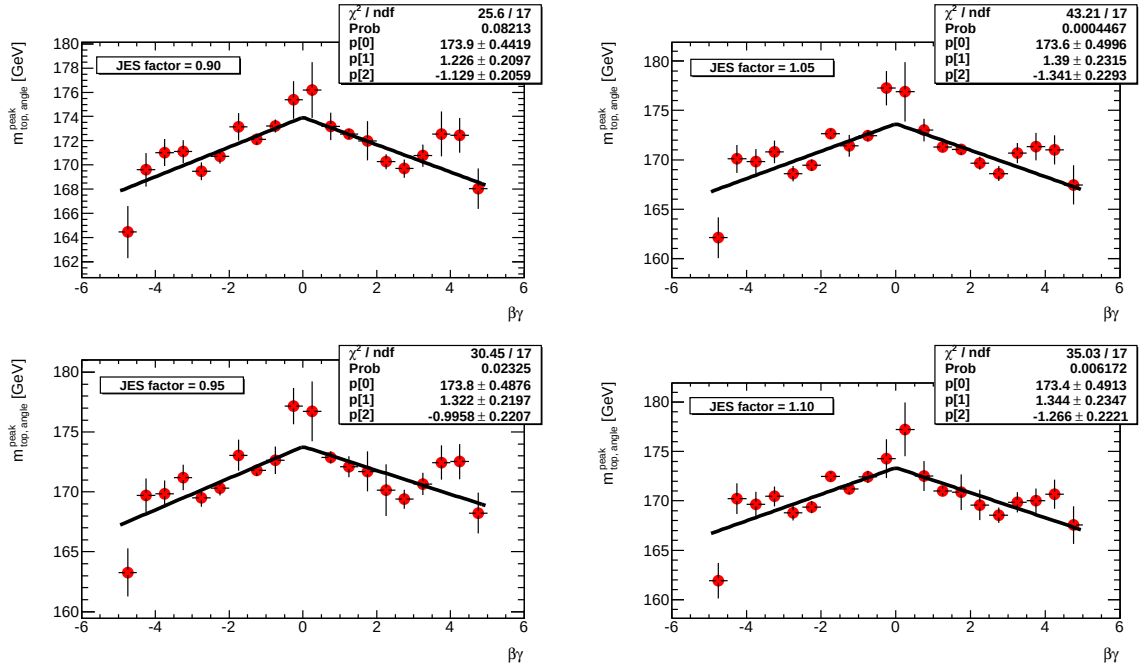

Figure 9.16.: Values of $m^{\text{peak}}_{\text{top, angle}}(\beta\gamma)$ plotted against $\beta\gamma$ for JES factors of 0.90, 0.95, 1.05 and 1.10

These plots clearly illustrate that the central mass point remains constant (within the limits of its statistical uncertainty) under global variations of the JES. The JES-related systematic uncertainty on the estimator p[0] is therefore negligible.

The $\beta\gamma$ interpolation method introduced in this section can, of course, be applied to the other three estimators as well by replacing $m_{\text{top, angle}}$ in Figure 9.13 by $m_{\text{top, ratio}}$ or m_{3jet} and fitting the resulting distributions with Crystal Ball functions to obtain the $\beta\gamma$-$m^{\text{peak}}_{\text{top, reco}}$ plots. These can be found in Appendix G.2.

The JES dependence of the central mass points $m^{\text{peak}}_{\text{top, reco}}(\beta\gamma = 0)$ for each of the three estimators is studied as described above and the results are shown in Figure 9.17.

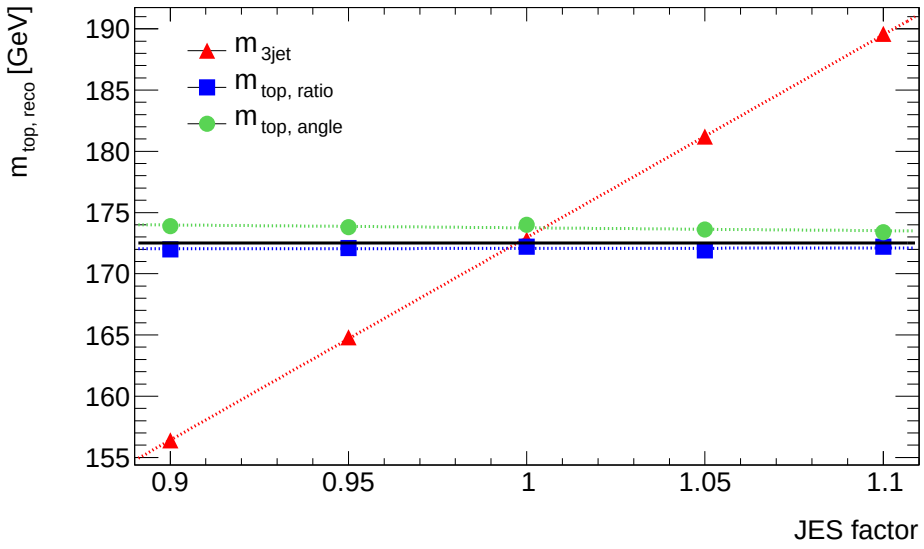

Figure 9.17.: JES dependence of the central mass points $m^{\text{peak}}_{\text{top, reco}}(\beta\gamma = 0)$ for the three estimators $m_{\text{3jet}}, m_{\text{top, ratio}}$ and $m_{\text{top, angle}}$ obtained with the $\beta\gamma$ method. The black horizontal line marks the generator mass $m_{\text{top, truth}} = 172.5$ GeV.

The corresponding systematic uncertainties are stated in Table 9.7: With 8.3 GeV the value of the systematic uncertainty on $m_{\text{3jet}}(\beta\gamma = 0)$ is slightly bigger than the uncertainty obtained with the standard approach in Section 9.2.1 (see Table 9.2). For the improved estimators, however, the slope of the linear fit functions (blue and green lines in Figure 9.17) turns out to be smaller than its uncertainty. Hence, the JES-related systematic uncertainties on $m^{\text{peak}}_{\text{top, ratio}}(\beta\gamma = 0)$ and $m^{\text{peak}}_{\text{top, angle}}(\beta\gamma = 0)$ are negligible.

$\boldsymbol{\Delta m^{\text{JES}}_{\text{3jet}}(\beta\gamma = 0)}$	(8.3 ± 0.1) GeV
$\boldsymbol{\Delta m^{\text{JES}}_{\text{top, ratio}}(\beta\gamma = 0)}$	< 0.2 GeV
$\boldsymbol{\Delta m^{\text{JES}}_{\text{top, angle}}(\beta\gamma = 0)}$	< 0.1 GeV

Table 9.7.: Systematic uncertainties and their errors for the three mass estimators evaluated with the $\beta\gamma$-method assuming a global uncertainty of 5% on the JES

In the light of Section 9.2.3, one might argue that these observations are simply a result of the looser set of cuts applied to the sample studied in this section, in particular of the fact that cleaning cut

CC1 has not been applied here. First studies of the JES dependence of the three mass estimators that have been performed on the same sample that has been used in this section but without applying the $\beta\gamma$-interpolation method, however, yield systematic uncertainties of roughly 0.5 GeV for $m_{\text{top, ratio}}$ and $m_{\text{top, angle}}$. This implies that the independence of the jet-energy scale observed with the $\beta\gamma$-method is indeed a result of the interpolation approach.

Finally, the bJES dependence of $m^{\text{peak}}_{\text{top, reco}}(\beta\gamma = 0)$ is studied by applying a global bJES factor in full analogy to the approach in Section 9.2.2. The results for the central mass points for the three estimators are illustrated in Figure 9.18 and the corresponding systematic uncertainties are summarised in Table 9.8.

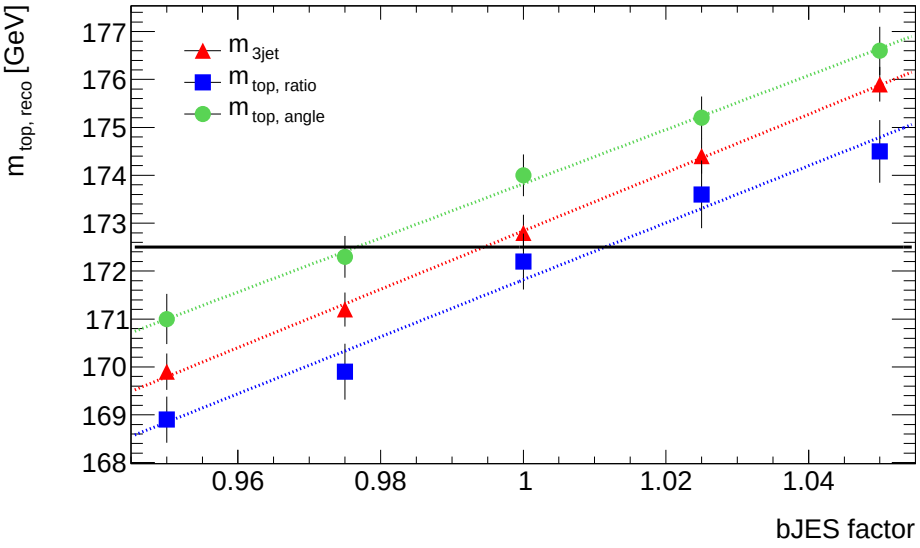

Figure 9.18.: Values of $m^{\text{peak}}_{\text{top, angle}}(\beta\gamma)$ plotted against $\beta\gamma$ for bJES factors of 0.950, 0.975, 1.025 and 1.050

The corresponding uncertainties do not differ significantly from the values derived with the standard approach in Section 9.2.2 (see Table 9.3). The bJES dependence observed for the central mass point, even for the angles method, is probably a result of the fact that a variation of the energies and momenta of the b-quark jets does not only change the absolute value of the reconstructed top-quark momentum - as does a re-scaling applied to all jets in the case of the JES variation - but also its direction. This may lead to an incorrect determination of the central mass point depending on the value of the bJES.

$\boldsymbol{\Delta m^{\text{bJES}}_{\text{3jet}}(\beta\gamma = 0)}$	(1.5 ± 0.1) GeV
$\boldsymbol{\Delta m^{\text{bJES}}_{\text{top, ratio}}(\beta\gamma = 0)}$	(1.5 ± 0.2) GeV
$\boldsymbol{\Delta m^{\text{bJES}}_{\text{top, angle}}(\beta\gamma = 0)}$	(1.4 ± 0.2) GeV

Table 9.8.: Systematic uncertainties and their errors for the three mass estimators evaluated with the $\beta\gamma$-method assuming a global uncertainty of 2.5% on the bJES. The black horizontal line marks the generator mass $m_{\text{top, truth}} = 172.5$ GeV.

Further studies of the interpolation method and its JES and bJES dependence will be possible as soon as larger Monte-Carlo samples become available.

10. Summary and Outlook

In this thesis, a new estimator for the measurement of the top-quark mass in the semileptonic decay channel, $m_{\text{top, angle}}$, has been introduced with the aim of reducing the JES-related systematic uncertainty on the top-quark mass. In this context, it has been shown that the mass of the top quark can be determined solely from the angles between the three jets from its hadronic decay evaluated in the restframe of the top quark. These angles can be measured much more accurately than the energies and momenta of the corresponding jets.

The new mass estimator has been compared to the two already established estimators, the invariant three-jet mass m_{3jet} and the 3-to-2-jet invariant mass ratio m_{ratio}, with particular regard to the JES and bJES dependence. To this end, two reconstruction methods, the ΔR- and the χ^2-method, have been tested in combination with different sets of cleaning cuts for both the 1 b-tag and the 2 b-tags case with the aim of obtaining similar shapes for the combinatorial-background distributions of the three mass estimators. This allows the respective mass distributions to be fitted with the same set of functions, thus providing a coherent basis for the comparison of the JES and bJES dependence of the fitted peak values. It turns out that a combination of the ΔR-method with a cut on the invariant mass of the reconstructed W-boson in the 2 b-tags case meets these requirements best. The resulting distributions are fitted with the sum of two Crystal Ball and a Landau function.

The JES dependence of the three mass estimators is evaluated by scaling the energies and momenta of all jets in an event by a global, i.e. p_T- and η-independent, scale factor that is varied by 10% up and down in steps of 5%. The systematic uncertainties of the different estimators are obtained from the resulting variations of the respective reconstructed masses under the assumption of a global JES uncertainty of 5%.

The bJES dependence is studied similar to the JES dependence by scaling the energies and momenta of all (true) b-jets by a global scale factor. This factor can be regarded as an additional, smaller energy correction for b-quark jets. The systematic uncertainties on the different estimators are evaluated under the assumption of a global bJES uncertainty of 2.5%.

The resulting systematic uncertainties for the three mass estimators are summarised in Table 10.1.

	$\Delta m^{\text{JES}}_{\text{top, reco}}$	$\Delta m^{\text{bJES}}_{\text{top, reco}}$
m_{3jet}	(7.7 ± 0.1) GeV	(1.6 ± 0.1) GeV
$m_{\text{top, ratio}}$	(0.8 ± 0.1) GeV	(1.5 ± 0.1) GeV
$m_{\text{top, angle}}$	(0.8 ± 0.1) GeV	(1.6 ± 0.1) GeV

Table 10.1.: Systematic uncertainties and their errors for the three mass estimators assuming a global uncertainty of 5% on the JES and of 2.5% on the bJES

The new estimator $m_{\text{top, angle}}$ yields a significantly reduced JES dependence compared to the standard estimator m_{3jet}. Its JES dependence is equal to that of the improved estimator $m_{\text{top, ratio}}$. The bJES-related systematic uncertainties are approximately the same for all three estimators.

First studies performed on the signal sample of correctly reconstructed $t\bar{t}$ events indicate that

a further reduction of the JES-related uncertainty of the new mass estimator $m_{\text{top, angle}}$ can be achieved by evaluating it for top quarks with small Lorentz boost $\beta\gamma$ with respect to the laboratory frame. For these events, the angles between the decay products can be measured directly in the laboratory frame without having to perform a Lorentz boost back to the top-quark restframe which requires a measurement of the four-momenta of the decay products and hence introduces a JES dependence into the measurement. To account for the fact that the selection cuts disfavour top quarks with small boosts, the fitted peak values of $m_{\text{top, angle}}$ are plotted against $\beta\gamma$ and two linear fit functions are used to interpolate to the central mass point at $\beta\gamma = 0$.

The JES and bJES dependence of this interpolation point is studied as before by applying global scale factors to the jet energies and momenta. The resulting systematic uncertainties are summarised in Table 10.2.

	$\boldsymbol{\Delta m^{\text{JES}}_{\text{top, reco}}(\beta\gamma = 0)}$	$\boldsymbol{\Delta m^{\text{bJES}}_{\text{top, reco}}(\beta\gamma = 0)}$
$\boldsymbol{m_{\text{3jet}}}$	(8.3 ± 0.1) GeV	(1.5 ± 0.1) GeV
$\boldsymbol{m_{\text{top, ratio}}}$	< 0.2 GeV	(1.5 ± 0.2) GeV
$\boldsymbol{m_{\text{top, angle}}}$	< 0.1 GeV	(1.4 ± 0.2) GeV

Table 10.2.: Systematic uncertainties and their errors for the three mass estimators evaluated with the $\beta\gamma$-method under the assumption of a global uncertainty of 5% on the JES and of 2.5% on the bJES

These first results obtained with the $\beta\gamma$-method are very promising: The JES dependence for both of the improved estimators $m_{\text{top, ratio}}$ and $m_{\text{top, angle}}$ is negligible. The corresponding JES-related systematic uncertainties for a global JES uncertainty of 5% are below 0.2 GeV and 0.1 GeV, respectively. For a further evaluation of this new method, which must eventually also include the combinatorial- and physical-background distributions, larger Monte-Carlo samples than those available at the time of writing are required. This is important in order to study the functional dependence between $m^{\text{peak}}_{\text{top, angle}}$ and $\beta\gamma$, in particular in the $\beta\gamma$-slices with lower statistics. In the light of these considerations, the $\beta\gamma$-method can be regarded as a promising new approach for measuring the top-quark mass at a later stage of the experiment when more data has been taken.

The studies of the JES and bJES dependence of the three mass estimators presented in this thesis have been performed using **global** scale factors to vary the energies and momenta of the respective jets. However, both the JES factors applied during reconstruction to correct the measured energies of the jets and the JES uncertainty depend on the transverse momentum p_T and pseudorapidity η of each jet. This p_T- and η-dependence of the JES factors has already been taken into account during the reconstruction of the simulated jets in the detector simulation for the Monte-Carlo samples used in this analysis. In a refined model, the systematic uncertainties on the top-quark mass would then need to be derived from error propagation after applying p_T- and η-dependent scale factors to vary the jet energies according their **local** JES uncertainties.

With the methods presented in the scope of this thesis, the JES-related systematic uncertainty of the top-quark mass can be significantly reduced and possibly even eliminated. It has also been shown that the bJES-related systematic uncertainty cannot be reduced with any of the estimators currently used. Further studies should therefore focus on the bJES as another dominant source of systematic uncertainty and aim at developing methods of reducing the bJES dependence of the top-quark mass.

Appendices

A. Calculation of Efficiencies and their Uncertainties

The Monte-Carlo samples simulated with the generator MC@NLO contain events with both positive and negative weights of absolute value 1 in order to account for the destructive interference of higher-order Feynman diagrams (see Section 3.1.2). This has to be taken into account when calculating efficiencies and their uncertainties for these samples.

Let N_+ and N_- be the number of events with positive and negative weights before a given cut, respectively, and let n_+ and n_- denote the corresponding numbers after the cut.

The overall efficiency ϵ of the cut can then be calculated as follows:

$$\epsilon = \frac{n_+ - n_-}{N_+ - N_-} \tag{A.1}$$

and its uncertainty, obtained from Gaussian error propagation, is given by

$$\Delta\epsilon = (N_+ - N_-)^{-2}\Big(\left[(1-\epsilon_+)N_+ - (1-\epsilon_-)N_-\right]^2 \cdot (\epsilon_+ N_+ + \epsilon_- N_-) \tag{A.2}$$

$$+(\epsilon_+ N_+ - \epsilon_- N_-)^2 \cdot \left[(1-\epsilon_+)N_+ - (1-\epsilon_-)N_-\right]\Big)^{\frac{1}{2}} \tag{A.3}$$

where $\epsilon_+ = \frac{n_+}{N_+}$ and $\epsilon_- = \frac{n_-}{N_-}$ are the efficiencies for the subsamples of events with positive and negative weights, respectively. For a derivation of these formulas see [57].

For a sample with positive event weights only, these formulas yield the known, simple expressions for a binomial distribution:

$$\epsilon = \epsilon_+ = \frac{n_+}{N_+} \tag{A.4}$$

and

$$\Delta\epsilon = \sqrt{\frac{\epsilon_+(1-\epsilon_+)}{N_+}}. \tag{A.5}$$

B. The Crystal Ball function

The Crystal Ball function that is used for fitting the signal and combinatorial background distributions of the different top-mass estimators is defined as follows:

$$f(x;\bar{x},\sigma,\alpha,n,S) = S \cdot \begin{cases} \exp\left(-\frac{(x-\bar{x})^2}{2\sigma^2}\right), & \text{for } \frac{x-\bar{x}}{\sigma} > -\alpha \\ A \cdot \left(B - \frac{x-\bar{x}}{\sigma}\right)^{-n}, & \text{for } \frac{x-\bar{x}}{\sigma} \leq -\alpha \end{cases} \tag{B.1}$$

where

$$A = \left(\frac{n}{|\alpha|}\right)^n \cdot \exp\left(-\frac{|\alpha|^2}{n}\right) \tag{B.2}$$

$$B = \frac{n}{|\alpha|} - |\alpha| \tag{B.3}$$

It is essentially a Gaussian function with an exponential correction factor below or above a certain value of the paramter α: Positive values of α correspond to an exponential correction on the lower, negative values to a correction on the upper tail of the Gaussian. The parameter n controls the rate of the decay, see Figure B.1. This parameter is kept fixed at a value of $n = 110$ in all fits. Both the function itself and its derivative are continuous.

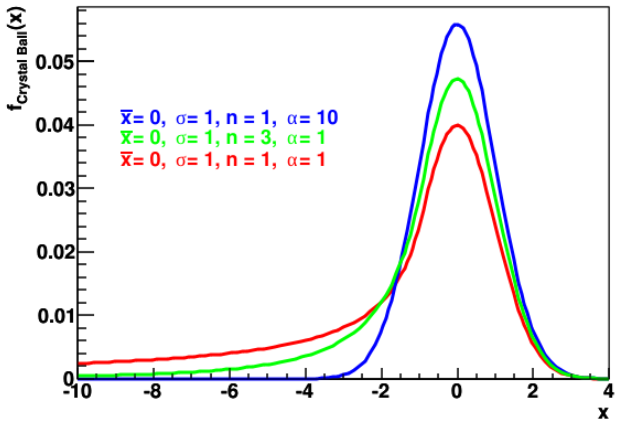

Figure B.1.: Crystal Ball functions for different values of the parameters α and n [63]

The Crystal Ball function was named after the Crystal Ball detector, initially located at the SPEAR[1] accelerator at the Stanford Linear Accelerator Center (SLAC). There it was used in the description of radiative decays of the Ψ' and J/Ψ ([64] and [65]).

[1] This acronym stands for **S**tanford **P**ositron **E**lectron **A**symmetric **R**ings.

C. Object Definitions for ATHENA Release 16.6.5

This appendix contains the details of the object definitions used throughout this analysis. These can also be found on the official Top group Twiki page [44]. A motivation for the various requirements imposed on the reconstructed objects is given in Section 5.

C.1. Electrons

- **Electron category**: tight
- **Reconstruction algorithm**: The reconstruction starts from seeds of calorimeter cells to form calorimeter clusters, i.e. (`author` == 1 || `author` == 3)
- **Transverse energy cut**: $E_T \geq 25$ GeV where E_T is defined as follows:

$$E_T = \frac{E_{EC\_cluster}}{\cosh(\eta_{ID\_track})}$$

- **Pseudorapidity cut**: $0 < |\eta_{EC\_Cluster}| < 2.47$ excluding the crack region $1.37 < |\eta_{EC\_Cluster}| < 1.52$
- **Electron isolation**: pileup-corrected, p_T-corrected Etcone20 < 3.5 GeV using the CaloIsoCorrection tool provided by the Top Working Group
- **Object quality (OQ) requirements**: `el_OQ&1446` == 0 to avoid dead calorimeter cells

C.2. Muons

- **Muon category**: tight
- **Reconstruction algorithm**: MuID combined, i.e. `author` == 12
- **Transverse momentum cut**: offline $p_T > 20$ GeV
- **Pseudorapidity cut**: $|\eta| < 2.5$

- **Additional hit requirements:**
  - (Expect b-layer hit == false) || (Number of b-layer hits > 0)
  - (Number of pixel hits + Number of crossed dead pixel sensors) > 1
  - (Number of SCT hits + Number of crossed dead SCT sensors) ≥ 6
  - (Number of pixel holes + Number of SCT holes) < 3
  - Define n = Number of TRT hits + Number of TRT outliers
    - For $|\eta| < 1.9$: Require n > 5 and (Number of TRT outlier)/n < 0.9
    - For $|\eta| \geq 1.9$: If n > 5, require nTRToutliers/n < 0.9
    - This means that there is no additional cut for muons with $n \leq 5$ and $|\eta| \geq 1.9$
- **Rejection of cosmic muons**: not applied for analyses in the semileptonic $t\bar{t}$ channel
- **Muon Isolation**:
  - Etcone30 < 4 GeV
  - Ptcone30 < 4 GeV
  - **Muon-jet overlap-removal**:
    Remove muons for which there is a jet with $p_T > 20$ GeV within $\Delta R < 0.4$ (before electron-jet overlap-removal).

C.3. Jets

- **Jet type**: Calorimeter jets reconstructed from topological clusters
- **Recombination Scheme**: E scheme
- **Jet algorithm**: anti-k_T algorithm with $R = 0.4$
- **Calibration Scheme**: EM+JES

  ⇒ `AntiKt4TopoEMJets` collection
- Remove jets with negative energy
- **Jet-electron overlap-removal**:
  Remove jets for which there is a selected electron, i.e. an electron that fulfills the electron object definition criteria, within a radius $\Delta R < 0.2$. For the overlap removal, the η and ϕ of the electron track are used.

C.4. Missing Transverse Energy (MET)

- $\not{E}_T$ scheme: `MET_RefFinal_em_tight`

The MET_RefFinal reconstruction and calibration scheme relies on the previous reconstruction of physics objects such as jets, electrons and muons. Energy depositions in calorimeter cells not associated with any of these objects are also taken into account as so-called CellOut terms. Each calorimeter cell is calibrated separately according to a calibration scheme that is specifically adapted to the respective parent object if there is any. The individual contributions are then combined to form the MET object. A schematic overview is given in Figure C.1.

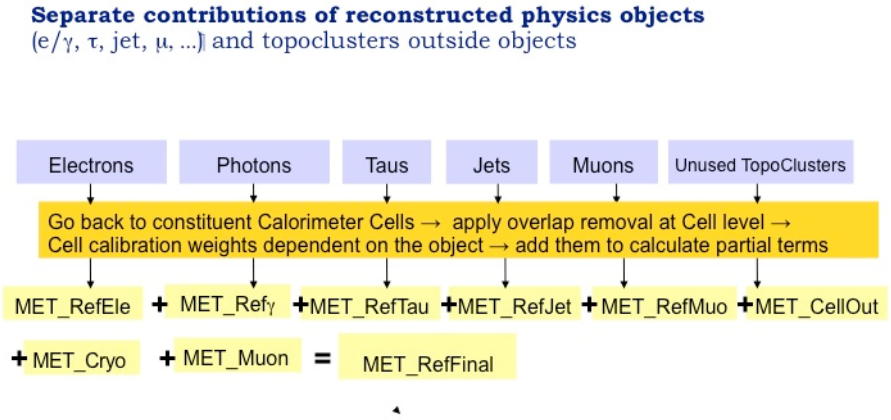

Figure C.1.: Overview of the MET_RefFinal reconstruction and calibration scheme [66]

For details on the reconstruction and calibration process see [53]; an overview of the different MET_RefFinal schemes is given in [66].

C.5. B-tagging

- B-tagging algorithm: SV0
- Tag a jet as b-jet if it has SV0 weight > 5.85 which corresponds to a b-tagging efficiency of 50.1 % and a purity of 93.9 % (see [55])

D. Monte-Carlo Samples

In the following, a complete list of the Monte-Carlo samples used in this analysis is presented. All samples are MC10b samples from the official Top Working Group production based on Release 16.6.5 of the ATHENA [67] framework and using Geant4 [68] for the full detector simulation.

The tables contain information about the respective **hard-scattering process** and **decay channel** as well as the **Monte-Carlo generator(s)** that were used to simulate them. Each sample from the official production has been assigned a unique **D**ata**S**et **ID**entification (**DSID**) code which is also stated in the tables. Moreover, the values for the **product of cross section and branching ratio** for each decay channel are given. This product has to be multiplied with the **k-factor** which parametrises the contributions from higher-order corrections to the cross section.

D.1. $t\bar{t}$ Samples

For these samples, as for all other samples involving top-quarks, MC@NLO was used to simulate the hard-scattering processes at next-to-leading order (NLO). It was interfaced with Herwig and Jimmy for the modelling of the parton/hadron showers for the simulation of the Underlying Event, respectively.

D.1.1. $t\bar{t}$ Baseline Sample

The $t\bar{t}$ baseline sample which is used throughout this analysis, unless stated otherwise, was generated with a top-mass value $m_{top} = 172.5$ GeV.

m_{top} [GeV]	Decay channel	Generator	DSID	$\sigma\cdot$ BR [pb]	k-factor
172.5	non-allhadronic	MC@NLO+Herwig/Jimmy	105200	79.99	1.117

Table D.1.: Non-allhadronic $t\bar{t}$ baseline sample: $m_{top} = 172.5$ GeV

D.1.2. $t\bar{t}$ Mass Variation Samples

In order to test the mass estimators for different input masses and obtain calibration curves, $t\bar{t}$ mass-variation samples with generator masses $m_{top} = 160$ GeV, 170 GeV, 180 GeV and 190 GeV are used.

m_{top} [GeV]	Decay channel	Generator	DSID	$\sigma\cdot$ BR [pb]	k-factor
160	non-allhadronic	MC@NLO+Herwig/Jimmy	106203	117.32	1.12
170	non-allhadronic	MC@NLO+Herwig/Jimmy	106201	85.99	1.12
180	non-allhadronic	MC@NLO+Herwig/Jimmy	106202	64.18	1.12
190	non-allhadronic	MC@NLO+Herwig/Jimmy	106204	48.23	1.12

Table D.2.: Non-allhadronic $t\bar{t}$ mass variation samples for $m_{top} = 160, 170, 180, 190$ GeV

D.2. Single-Top Samples

Like the $t\bar{t}$ samples, all single-top samples were generated with MC@NLO interfaced with Herwig/Jimmy.

D.2.1. Single-Top Baseline Samples

The single-top baseline samples, which are used as background samples to the $t\bar{t}$ baseline sample, were generated with the same top-mass value $m_{top} = 172.5$ GeV.

Production	Decay channel	Generator	DSID	$\sigma\cdot$ BR [pb]	k-factor
t-channel	$e\ \nu$	MC@NLO+Herwig/Jimmy	108340	7.12	1.00
t-channel	$\mu\ \nu$	MC@NLO+Herwig/Jimmy	108341	7.12	1.00
t-channel	$\tau\ \nu$	MC@NLO+Herwig/Jimmy	108342	7.10	1.00
s-channel	$e\ \nu$	MC@NLO+Herwig/Jimmy	108343	0.47	1.00
s-channel	$\mu\ \nu$	MC@NLO+Herwig/Jimmy	108344	0.47	1.00
s-channel	$\tau\ \nu$	MC@NLO+Herwig/Jimmy	108345	0.47	1.00
Wt-channel	inclusive	MC@NLO+Herwig/Jimmy	108346	14.59	1.00

Table D.3.: Single-top background samples for $m_{top} = 172.5$ GeV

D.2.2. Single-Top Mass Variation Samples

For each mass value of the $t\bar{t}$ mass-variation samples, a corresponding set of single-top samples with the same generated top masses was used.

Production	Decay channel	Generator	DSID	$\sigma\cdot$ BR [pb]	k-factor
t-channel	$e\ \nu$	MC@NLO+Herwig/Jimmy	107960	8.27	1.00
t-channel	$\mu\ \nu$	MC@NLO+Herwig/Jimmy	107961	7.94	1.00
t-channel	$\tau\ \nu$	MC@NLO+Herwig/Jimmy	107962	7.95	1.00
s-channel	$e\ \nu$	MC@NLO+Herwig/Jimmy	107963	0.63	1.00
s-channel	$\mu\ \nu$	MC@NLO+Herwig/Jimmy	107964	0.64	1.00
s-channel	$\tau\ \nu$	MC@NLO+Herwig/Jimmy	107965	0.62	1.00
Wt-channel	inclusive	MC@NLO+Herwig/Jimmy	107966	18.43	1.00

Table D.4.: Single-top background samples for $m_{top} = 160.0$ GeV

Production	Decay channel	Generator	DSID	$\sigma\cdot$ BR [pb]	k-factor
t-channel	$e\ \nu$	MC@NLO+Herwig/Jimmy	107970	7.23	1.00
t-channel	$\mu\ \nu$	MC@NLO+Herwig/Jimmy	107971	7.27	1.00
t-channel	$\tau\ \nu$	MC@NLO+Herwig/Jimmy	107972	7.32	1.00
s-channel	$e\ \nu$	MC@NLO+Herwig/Jimmy	107973	0.50	1.00
s-channel	$\mu\ \nu$	MC@NLO+Herwig/Jimmy	107974	0.50	1.00
s-channel	$\tau\ \nu$	MC@NLO+Herwig/Jimmy	107975	0.50	1.00
Wt-channel	inclusive	MC@NLO+Herwig/Jimmy	107976	15.37	1.00

Table D.5.: Single-top background samples for $m_{top} = 170.0$ GeV

Production	Decay channel	Generator	DSID	$\sigma\cdot$ BR [pb]	k-factor
t-channel	$e\ \nu$	MC@NLO+Herwig/Jimmy	107980	6.61	1.00
t-channel	$\mu\ \nu$	MC@NLO+Herwig/Jimmy	107981	6.55	1.00
t-channel	$\tau\ \nu$	MC@NLO+Herwig/Jimmy	107982	6.65	1.00
s-channel	$e\ \nu$	MC@NLO+Herwig/Jimmy	107983	0.40	1.00
s-channel	$\mu\ \nu$	MC@NLO+Herwig/Jimmy	107984	0.40	1.00
s-channel	$\tau\ \nu$	MC@NLO+Herwig/Jimmy	107985	0.40	1.00
Wt-channel	inclusive	MC@NLO+Herwig/Jimmy	107986	12.81	1.00

Table D.6.: Single-top background samples for $m_{top} = 180.0$ GeV

Production	Decay channel	Generator	DSID	$\sigma\cdot$ BR [pb]	k-factor
t-channel	$e\ \nu$	MC@NLO+Herwig/Jimmy	107990	6.01	1.00
t-channel	$\mu\ \nu$	MC@NLO+Herwig/Jimmy	107991	6.03	1.00
t-channel	$\tau\ \nu$	MC@NLO+Herwig/Jimmy	107992	6.06	1.00
s-channel	$e\ \nu$	MC@NLO+Herwig/Jimmy	107993	0.32	1.00
s-channel	$\mu\ \nu$	MC@NLO+Herwig/Jimmy	107994	0.32	1.00
s-channel	$\tau\ \nu$	MC@NLO+Herwig/Jimmy	107995	0.32	1.00
Wt-channel	inclusive	MC@NLO+Herwig/Jimmy	107996	10.79	1.00

Table D.7.: Single-top background samples for $m_{top} = 190.0$ GeV

D.3. W+jets Samples

The W+jets background samples were generated using Alpgen for the simulation of the hard-scattering process interfaced with Herwig/Jimmy to model the parton/hadron shower and the Underlying Event, respectively. The samples fall into four categories, depending on the final states of the hard-scattering process (matrix-element level): W + N partons, W + bb + N partons, W + c + N partons and W + cc + N partons. The different samples overlap in some phase-space regions because heavy quarks may occur both at matrix-element level and as part of the subsequent parton shower. To avoid double-counting of events, the Hfor tool [69], provided by the Top Working Group, is applied to all W+jets samples.

Hard final state	W decay	Generator	DSID	$\sigma\cdot$ BR [pb]	k-factor
W + 0 partons	$e\ \nu$	Alpgen+Herwig/Jimmy	107680	6921.60	1.20
W + 1 parton	$e\ \nu$	Alpgen+Herwig/Jimmy	107681	1304.30	1.20
W + 2 partons	$e\ \nu$	Alpgen+Herwig/Jimmy	107682	378.29	1.20
W + 3 partons	$e\ \nu$	Alpgen+Herwig/Jimmy	107683	101.43	1.20
W + 4 partons	$e\ \nu$	Alpgen+Herwig/Jimmy	107684	25.87	1.20
W + 5 partons	$e\ \nu$	Alpgen+Herwig/Jimmy	107685	7.00	1.20
W + 0 partons	$\mu\ \nu$	Alpgen+Herwig/Jimmy	107690	6919.60	1.20
W + 1 parton	$\mu\ \nu$	Alpgen+Herwig/Jimmy	107691	1304.20	1.20
W + 2 partons	$\mu\ \nu$	Alpgen+Herwig/Jimmy	107692	377.83	1.20
W + 3 partons	$\mu\ \nu$	Alpgen+Herwig/Jimmy	107693	101.88	1.20
W + 4 partons	$\mu\ \nu$	Alpgen+Herwig/Jimmy	107694	25.75	1.20
W + 5 partons	$\mu\ \nu$	Alpgen+Herwig/Jimmy	107695	6.92	1.20
W + 0 partons	$\tau\ \nu$	Alpgen+Herwig/Jimmy	107700	6918.60	1.20
W + 1 parton	$\tau\ \nu$	Alpgen+Herwig/Jimmy	107701	1303.20	1.20
W + 2 partons	$\tau\ \nu$	Alpgen+Herwig/Jimmy	107702	378.18	1.20
W + 3 partons	$\tau\ \nu$	Alpgen+Herwig/Jimmy	107703	101.51	1.20
W + 4 partons	$\tau\ \nu$	Alpgen+Herwig/Jimmy	107704	25.64	1.20
W + 5 partons	$\tau\ \nu$	Alpgen+Herwig/Jimmy	107705	7.04	1.20

Table D.8.: W + jets background samples

Hard final state	W decay	Generator	DSID	$\sigma\cdot$ BR [pb]	k-factor
W + bb + 0 partons	$l\nu$ ($l \in e, \mu, \tau$)	Alpgen+Herwig/Jimmy	107280	47.32	1.20
W + bb + 1 parton	$l\nu$ ($l \in e, \mu, \tau$)	Alpgen+Herwig/Jimmy	107281	35.77	1.20
W + bb + 2 partons	$l\nu$ ($l \in e, \mu, \tau$)	Alpgen+Herwig/Jimmy	107282	17.34	1.20
W + bb + 3 partons	$l\nu$ ($l \in e, \mu, \tau$)	Alpgen+Herwig/Jimmy	107283	6.63	1.20

Table D.9.: W + bb + jets background samples

Hard final state	W decay	Generator	DSID	$\sigma\cdot$ BR [pb]	k-factor
W + c + 0 partons	$l\nu$ ($l \in e, \mu, \tau$)	Alpgen+Herwig	117293	644.4	1.20
W + c + 1 parton	$l\nu$ ($l \in e, \mu, \tau$)	Alpgen+Herwig	117294	205.0	1.20
W + c + 2 partons	$l\nu$ ($l \in e, \mu, \tau$)	Alpgen+Herwig	117295	50.8	1.20
W + c + 3 partons	$l\nu$ ($l \in e, \mu, \tau$)	Alpgen+Herwig	117296	11.4	1.20
W + c + 4 partons	$l\nu$ ($l \in e, \mu, \tau$)	Alpgen+Herwig	117297	2.8	1.20

Table D.10.: W + c + jets background samples

Hard final state	W decay	Generator	DSID	$\sigma\cdot$ BR [pb]	k-factor
W + cc + 0 partons	$l\nu$ ($l \in e, \mu, \tau$)	Alpgen+Herwig/Jimmy	117284	127.53	1.20
W + cc + 1 parton	$l\nu$ ($l \in e, \mu, \tau$)	Alpgen+Herwig/Jimmy	117285	104.68	1.20
W + cc + 2 partons	$l\nu$ ($l \in e, \mu, \tau$)	Alpgen+Herwig/Jimmy	117286	52.08	1.20
W + cc + 3 partons	$l\nu$ ($l \in e, \mu, \tau$)	Alpgen+Herwig/Jimmy	117287	16.96	1.20

Table D.11.: W + cc + jets background samples

D.4. Z+jets Samples

Like the W+jets samples, the Z+jets background samples were generated with Alpgen interfaced with Herwig/Jimmy. They fall into two categories: Z + N partons and Z + bb + N partons. Again, the Hfor tool is used to remove heavy-flavour overlap between the different samples.

Hard final state	Z decay	Generator	DSID	$\sigma\cdot$ BR [pb]	k-factor
Z + 0 partons	$e^+ e^-$	Alpgen+Herwig/Jimmy	107650	668.32	1.25
Z + 1 parton	$e^+ e^-$	Alpgen+Herwig/Jimmy	107651	134.36	1.25
Z + 2 partons	$e^+ e^-$	Alpgen+Herwig/Jimmy	107652	40.54	1.25
Z + 3 partons	$e^+ e^-$	Alpgen+Herwig/Jimmy	107653	11.16	1.25
Z + 4 partons	$e^+ e^-$	Alpgen+Herwig/Jimmy	107654	2.88	1.25
Z + 5 partons	$e^+ e^-$	Alpgen+Herwig/Jimmy	107655	0.83	1.25
Z + 0 partons	$\mu^+ \mu^-$	Alpgen+Herwig/Jimmy	107660	668.68	1.25
Z + 1 parton	$\mu^+ \mu^-$	Alpgen+Herwig/Jimmy	107661	134.14	1.25
Z + 2 partons	$\mu^+ \mu^-$	Alpgen+Herwig/Jimmy	107662	40.33	1.25
Z + 3 partons	$\mu^+ \mu^-$	Alpgen+Herwig/Jimmy	107663	11.19	1.25
Z + 4 partons	$\mu^+ \mu^-$	Alpgen+Herwig/Jimmy	107664	2.75	1.25
Z + 5 partons	$\mu^+ \mu^-$	Alpgen+Herwig/Jimmy	107665	0.77	1.25
Z + 0 partons	$\tau^+ \tau^-$	Alpgen+Herwig/Jimmy	107670	668.40	1.25
Z + 1 parton	$\tau^+ \tau^-$	Alpgen+Herwig/Jimmy	107671	134.81	1.25
Z + 2 partons	$\tau^+ \tau^-$	Alpgen+Herwig/Jimmy	107672	40.36	1.25
Z + 3 partons	$\tau^+ \tau^-$	Alpgen+Herwig/Jimmy	107673	11.25	1.25
Z + 4 partons	$\tau^+ \tau^-$	Alpgen+Herwig/Jimmy	107674	2.79	1.25
Z + 5 partons	$\tau^+ \tau^-$	Alpgen+Herwig/Jimmy	107675	0.77	1.25

Table D.12.: Z + jets background samples

Hard final state	Z decay	Generator	DSID	$\sigma\cdot$ BR [pb]	k-factor
Z + bb + 0 partons	$e^+ e^-$	Alpgen+Herwig/Jimmy	109300	6.57	1.25
Z + bb + 1 parton	$e^+ e^-$	Alpgen+Herwig/Jimmy	109301	2.48	1.25
Z + bb + 2 partons	$e^+ e^-$	Alpgen+Herwig/Jimmy	109302	0.89	1.25
Z + bb + 3 partons	$e^+ e^-$	Alpgen+Herwig/Jimmy	109303	0.39	1.25
Z + bb + 0 partons	$\mu^+ \mu^-$	Alpgen+Herwig/Jimmy	109305	6.56	1.25
Z + bb + 1 parton	$\mu^+ \mu^-$	Alpgen+Herwig/Jimmy	109306	2.47	1.25
Z + bb + 2 partons	$\mu^+ \mu^-$	Alpgen+Herwig/Jimmy	109307	0.89	1.25
Z + bb + 3 partons	$\mu^+ \mu^-$	Alpgen+Herwig/Jimmy	109308	0.39	1.25
Z + bb + 0 partons	$\tau^+ \tau^-$	Alpgen+Herwig/Jimmy	109310	6.57	1.25
Z + bb + 1 parton	$\tau^+ \tau^-$	Alpgen+Herwig/Jimmy	109311	2.49	1.25
Z + bb + 2 partons	$\tau^+ \tau^-$	Alpgen+Herwig/Jimmy	109312	0.89	1.25
Z + bb + 3 partons	$\tau^+ \tau^-$	Alpgen+Herwig/Jimmy	109313	0.39	1.25

Table D.13.: Z + bb + jets background samples

D.5. Diboson Samples

There are three classes of diboson samples, WW, WZ and ZZ, all of which were simulated using Herwig for both the hard-scattering process and the parton/hadron shower. The samples were filtered at generator level so that they contain only events which are likely to pass the rudimentary selection cuts.

Hard final state	Generator	DSID	$\sigma\cdot$ BR [pb]	k-factor	Filter
WW	Herwig	105985	11.5003	1.48	1 lepton ($p_T > 10$ GeV, η <2.8)
ZZ	Herwig	105986	0.9722	1.30	1 lepton ($p_T > 10$ GeV, η <2.8)
WZ	Herwig	105987	3.4641	1.60	1 lepton ($p_T > 10$ GeV, η <2.8)

Table D.14.: Diboson background samples

E. Derivation of the Analytical Expression for the Top-Mass Estimator $\mathbf{m_{top,\,angle}}$

Consider the hadronic top-quark decay $t \to b + W$ where the W-boson decays into two quarks: $W \to q_1 + \bar{q}_2'$.

The following calculations are performed in the restframe of the top quark and all quantities are evaluated in this frame accordingly.

Let p_1 and p_2 be the four-vectors of the two quarks from the decay of the W-boson and let p_b be the four-vector of the corresponding b-quark in the restframe of the top quark:

$$p_k = \begin{pmatrix} E_k \\ \vec{j}_k \end{pmatrix}, \quad k \in \{1, 2, b\}. \tag{E.1}$$

The three quarks from the top-quark decay are assumed to be massless, i.e.

$$m_k^2 = p_k^2 = 0 \quad \text{and} \quad E_k = |\vec{j}_k|, \qquad k \in \{1, 2, b\}. \tag{E.2}$$

The aim of the following calculations is to express the (dimensionless) ratio $\frac{m_W}{m_{\text{top}}}$ of the invariant masses of the W-boson and the top-quark in terms of the angles between $\vec{j}_1$, $\vec{j}_2$ and $\vec{j}_b$ only. To facilitate these calculations, it is convenient to introduce dimensionless four-vectors by dividing all energies and momenta by m_{top}:

$$x_k := \frac{E_k}{m_{\text{top}}} = \frac{|\vec{j}_k|}{m_{\text{top}}} \tag{E.3}$$

$$\vec{j}_k' := \frac{\vec{j}_k}{m_{\text{top}}} \tag{E.4}$$

In the restframe of the hadronically decaying top-quark, momentum conservation dictates that the b-quark and the W-boson are emitted back-to-back and that

$$\vec{j}_1' + \vec{j}_2' + \vec{j}_b' = 0, \tag{E.5}$$

i.e. the three (re-scaled) momentum vectors $\vec{j}_1'$, $\vec{j}_2'$ and $\vec{j}_b'$ lie in the same plane and can therefore w.l.o.g. be represented in two-dimensional coordinates as follows:

$$\vec{j}_1' = \frac{\vec{j}_1}{m_{\text{top}}} = x_1 \begin{pmatrix} 1 \\ 0 \end{pmatrix} \tag{E.6}$$

$$\vec{j}_2' = \frac{\vec{j}_2}{m_{\text{top}}} = x_2 \begin{pmatrix} \cos(\phi_{12}) \\ \sin(\phi_{12}) \end{pmatrix}, \tag{E.7}$$

$$\vec{j}_b' = \frac{\vec{j}_b}{m_{\text{top}}} = x_b \begin{pmatrix} \cos(\phi_{1b}) \\ \sin(\phi_{1b}) \end{pmatrix} = -\vec{j}_1 - \vec{j}_2 = - \begin{pmatrix} x_1 + x_2 \ \cos(\phi_{12}) \\ x_2 \ \sin(\phi_{12}) \end{pmatrix} \tag{E.8}$$

where

$$\cos(\phi_{12}) = \frac{\vec{j}_1 \cdot \vec{j}_2}{|\vec{j}_1|\ |\vec{j}_2|} \tag{E.9}$$

$$\cos(\phi_{1b}) = \frac{\vec{j}_1 \cdot \vec{j}_b}{|\vec{j}_1|\ |\vec{j}_b|} = \frac{x_1\ x_b \cos(\phi_{1b})}{x_1\ x_b} = -\frac{x_1 + x_2\ \cos(\phi_{12})}{1 - x_1 - x_2} \tag{E.10}$$

$$\cos(\phi_{2b}) = \frac{\vec{j}_2 \cdot \vec{j}_b}{|\vec{j}_2|\ |\vec{j}_b|} = \frac{x_2\ x_b \cos(\phi_{2b})}{x_2\ x_b} = -\frac{x_1\ \cos(\phi_{12}) + x_2}{1 - x_1 - x_2}. \tag{E.11}$$

Energy conservation yields the additional constraint

$$x_1 + x_2 + x_3 = 1. \tag{E.12}$$

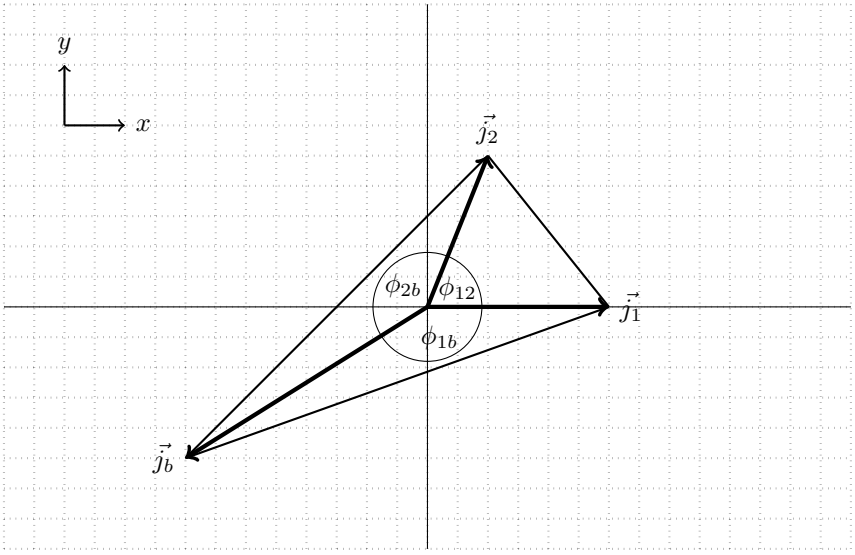

Figure E.1.: Momentum vectors of the two light-quark jets $\vec{j}_1$ and $\vec{j}_2$ and the b-quark jet $\vec{j}_b$ in the two-dimensional coordinate system defined in (E.5)

Equations (E.5) to (E.12) can be solved for the magnitudes of the momenta, x_1, x_2 and x_3, expressed in terms of the angles ϕ_{12}, ϕ_{1b} and ϕ_{2b} only:

$$x_1 = \frac{\sin(\phi_{2b})}{\sin(\phi_{12}) + \sin(\phi_{1b}) + \sin(\phi_{2b})} \tag{E.13}$$

$$x_2 = \frac{\sin(\phi_{1b})}{\sin(\phi_{12}) + \sin(\phi_{1b}) + \sin(\phi_{2b})} \tag{E.14}$$

$$x_3 = \frac{\sin(\phi_{12})}{\sin(\phi_{12}) + \sin(\phi_{1b}) + \sin(\phi_{2b})} \tag{E.15}$$

In the dimensionless units introduced in (E.3) the ratio $\frac{m_W}{m_{\text{top}}}$ can be rewritten as follows:

$$\left(\frac{m_W}{m_{\text{top}}}\right)^2 = \left[\begin{pmatrix} x_1 \\ \vec{j}_1 \end{pmatrix} + \begin{pmatrix} x_2 \\ \vec{j}_2 \end{pmatrix}\right]^2 = \left(\frac{m_1}{m_{\text{top}}}\right)^2 + \left(\frac{m_2}{m_{\text{top}}}\right)^2 + 2\ (x_1 x_2 - \vec{j}_1 \cdot \vec{j}_2) = 2\ x_1 x_2\ [1 - \cos(\phi_{12})] \tag{E.16}$$

where the last step follows from the assumption that the quarks are massless ($\frac{m_k}{m_{\text{top}}} \ll 1$).

Using Equations (E.13) and (E.14), the right-hand side of this equation can be reformulated in terms of angles only to yield the final expression for the top-quark mass $m_{\text{top}} \equiv m_{top,angle}$

$$\left(\frac{m_W}{m_{\text{top, angle}}}\right)^2 = \frac{2 \cdot \sin(\phi_{1b}) \cdot \sin(\phi_{2b}) \cdot [1 - \cos(\phi_{12})]}{[\sin(\phi_{12}) + \sin(\phi_{1b}) + \sin(\phi_{2b})]^2}. \tag{E.17}$$

F. Systematic Variation of the Lower Fit Limit

The following plots show the effect of a variation of the lower fit limit, chosen to be 120 GeV throughout the analysis, by ± 10 GeV. The resulting variations of the fitted peak values for the different mass estimators are listed in Table F.1. The peak values for the fit limits of 110 GeV and 130 GeV are obtained from Figure F.1, those corresponding to a lower limit of 120 GeV are taken from Figures 9.4, 9.5 and 9.6.

	$(m^{110}_{\text{top, reco}} - m^{120}_{\text{top, reco}})$	$(m^{130}_{\text{top, reco}} - m^{120}_{\text{top, reco}})$
m_{3jet}	+0.5 GeV	+0.1 GeV
$m_{\text{top, ratio}}$	±0 GeV	±0 GeV
$m_{\text{top, angle}}$	-0.1 GeV	+0.4 GeV

Table F.1.: Differences between the fitted peak values for a lower fit limit of 120 GeV and the corresponding values for 110 GeV (left column) and 130 GeV (right column)

The resulting systematic uncertainties on the top-quark mass are of the order of the statistical uncertainties.

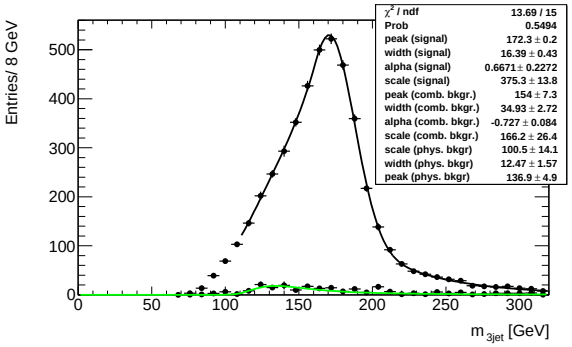

(a) $m_{3\text{jet}}$, $m_{\text{lower limit}} = 110$ GeV

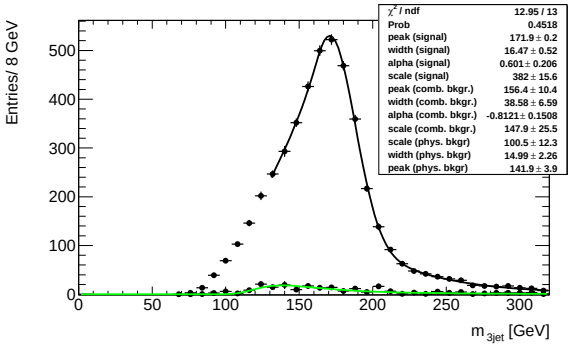

(b) $m_{3\text{jet}}$, $m_{\text{lower limit}} = 130$ GeV

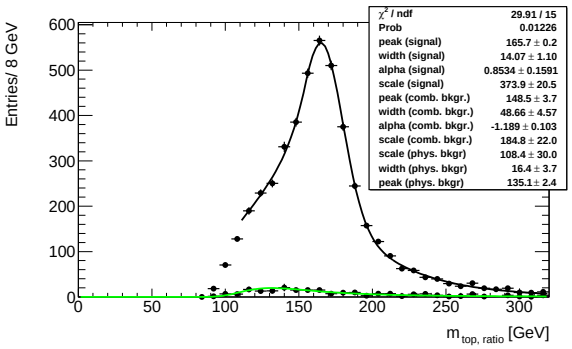

(c) $m_{\text{top, ratio}}$, $m_{\text{lower limit}} = 110$ GeV

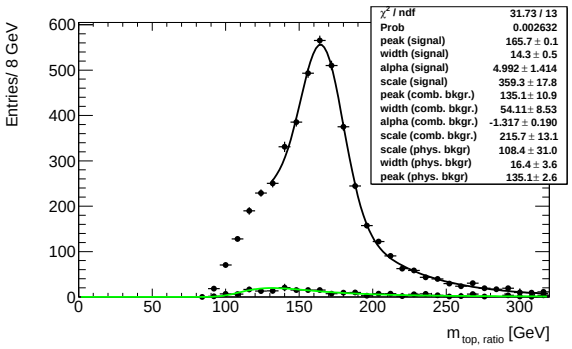

(d) $m_{\text{top, ratio}}$, $m_{\text{lower limit}} = 130$ GeV

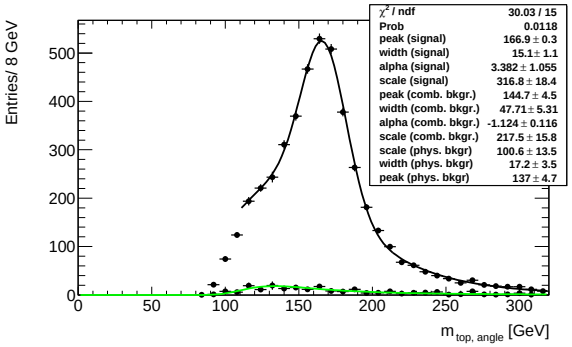

(e) $m_{\text{top, angle}}$, $m_{\text{lower limit}} = 110$ GeV

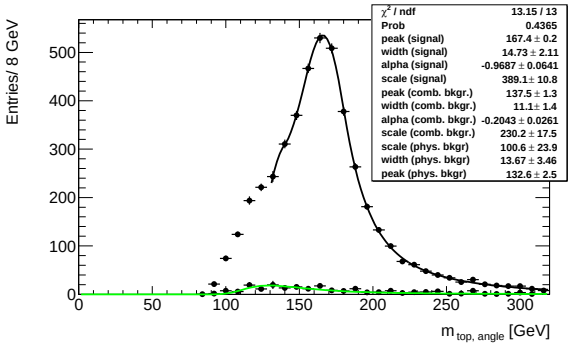

(f) $m_{\text{top, angle}}$, $m_{\text{lower limit}} = 130$ GeV

Figure F.1.: Fit of the complete mass distributions for the three mass estimators with lower fit limits chosen to be 110 GeV (left column) and 130 GeV (right column)

G. Additional Material

G.1. Additional Plots for Section 9.2.3

The plots given in this appendix have been used to derive the values for the JES- and bJES-related systematic uncertainties for different values of the cut parameter x that are stated in Tables 9.4 and 9.5.

G.1.1. JES dependence for $x = 1.5$

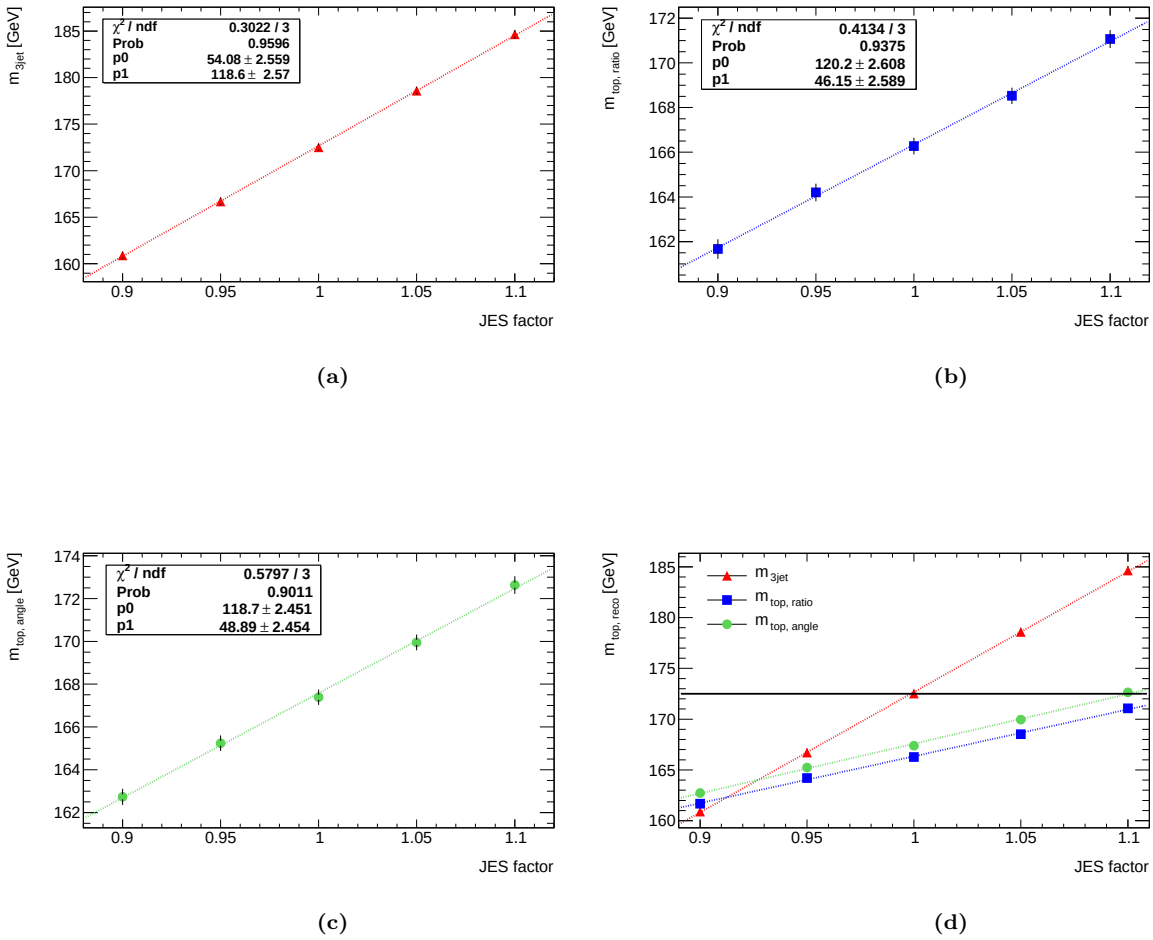

Figure G.1.: JES dependence of the three mass estimators for a value of the cut parameter $x = 1$. The reconstructed masses $m_{\text{top, reco}}$ are plotted against the global JES factor and a linear function is used to fit the mass points (a - c); (d) is a combination of the three subplots. The black horizontal line marks the generator mass $m_{\text{top, truth}} = 172.5$ GeV

G.1.2. JES dependence for $x = 1$

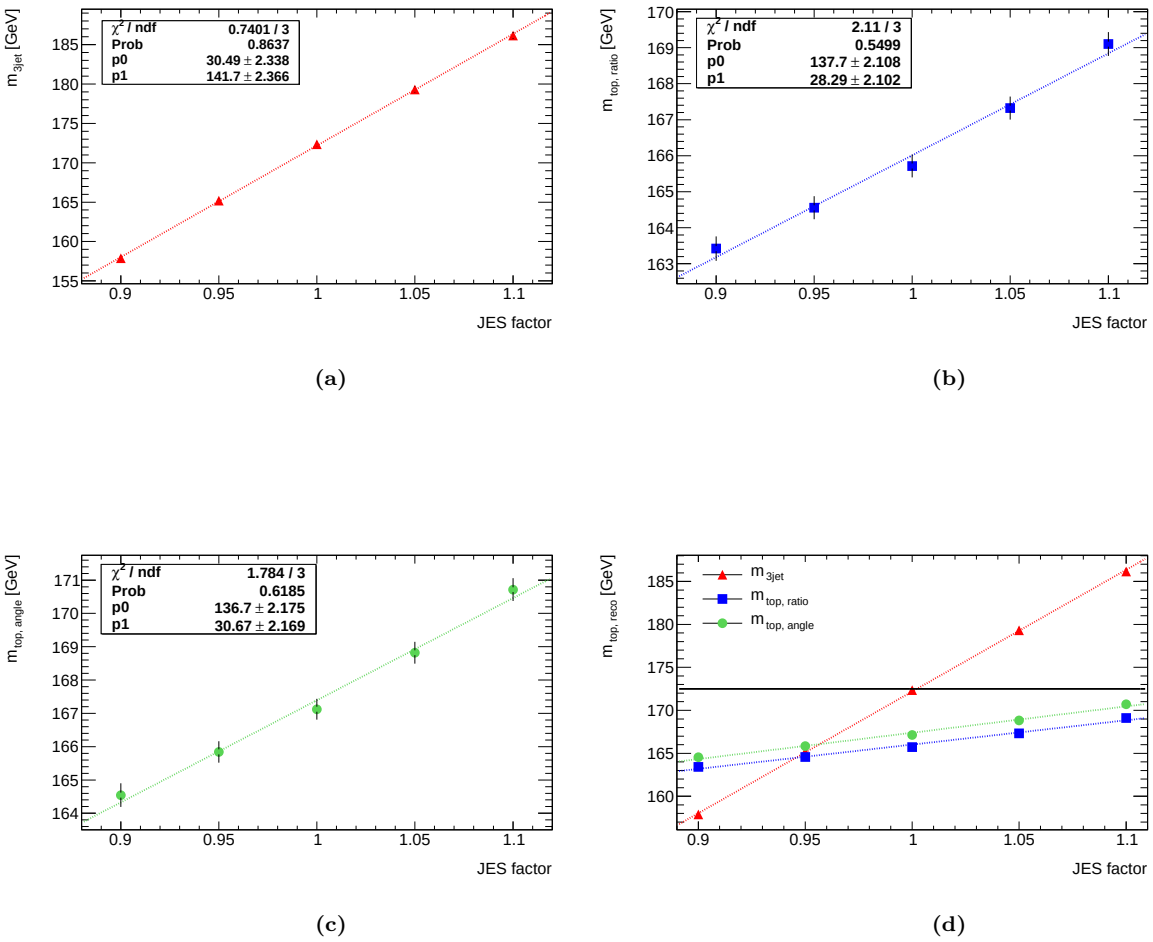

Figure G.2.: JES dependence of the three mass estimators for a value of the cut parameter $x = 1.5$. The reconstructed masses $m_{\text{top, reco}}$ are plotted against the global JES factor and a linear function is used to fit the mass points (a - c); (d) is a combination of the three subplots. The black horizontal line marks the generator mass $m_{\text{top, truth}} = 172.5$ GeV

G.1.3. bJES dependence for $x = 1$

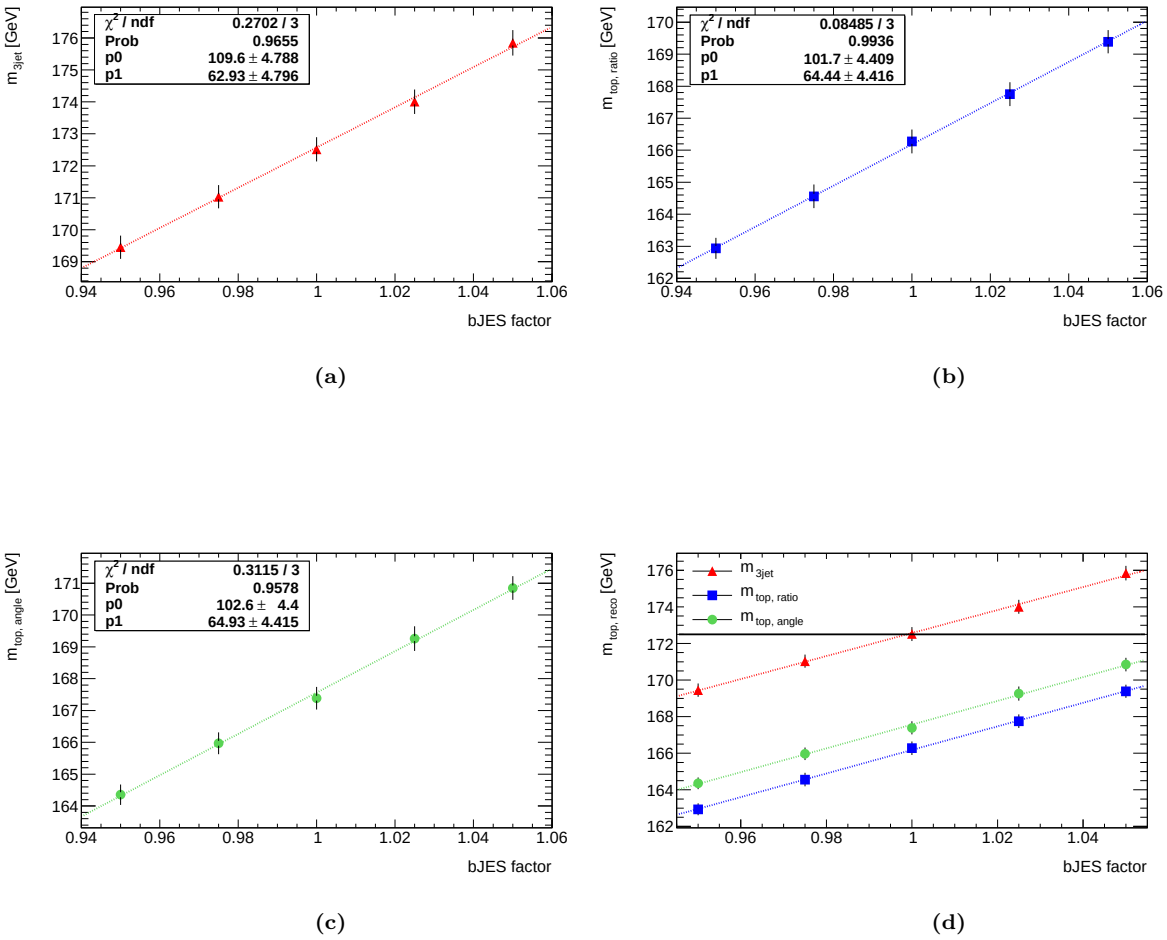

Figure G.3.: bJES dependence of the three mass estimators for a value of the cut parameter $x = 1$. The reconstructed masses $m_{\text{top, reco}}$ are plotted against the global JES factor and a linear function is used to fit the mass points (a - c); (d) is a combination of the three subplots. The black horizontal line marks the generator mass $m_{\text{top, truth}} = 172.5$ GeV

G.1.4. bJES dependence for $x = 1.5$

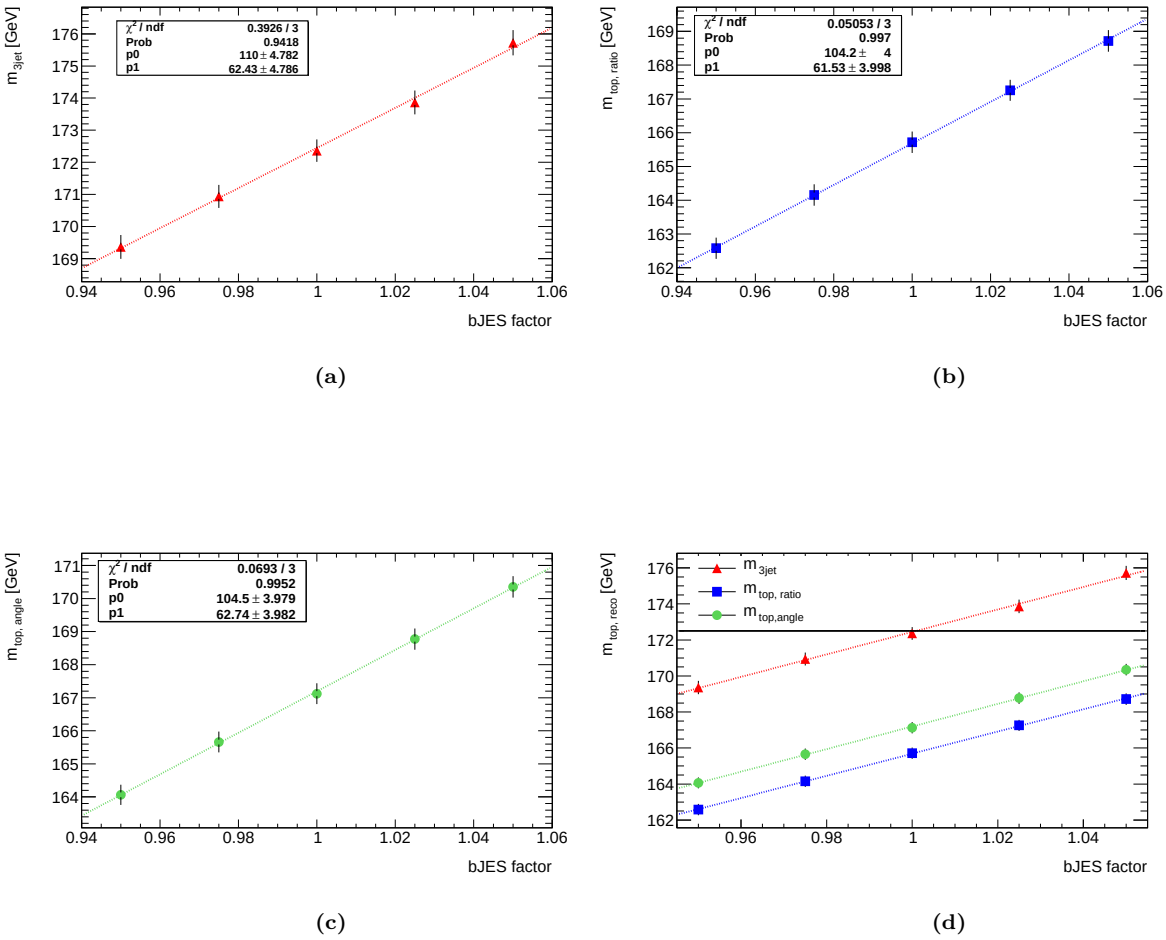

Figure G.4.: bJES dependence of the three mass estimators for a value of the cut parameter $x = 1.5$. The reconstructed masses $m_{\text{top, reco}}$ are plotted against the global JES factor and a linear function is used to fit the mass points (a - c); (d) is a combination of the three subplots. The black horizontal line marks the generator mass $m_{\text{top, truth}} = 172.5$ GeV

G.2. Additional Plots for Section 9.4

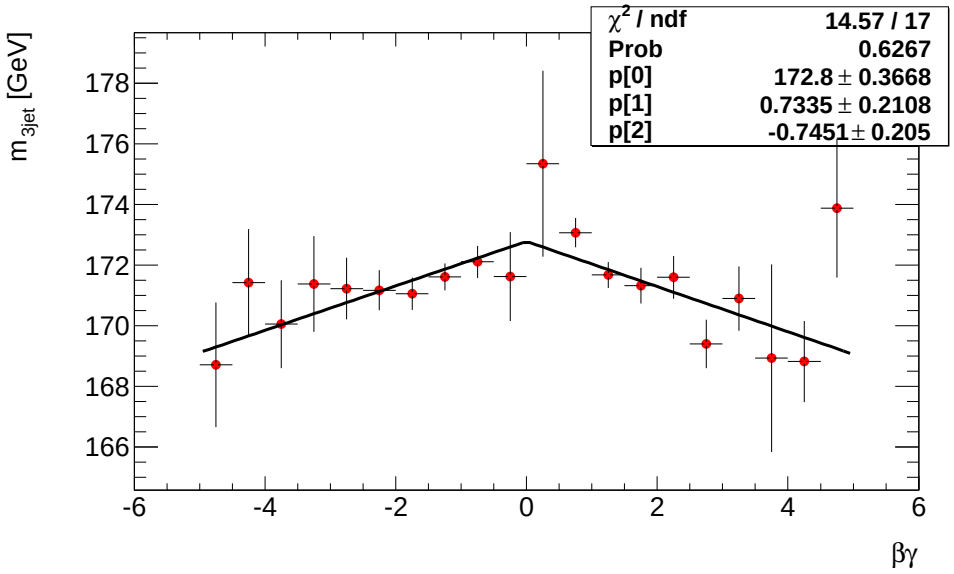

Figure G.5.: Values of $m_{\text{3jet}}^{\text{peak}}(\beta\gamma)$, obtained from fitting each slice in $\beta\gamma$ individually, plotted against the Lorentz boost $\beta\gamma$

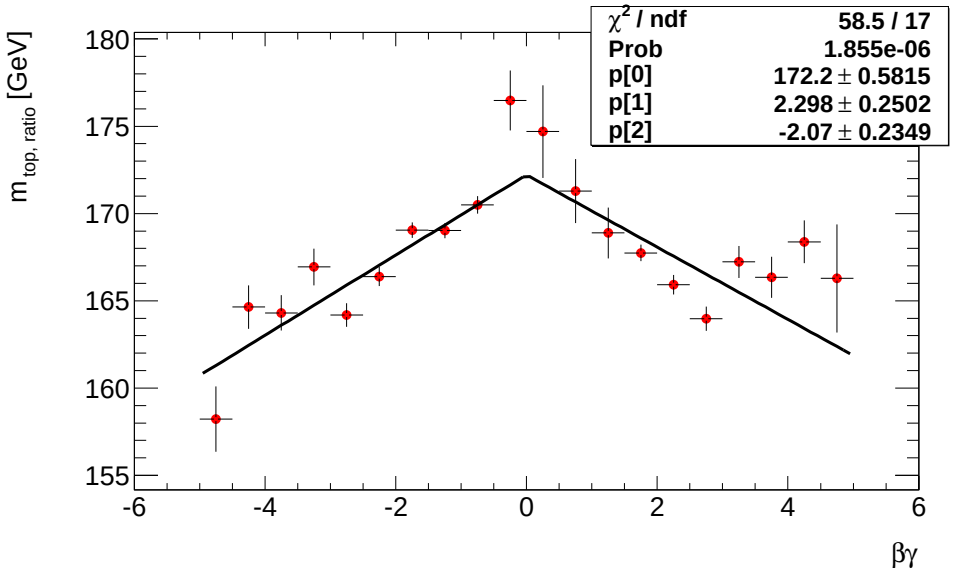

Figure G.6.: Values of $m_{\text{top, ratio}}^{\text{peak}}(\beta\gamma)$, obtained from fitting each slice in $\beta\gamma$ individually, plotted against the Lorentz boost $\beta\gamma$

Bibliography

[1] The TeVatron Electroweak Working Group, the DØ Collaboration, and the CDF Collaboration. Combination of CDF and DØ results on the mass of the top quark using up to 5.8 ifb of data, July 2011. FERMILAB-TM-2504-E.

[2] K. Anthony. Rencontres de Moriond QCD 2012: Straight to the Top. *The CERN Bulletin*, March 2012.

[3] K. Nakamura et al. (Particle Data Group) Review of Particle Physics. *J. Phys. G*, 37(075021), January 2010.

[4] F. Abe et al. (The CDF Collaboration) Observation of Top Quark Production in $\bar{p}p$ Collisions with the Collider Detector at Fermilab. *Phys. Rev. Lett.*, 74:2626, 1995.

[5] S. Abachi et al. (The DØ Collaboration) Observation of the Top Quark. *Phys. Rev. Lett.*, 74: 2632, 1995.

[6] C. M. G. Lattes et al. Processes involving Charged Mesons. *Nature*, 159:694–607, 1947.

[7] R. E. Marshak and H. A. Bethe. On the Two-Meson Hypothesis. *Physical Review*, 72:506, 1947.

[8] S. W. Herb et al. Observation of a Dimuon Resonance at 9.5 GeV in 400-GeV Proton-Nucleus Collisions. *Phys. Rev. Lett.*, 39:252, 1977.

[9] G. Arnison et al. Experimental Observation of Isolated Large Transverse Energy Electrons with Associated Missing Energy at $\sqrt{s} = 540$ GeV. *Physics Letters B*, 122B:103, 1983.

[10] G. Arnison. Experimental Observation of Lepton Pairs of Invariant Mass around 95 GeV at the CERN SPS Collider. *Physics Letters B*, 126B:398, 1983.

[11] R. P. Feynman. *QED: The Strange Theory of Light and Matter*. Princeton University Press, second edition, 1985.

[12] M. E. Peskin and D. V. Schroeder. *An Introduction to Quantum Field Theory*. Westview Press, 1995.

[13] D. Griffiths. *Introduction to Elementary Particles*. WILEY-VCH, second (revised) edition, 2008.

[14] F. Halzen and A. D. Martin. *Quarks and Leptons*. John Wiley and Sons, 1984.

[15] O. Biebel. Experimental Tests of the Strong Interaction and its Energy Dependence in Electron-Positron Annihilation. *Physics Reports*, 340:165, 2001.

[16] O. Biebel. Studien der Quanten-Chromodynamik mit Collider-Experimenten. Lecture held Ludwig-Maximilians-Universität (LMU) München, Wintersemester (Winter Term) 2004/05.

[17] T Sjöstrand, S. Mrenna, and P. Skands. Pythia 6.4: Physics and Manual. *JHEP*, 0605:026, 2006.

[18] G. Corcella, I. G. Knowles, G. Marchesini, S. Moretti, K. Odagiri, P. Richardson, M. H. Seymour, and B. R. Webber. HERWIG 6.5. *JHEP*, 0101:010, 2001.

[19] M. Lambacher. *Study of fully hadronic $t\bar{t}$ decays and their separation from QCD multijet background events in the first year of the ATLAS experiment*. PhD thesis, Ludwig-Maximilians-Universität (LMU) München, July 2007.

[20] M. C. Smith and S. S. Willenbrock. Top Quark Pole Mass. *Phys. Rev. Lett.*, 79(20), December 1996.

[21] The ATLAS Collaboration. Determination of the Top-Quark mass from the $t\bar{t}$ Cross-Section Measurement in pp Collisions at $\sqrt{s} = 7\ TeV$ with the ATLAS detector, March 2011. ATLAS-CONF-2011-054.

[22] The DØ Collaboration. Determination of the pole and $\overline{MS}$ masses of the top quark from the $t\bar{t}$ cross-section. *Physics Letters B*, 703(4):422, September 2011.

[23] The CMS Collaboration. Determination of the Top Quark Mass from the $t\bar{t}$ Cross Section at $\sqrt{s} = 7\ TeV$, December 2011. CMS Physics Analysis Summary.

[24] The LEP Collaborations:. ALEPH, DELPHI, L3, OPAL and the LEP Electroweak Working Group. Combined Preliminary Data on Z Parameters from the LEP Experiments and Constraints on the Standard Model. *CERN-PPE/94-187*, 1994.

[25] A. Grohsjean. *Measurement of the Top Quark Mass in the Dilepton Final State using the Matrix Element Method*. PhD thesis, Ludwig-Maximilians-Universität (LMU) München, December 2008.

[26] The DØ Collaboration. http://www-d0.fnal.gov, February 2012.

[27] N. Kidonakis. Next-to-next-to-leading-order collinear and soft gluon corrections for t-channel single top quark production. *Phys. Rev. D*, 83:091503(R), 2011.

[28] N. Kidonakis. Next-to-next-to-leading-logarithm resummation for s-channel single top quark production. *Phys. Rev. D*, 81:054028, 2010.

[29] N. Kidonakis. Two-loop soft anomalous dimensions for single top quark associated production with a W or H. *Phys. Rev. D*, 82:054018, 2010.

[30] S. Frixione and B. R. Webber. Matching NLO QCD computations and parton shower simulations. *JHEP*, 0206(029), 2002.

[31] S. Frixione, P. Nason, and B. R. Webber. Matching NLO QCD and parton showers in heavy flavour production. *JHEP*, 0308(007), 2003.

[32] N. Kidonakis. Next-to-next-to-leading soft-gluon corrections for the top quark cross section and transverse momentum distribution. *Phys. Rev. D*, 81:114030, 2010.

[33] V. M. Abazov et al. (The DØ Collaboration) Observation of Single Top-Quark Production. *Phys. Rev. Lett.*, 103:092001, 2009.

[34] T. Aaltonen et al. (The CDF Collaboration) Observation of Electroweak Single Top-Quark Production. *Phys. Rev. Lett.*, 103:092002, 2009.

[35] European Organisation for Nuclear Research (CERN). ATLAS - Detector Physics and Physics Performance: Technical Design Report. Technical report, CERN, 1999.

[36] European Organisation for Nuclear Research (CERN). The CERN Document Server. http://cdsweb.cern.ch, January 2012.

[37] L. Evans and P. Bryant (eds.). The LHC Machine. *Journal of Instrumentation (JINST)*, 3 (S08001), 2008.

[38] C. Schmitt. Studien zum Underlying Event bei LHC Energien. Diplomarbeit, Ludwig-Maximilians-Universität (LMU) München, June 2011.

[39] L. Evans and P. Bryant (eds.). The ATLAS Experiment at the CERN Large Hadron Collider. *Journal of Instrumentation (JINST)*, 3(S08003), 2008.

[40] The ATLAS Collaboration. ATLAS Data Summary. https://atlas.web.cern.ch/Atlas/GROUPS/DATAPREPARATION/DataSummary/2011/, January 2012.

[41] Worldwide LHC Computing Grid. http://lcg.web.cern.ch/lcg/, February 2012.

[42] The ATLAS Collaboration. http://www.atlas.ch/, February 2012.

[43] The ATLAS Collaboration. Electron performance measurements with the ATLAS detector using the 2010 LHC proton-proton collision data. *submitted to: Eur. Phys. J. C*, October 2011.

[44] The ATLAS Top Working Group. Twiki Page: TopCommonObjects. https://twiki.cern.ch/twiki/bin/viewauth/AtlasProtected/TopCommonObjects, February 2012.

[45] The ATLAS Collaboration. ATLAS Note: Muon Reconstruction and Identification: Studies with Simulated Monte Carlo Samples, April 2009. ATL-PHYS-PUB-2009-008.

[46] The ATLAS Collaboration. Jet energy measurement with the ATLAS detector in proton-proton collisions at $\sqrt{s} = 7$ TeV. *submitted to: Eur. Phys. J. C*, December 2011.

[47] The ATLAS Collaboration. ATLAS Note: Performance of Jet Algorithms in the ATLAS Detector, April 2010.

[48] T. Sjöstrand. Monte Carlo Generators. Lectures presented at the 2006 European School of High-Energy Physics, Aronsborg, Sweden, 18 June – 1 July 2006, arXiv:hep-ph/0611247v1.

[49] Y. L. Dokshitzer, V. A. Khoze, A. H. Mueller, and S. I. Troyan. *Basics of Perturbative QCD*. Edition Frontières, 1991.

[50] M. Cacciari, G. P. Salam, and G. Soyez. *FastJet 2.4.1 user manual*. arXiv:1111.6097v1.

[51] The ATLAS TopJetLiason Group. Twiki Page: TopJetLiaisonR16Recommendations. https://twiki.cern.ch/twiki/bin/viewauth/AtlasProtected/TopJetLiaisonR16Recommendations, February 2012.

[52] The ATLAS Collaboration. Expected Performance of the ATLAS Experiment: Detector, Trigger and Physics, December 2008. CERN-OPEN-2008-020.

[53] The ATLAS Collaboration. Performance of Missing Transverse Momentum Reconstruction

in Proton-Proton Collisions at $\sqrt{s} = 7$ TeV with ATLAS. *submitted to: Eur. Phys. J. C*, December 2011. CERN-PH-EP-2011-114.

[54] The ATLAS Collaboration. ATLAS Note: Performance of the ATLAS Secondary Vertex b-tagging Algorithm in 7 TeV Collision Data, June 2010. ATLAS-CONF-2010-042.

[55] The ATLAS Flavour Tagging Working Group. Twiki Page: BTaggingBenchmarks. https://twiki.cern.ch/twiki/bin/viewauth/AtlasProtected/BTaggingBenchmarks, February 2012.

[56] The ATLAS Top Cross-Section Working Group. Twiki Page: ATLAS Top Cross-Section. https://espace.cern.ch/topxsec/Lists/Updated%20Ljets%20AtlasPhysics166551/AllItems.aspx, February 2012.

[57] R. Mameghani. *Semi- and Dileptonic Top Pair Decays at the ATLAS Experiment.* PhD thesis, Ludwig-Maximilians-Universität München, May 2008.

[58] K. Herrmann. Early Measurement of the Top Mass at the ATLAS Experiment. Diplomarbeit, Ludwig-Maximilians-Universität München, March 2009.

[59] E. Cogneras and D. Pallin. ATLAS Note: Top Mass measurement in the 2 b-tagged semileptonic $t\bar{t}$ channel, April 2008. ATL-COM-PHYS-2008-044.

[60] E. Cogneras and D. Pallin. ATLAS Note: Reconstruction of $t\bar{t}$ events without b-tagging within ATLAS, March 2009. ATL-COM-PHYS-2009-083.

[61] F. James and M. Roos. Minuit - a system for function minimization and analysis of the parameter errors and correlations. *Computer Physics Communications*, 10(6):343, 1975.

[62] R. Brun and F. Rademakers. ROOT - An Object Oriented Data Analysis Framework, 1997. Proceedings AIHENP'96 Workshop, Lausanne, Sep. 1996, Nucl. Inst. and Meth. in Phys. Res. A 389.

[63] Wikipedia: Crystal Ball function. http://en.wikipedia.org, March 2012.

[64] M. E. Oreglia. *A study of the reactions* $\Psi' \to \gamma\gamma\Psi$. PhD thesis, Stanford Linear Accelerator Center, Stanford University, December 1980.

[65] J. E. Gaiser. *Charmonium spectroscopy from radiative decays of the* J/Ψ *and* Ψ'. PhD thesis, Stanford Linear Accelerator Center, Stanford University, August 1982.

[66] The ATLAS JetEtMiss Working Group. Twiki Page: EtMiss. https://twiki.cern.ch/twiki/bin/viewauth/AtlasProtected/EtMiss, February 2012.

[67] The ATLAS Collaboration. Twiki Page: ATHENA Framework. https://twiki.cern.ch/twiki/bin/viewauth/Atlas/AthenaFramework, February 2012.

[68] S. Agostinelli et al. Geant4: A simulation toolkit. *Nuclear Instruments and Methods in Physics Research A*, 506:250, 2003.

[69] The ATLAS Top Working Group. Twiki Page: Hfor Tool. https://twiki.cern.ch/twiki/bin/viewauth/AtlasProtected.HforTool, February 2012.

Acknowledgements

An dieser Stelle möchte ich mich bei all den Menschen bedanken, die durch ihre Hilfe und ihre Unterstützung maßgeblich zur Vollendung dieser Diplomarbeit beigetragen haben. Mein besonderer Dank gilt dabei

- Prof. Dr. Otmar Biebel für die in jeder Hinsicht hervorragende Betreuung dieser Arbeit, insbesondere für all die Zeit, die er sich für Fragen, Diskussionen und die Lösung softwaretechnischer Probleme genommen hat; ebenso für seinen Rat, seine aufmunternden Worte und die vielen anregenden Gespräche

- Prof. Dr. Jochen Schieck für die Erstellung des Zweitgutachtens und die Gelegenheit, meine Arbeit mit ihm zu diskutieren

- Prof. Dr. Dorothee Schaile für all ihren Rat und ihre Unterstützung

- Frau Herta Franz für ihre freundliche und kompetente Hilfe in administrativen Angelegenheiten

- Stefanie Adomeit für ihre Hilfe bei analysetechnischen Fragen, das Korrekturlesen der Arbeit und die aufmunternden E-Mails während der letzten Wochen

- Christopher Schmitt und Dan Vladoiu für die angenehme Atmosphäre im Büro und ihre stete Hilfsbereitschaft; besonderen Dank auch an Christopher Schmitt für das Korrekturlesen der Arbeit und die Teilhabe an seinen kulinarischen Vorräten

- Jona Bortfeld und Alexander Ruschke für die freundliche Aufnahme in ihrem Büro während meiner ersten beiden Monate am Lehrstuhl

- Johannes Ebke, Dr. Johannes Elmsheuser, Dr. Thomas Müller, Dr. Otto Schaile und Jonas Will für die Hilfe bei programmiertechnischen und das Grid betreffenden Fragen

- Sebastian Becker, Bonnie Chow, Julien de Graat, Christian Meineck, Christopher Schmitt, Dan Vladoiu, Jonas Will und Josephine Wittkowski für die vergnüglichen Tischtennisrunden, ihre Hilfsbereitschaft und die netten Gespräche, sowie allen weiteren Mitgliedern des Lehrstuhls für die angenehme Atmosphäre im Institut

- Alma Brodersen für das gründliche Korrekturlesen der Arbeit

- meinen Eltern Heike und Bernhard Behr und meinem Bruder Beve Behr für all ihre Liebe und ihre Unterstützung in jeder nur erdenklichen Hinsicht

Selbständigkeitserklärung

Hiermit erkläre ich, dass ich die vorliegende Diplomarbeit mit dem Titel

Measurement of the Top-Quark Mass
in the Semileptonic Decay Channel
at the ATLAS Experiment

selbstständig und nur unter Verwendung der angegebenen Quellen und Hilfsmittel angefertigt habe.

München, den 30. März 2012

(Janna Katharina Behr)